Desorption due to recoil induced by neutrino emission and auger relaxation of 37Cl following the electron capture decay of 37Ar
by Lin Zhu

A thesis submitted in partial fulfillment of the requirements for the degree of Doctor of Philosophy in Physics
Montana State University

Abstract:
A novel experiment was developed in this work to study the desorption and the Auger relaxation processes of 37Cl following the 37Ar electron capture decay. For the first time, the desorption of 37Cl ions due to recoil induced by neutrino emission in this decay process was observed. The kinetic energy distribution of the desorbing 37Cl ions was accurately measured by using coincidence techniques. The resulting 37Cl ion energy ranges from 5 eV to 13 eV with a maximum at around 9 eV and an FWHM about 3 eV. The charge state distribution of the desorbing 37Cl ions was also measured. The resulting charge state distribution is: 53% of the total ions have charge +e, 21% have charge +2e and 26% have charge +ne, where $n \geq 3$. The desorbing probability of 37Cl ions was measured by two independent experiments which gave the result of 9.4±1.2%. The energy distribution, the charge state distribution and the desorbing probability of 37Cl ions are all quite different as compared with the expected values for an isolated Cl atom. These differences are explained in the desorption model involving charge exchange and Coulomb repulsion between 37Cl ions and their surrounding atoms.

The electron capture decay also creates a highly unusual initial state in the 37Cl atom which allows direct observation of some novel relaxation processes which are. amenable to many body theory, but essentially impossible to probe experimentally with conventional techniques. For the first time, direct evidence of the double Auget decay of a K-hole and the large shift in energy (22 eV) of an LMM Auger line was reported. The double Auger decay probability and energy distribution of the two double Auger electrons were measured by using coincidence techniques. The resulting double Auger decay probability ranges from 12±0.3% to 15±0.4% of the total Auger decay, The preferred energy distribution of the double Auger emission is for one of the electrons to take most of the energy, with the second receiving the small remaining balance. A model explaining the large shift in energy of an LMM Auger line is also provided.

DESORPTION DUE TO RECOIL INDUCED BY NEUTRINO EMISSION AND AUGER RELAXATION OF ^{37}Cl FOLLOWING THE ELECTRON CAPTURE DECAY OF ^{37}Ar

by

LIN ZHU

A thesis submitted in partial fulfillment
of the requirements for the degree

of

Doctor of Philosophy

in

Physics

MONTANA STATE UNIVERSITY—BOZEMAN
Bozeman, Montana

May 1995

APPROVAL

of a thesis submitted by

LIN ZHU

This thesis has been read by each member of the thesis committee and has been found to be satisfactory regarding content, English usage, format, citations, bibliographic style, and consistency, and is ready for submission to the College of Graduate Studies.

Dr. Gerald Lapeyre G J Lapeyre 6-9-95
(Signature) (Date)

Approved for the Department of Physics

Dr. John Hermanson 6-9-95
(Signature) (Date)

Approved for the College of Graduate Studies

Dr. Robert Brown R L Brown 6/23/95
(Signature) (Date)

STATEMENT OF PERMISSION TO USE

In presenting this thesis in partial fulfillment of the requirements for a doctoral degree at Montana State University—Bozeman, I agree that the Library shall make it available to borrowers under the rules of the Library. I further agree that copying of this thesis is allowable only for scholarly purposes, consistent with "fair use" as prescribed in the U.S. Copyright Law. Requests for extensive copying or reproduction of this thesis should be referred to University Microfilms International, 300 North Zeeb Road, Ann Arbor, Michigan 48106, to whom I have granted "the exclusive right to reproduce and distribute my dissertation in and from microform along with the non-exclusive right to reproduce and distribute my abstract in any format in whole or part."

Signature

Date 6-9-95

DEDICATED TO MY GRANDMOTHER
AND MY PARENTS

VITA

Lin Zhu was born on October 29, 1962 in Beijing, China to Shijun Zhu and Wenjuan Xiang. He has a younger sister, Hong Zhu.

Lin Zhu was raised in the beautiful campus of Tsinghua University, Beijing China where he attended the university-attached primary school in 1969, junior high school in 1974 and high school in 1977. In 1980, he was admitted to Tsinghua University, one of the best schools in China. He completed his undergraduate education with a B.S. degree in electrical engineering in 1985. In the same year, he started his graduate study in the Graduate College of Tsinghua University. From 1987 to 1989, he studied in the Physics Department of the Technical University of Munich, Munich, West Germany. In 1989, he came to the wonderful small town called Bozeman. He got his M.S. degree in physics from Montana State University in 1992.

PREFACE

Eight years ago, when Dr. Avci, a surface scientist met Dr. Hindi, a nuclear physicist half a world away in Saudi Arabia, they came up with a brilliant idea: using surface analysis techniques to study nuclear reactions. Six years ago, Dr. Menzel invited me to his office, "I just talked to Prof. Lapeyre in Montana. You should not disappoint them when you get there," he told me in German, "because I have just put up a lot of good words for you." Four years ago, there began this research project. With the help of a German professor, I got the opportunity to work under the guidance of professors with Turkish, Lebanese and American origin. I would like to dedicate this report to these mentors who have shown me how small this world could be for physicists.

My sincere thanks to those who made this possible. To Dr. Lapeyre for his help in my coming to this great country, for his continuous support, supervision and confidence in me. To Dr. Avci for his scientific inspiration, encouragement and patient guidance throughout this thesis work. To Dr. Hindi who has helped me throughout this project with his sharp instincts in physics and tireless working spirits. To Dr. Anderson for his important criticisms and advice that have been and will remain as a beneficial experience for me. To Dr. Smith, Dr. Tuthill and Department Chairman, Dr. Hermanson for their great support in my graduate study. To the wonderful staff, Alice, Margaret and Rose for their cheerful help. To Erik and Norm for their excellent technical support.

TABLE OF CONTENTS

Page

VITA..v

PREFACE..vi

TABLE OF CONTENTS...vii

LIST OF TABLES...x

LIST OF FIGURES...xi

ABSTRACT...xv

1. INTRODUCTION..1

Concepts of the Work..2

Desorption due to Recoil Induced by Neutrino Emission..................2

Surface Interactions of ^{37}Cl Ion..5

Auger Relaxation of ^{37}Cl Atom...8

Historical Review of Related Works..10

2. THEORY..14

Recoil Induced by Neutrino Emission...14

Models on Stimulated Desorption...17

The Menzel-Gomer-Redhead (MGR) Model...................................18

TABLE OF CONTENTS—Continued

Page

    The Knotek-Feibelman (KF) Model 22
    Desorption Due to "Coulomb Explosion" 25
  Theory of Auger Transition 29
    Auger Effect 29
    Auger Energies and Intensities 33
    Double Auger Transition 38
3. EXPERIMENT 45
  Experimental Setups 45
    The UHV System 46
    The Substrates 49
    The Detectors 51
    The Position Sensitive Detector 56
    The Radioactive ^{37}Ar Sources 61
  Coincidence Techniques and Electronic Systems 66
  Experimental Procedure 73
4. RESULTS AND DISCUSSIONS 77
  Desorption due to Recoil Induced by Neutrino Emission 77
    Energy Distribution of ^{37}Cl Ions 77
    Charge-State Distribution of ^{37}Cl Ions 83

TABLE OF CONTENTS—Continued

Page

Results on Multiple and Mixed Layers....91

Desorption Probability of ^{37}Cl Ions.... 95

Discussion of the Desorption Results.... 99

Auger Relaxation of a ^{37}Cl atom....108

^{37}Cl LLM and LMM Auger Peaks.... 109

Discussion of ^{37}Cl LMM Auger Results....113

Double Auger Decay of a ^{37}Cl atom.... 117

^{37}Cl Double Auger Probability.... 118

^{37}Cl Double Auger Energy Distribution....127

Discussion of ^{37}Cl Double Auger Decay Results.... 133

5. CONCLUSIONS....140

Conclusions....140

Perspective on Neutrino Mass Limit Study.... 143

REFERENCES.... 146

APPENDICES.... 156

Appendix A: Introduction to Neutrino Physics and Neutrino Mass Limit Study....156

Appendix B: Designing Diagrams of the Detectors.... 168

Appendix C: Plasmon Decay into Multi-Electron-Hole Pairs in Si(111)... 176

LIST OF TABLES

Table Page

2.1 Table of the Energies, Symbols and Number of Electrons for Ar and Cl Core Levels....29

2.2 Table of Final States of Ar KLL Auger Series....32

2.3 Table of Ar LMM Auger Energies and Relative Intensities....36

2.4(a) Table of Auger Transition Probabilities for a K-hole Vacancy....36

2.4(b) Table of Auger Transition Probabilities for L-hole Vacancies....37

2.5 Table of Final Charge State Distribution of Ar after Auger Transition of an 1s Initial Hole....38

4.1 Table of Charge State Distribution Results from Experiments and Simulations....84

A1.1 Table of the Three Generations of Quarks and Leptons....161

A1.2 Table of Neutrino Mass Fitting Results....165

LIST OF FIGURES

Figure Page

1.1 Electron capture decay and ^{37}Cl ions desorption in $^{37}Ar \rightarrow ^{37}Cl + \nu$ 3

1.2 The original 9.5 eV recoil energy and the additional energy due to charge exchange and Coulomb repulsion of the ^{37}Cl ions 6

1.3 The unusual initial state of ^{37}Cl atom from EC decay 9

1.4 Normal Auger transition and double Auger transition 10

2.1 The energy level scheme of MGR model 19

2.2 The energy level scheme of Antoniewicz model 21

2.3 The KF model for O^+ ion desorption 23

2.4 Schematic displaying terms of a Hubbard Hamiltonian with intrasite Coulomb term U_{eff} 27

2.5 KLL Auger transition and LLM Coster-Koing Auger transition 30

2.6 Energy changes of an Auger electron entering analyzer with work function 34

2.7 Relative intensities of Auger peaks of Ar with 1s hole calculated by using RACS 37

2.8 Brueckner-Goldstone diagrams for the partial amplitudes of double Auger decay 40

2.9 Diagrams for double Auger decay models 42

2.10 Double Auger energy distribution calculated for atomic Ne 43

3.1 UHV system schematics 47

LIST OF FIGURES—Continued

Figure Page

3.2 Auger peaks of Ar and Carbon from the substrates at different temperatures 48

3.3 TPD spectrum of Ar from the graphite substrate 50

3.4 The mounting bridge between the graphite substrate and the cold finger 51

3.5 Diagram of the home-made channeltron based detector 53

3.6 Diagram of the home-made microchannel plates based detector 55

3.7 MCP pulse high distribution and detecting efficiencies for electron and ion 55

3.8 Geometry of a circular arc terminated resistive anode encoder 59

3.9 Diagram of the home-made MCP-RAE based PSD detector 60

3.10 The gamma ray spectrum of the radioactive gas source taken by an HP-Ge detector 62

3.11 The gamma ray spectrum of the ^{37}Ar gas source 63

3.12 Double sealing ^{40}Ca in quartz ampoules before nuclear irradiation 65

3.13 Schematic diagram of the first coincidence measurement system 67

3.14 True coincidence counts and accidental coincidence counts 68

3.15 Schematic diagram of the second coincidence measurement system 70

3.16 The logic block diagram of the second coincidence measurement system 71

4.1 The Monte-Carlo simulation of the ^{37}Cl ion recoil velocity distribution 79

LIST OF FIGURES—Continued

Figure Page

4.2 Time-of-flight spectrum obtained by using coincidence measurement and the corresponding energy spectrum of the desorbing ^{37}Cl ion................ 81

4.3 Comparison of ToF spectra between the Monte-Carlo simulations and the experimental results.. 82

4.4 Using retarding field energy analyzer to measure charge state distribution.. 85

4.5 Retarding field energy spectrum of the desorbing ^{37}Cl ion............................86

4.6 Calculating charge state distribution from the RFE spectrum....................... 87

4.7 Comparison of charge state distribution and the REF spectra between the Monte-Carlo simulation and the experimental results...............89

4.8 Comparison of the maximum kinetic energy obtained by ToF and RFE spectra... 90

4.9 RFE spectra of desorbing ^{37}Cl ion at different coverage.............................. 92

4.10 Comparison of RFE spectra, total ion counts and maximum kinetic energies among different mixtures of radioactive and stable Ar....... 93

4.11 Comparison of energy distribution of desorbing ^{37}Cl ion from different coverage...95

4.12 KLL and LMM Auger electron-electron coincidence ToF spectrum........... 98

4.13 Local environment of ^{37}Cl ion... 100

4.14 The simulation results of Cl^{+} ion exchange charge with metal surface......... 104

4.15 The model explaining charge exchange and Coulomb repulsion during ^{37}Cl ion desorption...106

4.16 The RAE spectrum of ^{37}Cl LMM Auger... 110

LIST OF FIGURES—Continued

Figure Page

4.17 Comparison of LMM Auger spectra among ^{37}Cl following EC decay, Cl from CsCl and physisorbed ^{40}Ar.......... 111

4.18 ^{37}Cl LMM Auger spectrum measured with new radioactive source.......... 113

4.19 Comparison between ^{37}Cl LMM Auger spectrum and Cl conventional Auger lines.......... 114

4.20 The Auger cascade model explaining the LMM^H peak.......... 116

4.21 Spectrum of coincidence measurement between KLL Auger and LMM Auger.......... 119

4.22 Spectrum of coincidence measurement between two Double Auger electrons.......... 120

4.23 The RFE spectrum of ^{37}Cl LMM Auger by the MCP detector.......... 123

4.24 Spectra of coincidence measurement for KLL and LMM Auger electrons with different retarding screen voltages.......... 126

4.25 Spectra of coincidence measurement for double Auger electrons with different retarding screen voltages.......... 128

4.26 Double Auger energy distribution.......... 130

4.27 Differential energy dependence of the double Auger probability as compared with theoretical prediction.......... 131

4.28 Double Auger energy distribution measured with the new source.......... 132

4.29 Schematic diagram of a triple coincidence spectrum.......... 134

4.30 Comparison of double Auger coincidence spectra between experimental and simulation results.......... 138

ABSTRACT

A novel experiment was developed in this work to study the desorption and the Auger relaxation processes of ^{37}Cl following the ^{37}Ar electron capture decay. For the first time, the desorption of ^{37}Cl ions due to recoil induced by neutrino emission in this decay process was observed. The kinetic energy distribution of the desorbing ^{37}Cl ions was accurately measured by using coincidence techniques. The resulting ^{37}Cl ion energy ranges from 5 eV to 13 eV with a maximum at around 9 eV and an FWHM about 3 eV. The charge state distribution of the desorbing ^{37}Cl ions was also measured. The resulting charge state distribution is: 53% of the total ions have charge +e, 21% have charge +2e and 26% have charge +ne, where $n \geq 3$. The desorbing probability of ^{37}Cl ions was measured by two independent experiments which gave the result of 9.4±1.2%. The energy distribution, the charge state distribution and the desorbing probability of ^{37}Cl ions are all quite different as compared with the expected values for an isolated Cl atom. These differences are explained in the desorption model involving charge exchange and Coulomb repulsion between ^{37}Cl ions and their surrounding atoms.

The electron capture decay also creates a highly unusual initial state in the ^{37}Cl atom which allows direct observation of some novel relaxation processes which are amenable to many body theory, but essentially impossible to probe experimentally with conventional techniques. For the first time, *direct* evidence of the double Auger decay of a K-hole and the large shift in energy (22 eV) of an LMM Auger line was reported. The double Auger decay probability and energy distribution of the two double Auger electrons were measured by using coincidence techniques. The resulting double Auger decay probability ranges from 12±0.3% to 15±0.4% of the total Auger decay. The preferred energy distribution of the double Auger emission is for one of the electrons to take most of the energy, with the second receiving the small remaining balance. A model explaining the large shift in energy of an LMM Auger line is also provided.

CHAPTER 1

INTRODUCTION

On February 23, 1987, a supernova burst in the Large Magellanic Cloud (SN1987a) and sent rays of neutrinos to the earth. The sudden release of the 10^{53} erg of energy from the dying star triggered merely 100 or so "neutrino" counts in huge underground detectors around the world. This, however, caused enough excitement for several groups of physicists—the burst of SN1987a gave them a golden opportunity to study the mysteries of neutrinos.[1,2] Among these mysteries, the biggest one is whether neutrino has a rest mass or not, and what that mass might be. The neutrino mass problem is one of the most fundamental questions in physics. The answer to this question could have profound implications for particle physics, astrophysics and cosmology.[3]

The mass information of a neutrino can be obtained from a nuclear reaction involving the creation or annihilation of a neutrino.[1-3] One of these kinds of nuclear reactions is the electron capture (EC) decay. In this thesis, the desorption due to recoil induced by neutrino emission and the Auger relaxation processes of ^{37}Cl following the EC decay of ^{37}Ar is reported. It is demonstrated in this work that the EC decay of ^{37}Ar provides not only a possible approach to the neutrino mass problem but also a rare opportunity for some novel studies in surface and atomic physics.[4-7] The focal point of this thesis is to report the results of these novel studies.

The problems addressed in this thesis work fall into two categories: The first one is the study of the desorption due to recoil induced by neutrino emission in the EC decay process, $^{37}Ar \rightarrow {}^{37}Cl + \nu$, where ν is a neutrino. In this EC decay process, could the emission of the neutrino cause enough recoil of the adsorbed daughter atom ^{37}Cl to break the absorption bond? If the desorption does occur, what factors would affect the energy distribution of those desorbing daughter atoms? The second category is the study of the Auger relaxation processes of the ^{37}Cl daughter atom. The EC decay creates a deep vacancy in the energy levels of the ^{37}Cl atom while the whole atom is still in a neutral charge state. As discussed later, this initial state is highly unusual as compared with those commonly encountered initial excitations. What are the relaxation processes or the decay channels associated with this particular initial state? To better understand these questions, the concepts of these studies will be introduced first in the following paragraphs.

Concepts of the Work

Desorption due to Recoil Induced by Neutrino Emission

The first part of the study is to measure the spectrum of recoil velocities of ^{37}Cl ions following the EC decay of ^{37}Ar physisorbed on a well defined surface. In this EC decay process which converts ^{37}Ar into ^{37}Cl, a proton in the nuclei of ^{37}Ar captures a 1s or 2s electron and becomes a neutron, while a neutrino is emitted and the ^{37}Cl daughter atom recoils in the direction opposite to that in which the neutrino moves. This recoil may break the bond between the ^{37}Cl atom and the substrate and cause desorption of the ^{37}Cl ions from the surface (Fig. 1.1). The initial 1s or 2s vacancy created by the EC process will decay through Auger cascades or x-ray emission. Therefore the daughter ^{37}Cl atom is usually multiple ionized after the EC decay.

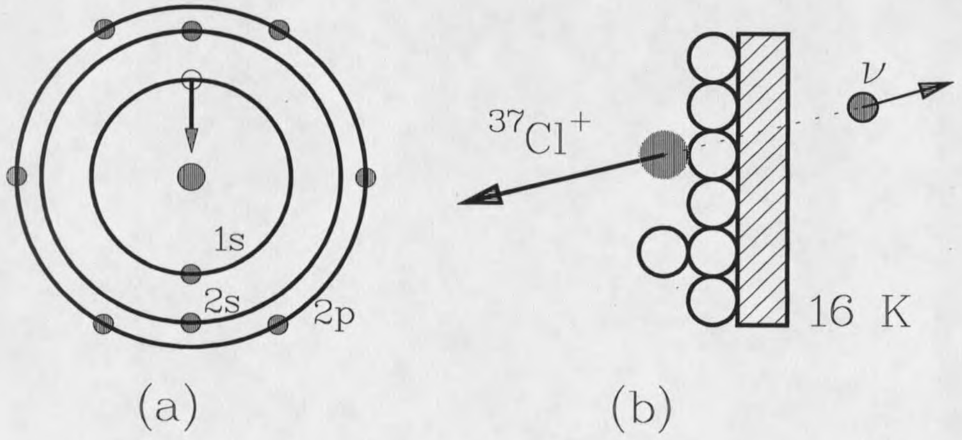

Figure 1.1. (a) Electron is captured from a low (1s) orbital: $^{37}\mathrm{Ar} \rightarrow {}^{37}\mathrm{Cl} + \nu$. (b) ^{37}Cl ion recoils and desorbs from surface due to neutrino emission.

For an isolated ^{37}Ar atom, the recoil process is a two-body problem with a total reaction energy, Q = 814 keV (Ref. 8). Energy and momentum conservation dictates that the recoil energy must be 9.54 eV, if a massless neutrino with about 814 keV of energy is emitted. If a neutrino with mass m_v is also emitted in a certain fraction of the EC decays, then the corresponding recoiling ions will have lower kinetic energy. The fractional change in recoil kinetic energy is $\Delta E/E = (m_v/Q)^2$ (Ref. 3), where Q, the total reaction energy is the rest mass (mc^2) difference between ^{37}Ar and ^{37}Cl. Thus the heaviest massive neutrino that could be emitted in this EC decay would have a rest mass of 814 keV. If a 250-keV neutrino were to be emitted, for example, the fractional change in recoil energy of the ^{37}Cl would be 9.4%. The lowest neutrino mass to which this method could be sensitive depends on the ability to resolve the peak associated with the emission of the massive neutrino from the dominant peak associated with the emission of the massless neutrino in the recoil spectrum.

There are well known and calculable effects that would contribute to the broadening in the recoil energy spectrum for an isolated ^{37}Ar atom. Some of these effects can be studied by computer simulations. However, for an ^{37}Ar atom physisorbed on a cold surface, and possibly surrounded by other Ar atoms, it is not obvious whether the recoil due to neutrino emission could break the bond between ^{37}Cl atom and the substrate and cause desorption. Even if the desorption does occur, it is still much more difficult, as compared to the isolated ^{37}Ar case, to determine what effects would contribute to the broadening in the recoil energy spectrum. To approach these questions, it is necessary to examine the surface interactions during the ^{37}Cl ion desorption process.

Surface Interactions of ^{37}Cl Ion

Adsorption and stimulated desorption have been very useful tools to study surfaces. Since the 1960s, several models have been developed to describe the interactions between adsorbates and the substrates. Current models involve detailed knowledge of surface binding energies, adsorption site symmetries and potentials, substrate phonon spectra, and surface electronic structures.[9-12] The neutrino recoil in this work provides an entirely new way to study the desorption dynamics. A simple model of the desorption in this case is described as follows: First, the adsorbed ^{37}Ar atoms undergo EC decay and become ^{37}Cl ions with 9.54 eV recoil energy to move away from the surface. Before these ^{37}Cl ions can leave the surface, the interactions between the ^{37}Cl ions and the substrate will result in additional kinetic energies on the top of the 9.54 eV recoil energy. These additional energies will contribute to the broadening of the recoil energy spectrum. One of the major goals in this work is to understand these interactions.

The first interaction to be discussed is the bonding between ^{37}Ar and the cold substrates. The ^{37}Ar atom is physisorbed on gold or graphite substrates. At the critical temperature of 65 K Ar begins to form a monolayer on these substrates. By about 30 K, multiple adsorbed layers (Ar ice) are formed.[13-15] It has been found that these multiple adsorbed layers are likely to form a face-centered cubic (fcc) polycrystalline layer at the experimental temperature of 16 K.[16] Therefore the adsorbed Ar could actually form a band structure and solid state physics has to be taken into account. The bonding between an ^{37}Ar atom and the substrate or the neighboring Ar atoms is established through the van der Waals interaction which gives rise to a binding energy of about 100 meV.[15] This interaction cannot play a major role in the broadening of the recoil energy spectrum because the 100 meV interaction energy is much less than the 9.54 eV recoil energy.

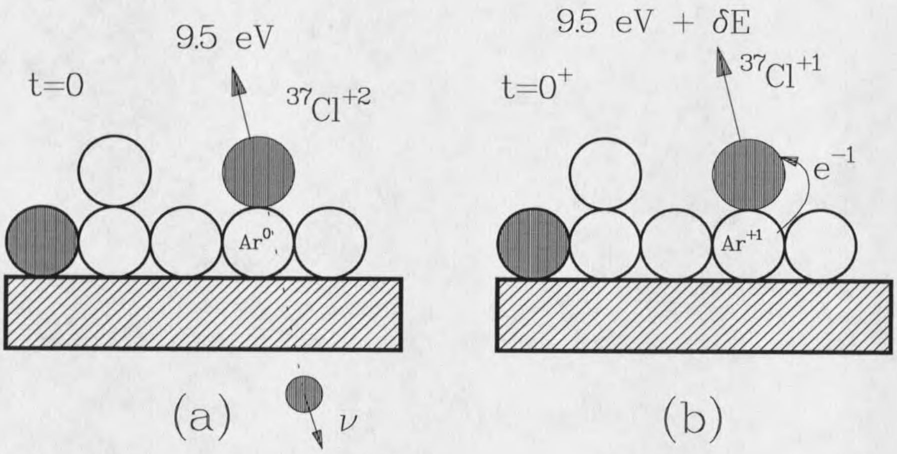

Figure 1.2 (a) ^{37}Cl ion obtains 9.5 eV recoil energy from neutrino emission. (b) Charge is transferred and Coulomb repulsion gives additional energy *δE* to the outgoing ^{37}Cl ion.

The second interaction to be discussed is the charge exchange between the ^{37}Cl ions and their local surrounding atoms.[17-21] Theoretical calculations and experiments have shown that in the gas phase the EC decay of ^{37}Ar will give rise to dominantly ^{37}Cl^{3+}, the positively threefold-charged ions.[22, 23] It is energetically more favorable for the ^{37}Cl^{3+} ion to pick up an electron from the neighboring particle, such as an Ar atom, during the initial phase of desorption.[24] These charge exchanges, however, could significantly broaden the recoil energy spectrum. The positively charged ^{37}Cl ions and their positively charged neighboring atoms will interact via the Coulomb repulsion giving additional contributions to the kinetic energy of the outgoing ^{37}Cl ions (Fig. 1.2). In some cases, the additional energy due to this "Coulomb explosion"[25] could reach as high as 6 eV. The charge exchange process and Coulomb repulsion are the main causes of the broadening of the ^{37}Cl recoil energy spectrum.

The charge exchange process can also cause an outgoing ^{37}Cl ion to lose all of its positive charges and become a neutral atom while desorbing from the surface.[26-28] The experimental setup in this work can only detect charged particles. An estimation of the neutralization cross section and ion desorption yield per electron capture decay will be given from the experimental and computer simulation results.

There are other interactions that affect the energy distribution of the ^{37}Cl ions desorbing from the substrate. Two examples of them are the thermal vibration of the ^{37}Ar atoms on the substrate and the recoil of the ^{37}Cl ions due to Auger electron emission. The physical and chemical characteristics of the substrates can also play an important role in affecting the energy distribution of the ^{37}Cl ions. Some of these effects will be calculated using computer simulation to compare with the experimental results.

A full treatment of each of the interactions discussed above is beyond the scope of this work, rather, the emphasis is put on the study of the "Coulomb explosion" phenomenon which is of great significance for the understanding of this particular desorption process. Because this interaction is the dominant factor in the broadening of the recoil energy spectrum, it also becomes a major obstacle to the neutrino mass limit measurements. The broadening of the recoil spectrum reduces the sensitivity of the neutrino mass limit measurements in this experiment. However, through the present studies the major factors which are responsible for the broadening of the recoil spectrum are understood. Future experiments will be designed with reduced charge exchange effects.

Auger Relaxation of ^{37}Cl atom

The electron capture decay of the ^{37}Ar atom creates a highly unusual electronic configuration in the daughter ^{37}Cl atom which is not encountered in ordinary non-nuclear physical process. Conventional excitations utilizing electron or photon bombardments generally leave the atom in an ionized initial state. However, in the EC decay a proton and an electron become a neutron, hence the total net charge of the atom is unchanged. The daughter ^{37}Cl atom remains neutral, even though there is a vacancy in its inner shell —the hole resulting from the capture of a electron. As shown in Fig. 1.3, this initial state is unusual in three ways. First, the electronic configuration of the initial state in ^{37}Cl atom is like Cl in energy but resembles Ar in structure, *i.e.,* each energy level of the ^{37}Cl atom is relaxed from the Ar level to Cl level within the decay time but all levels except 1s are still fully occupied with electrons, as in the Ar case. Second, this initial state is a neutral state with a hole in the K-shell as compared to the ionized initial state obtained by conventional means. Third, with 90% of the electron capture occurring from 1s orbital, the initial state in the ^{37}Cl atom is almost a pure 1s vacancy state, while the initial states obtained by conventional means are mostly 2s and 2p vacancy states. This unique initial state provides valuable opportunities to study some atomic relaxation processes that were feasible in theoretical studies but impossible to probe with conventional experiments.

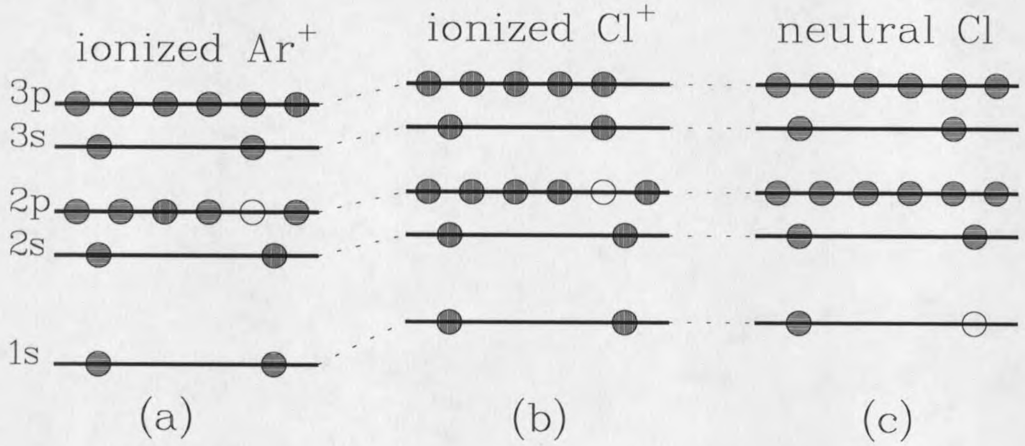

Figure 1.3 (a) and (b) Ionized initial state of Ar$^+$ and Cl$^+$ obtained by conventional means. (c) The unusual ^{37}Cl initial state obtained from electron capture decay.

There are two interesting relaxation processes for the unusual initial state studied in this work. The first one is the LMM and LLM Auger relaxation of this initial state. In an Auger process, the Auger peak energies and structures (splitting, satellite, etc.) are governed by the electronic configuration of the element studied. Therefore, the LMM and LLM Auger peaks of the ^{37}Cl atom are expected to be like Cl Auger in energy but resemble Ar Auger in structure. One purpose of this study is to look for possible shifts and new features in the Auger peaks and to compare them with known Cl and Ar Auger peaks.[29-39] The second relaxation process studied in this work is a particular phenomena called double Auger decay where the filling of the 1s hole causes *two* Auger electrons to be emitted simultaneously (Fig. 1.4). While having been predicted by theory, this phenomena has never been directly observed.[4, 40-43] Therefore another goal of this study is to measure the probability of the double Auger process and the energy distribution between the two double Auger electrons.

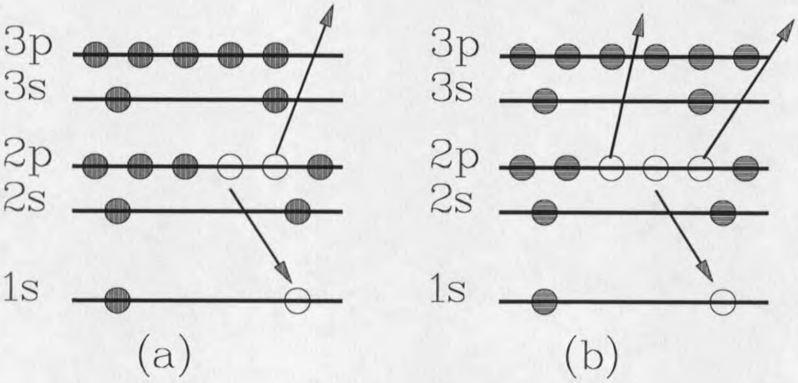

Figure 1.4 (a) Normal Auger transition. (b) Double Auger transition.

Historical Review of Related Works

Because this work straddles several disciplines including nuclear physics, surface physics and atomic physics, there is little that has been published to serve as a precedent.

Therefore, the review of the references is divided into each aspect of this research work: the ^{37}Cl ion recoil study, the desorption model study and the Auger relaxation study.

The first measurement of the recoil velocities of ^{37}Cl ions in the gas phase was reported in 1952.[44] Results of experimental[22,23] and theoretical[45] studies have since been reported on the recoil momentum and charge distribution of ^{37}Cl ions. The measurements of orbital electron capture ratios in this system have also been reported.[46,47] However, not much experimental work on the recoil velocities of ^{37}Cl ions has been reported since the 1950s. Previous experiments in the gas phase lacked the necessary resolution in the recoil spectra to search for a massive neutrino because of the effect of thermal velocities of ^{37}Ar atoms and the large size of the gas region seen by detectors. In this work ^{37}Ar atoms are localized by physisorbing them onto a well defined surface at a low temperature under ultrahigh vacuum conditions, where well known surface and nuclear physics techniques can be utilized to measure the recoil energies of the ^{37}Cl ions as well as other atomic and electronic properties of the surface species. The resolution of this work is expected to be much better than those in the gas phase experiments.

When an electron or a photon beam is incident on a surface with adsorbed atoms, electronic excitations will be generated by the interactions between the electrons or photons and the surface bonded complex, *i.e.,* the absorbates and the substrate surface. The decay of these electronic excitations may sometimes cause desorption. This is called *stimulated desorption.*[11] The studies on stimulated desorptions have become the focus of increased activities over the past three decades. The results and ideas generated in this rather specialized area of surface science have had an important effect on surface science and other disciplines.[9-12] Most of the existing work focuses on the study of desorption stimulated by low energy electrons (ESD) and photons (PSD). In 1964, Menzel, Gomer[48] and Redhead[49] developed the MGR theory to explain ESD on metal surface. Knotek and Feibelman[50] developed the K-F model in 1978 for the desorption in ionic systems. In 1979, Menzel and Franchy[25] explained the desorption due to Auger-like final states in covalent materials where the Auger decay of a core hole results in a final state with two or three valence holes. "Hence, we can envisage a 'Coulomb explosion' as observed in gas phase[91] molecules", they reported. Their report is very helpful in establishing the model for the desorption process in this research work. A comprehensive review of the stimulated desorption was given by Knotek in 1984.[11] There have been many papers reporting PSD and ESD studies of rare gases on metal or graphite surfaces by Menzel's group [51-60] and other research groups.[61-69] The reason for studying these desorption models is to develop a new model to understand the broadening of the recoil energy spectrum of the ^{37}Cl ions in the desorption process.

The Auger process was first observed seventy years ago. However, until the application of the lock-in amplifier by Harris in 1967, Auger signals were very hard to detect due to the small signal to noise ratio. Since the 1970s, Auger electron spectroscopy (AES) has become one of the most important surface analysis techniques.[70-75] The theoretical and experimental aspects of Auger emission have been comprehensively reviewed by Sevier[75] and Bambynek.[70] The K shell, L shell, M shell and Coster-Konig Auger transition rates for most atoms have also been calculated.[70,74,76] There have been many reports on Ar and Cl related Auger studies.[29-39, 77,78] In 1973, Siegbahn reported the LMM Auger study of Ar in the gas phase where they observed more than eighty peaks in their high resolution experiment.[29] Among these peaks, they attributed more than thirty to known electronic transitions. Their results were used as the reference energies for this research work. There are also results of the KLL Auger energies of Ar.[79-81] For the Auger decay of the initial state in this work, another good reference is the theoretical studies by Omar and Hahn, where they calculated the Auger lines produced by the decay of Ar ions with a deep 1s hole.[29-34] The first evidence of the double Auger decay process was reported by Krause's group in 1984.[40] Some other indirect evidence of this process was reported by Becker *et al* in 1989.[41] One of the few theoretical studies on the double Auger decay process was reported by Amusia *et al.* in 1992.[4] The experimental studies reported were concentrated on measuring the charge state distribution of the ions in the gas phase following a double Auger decay.[82,83] For example, the ordinary Auger decay of a neon atom in the gas phase will result in a doubly charged Ne^{2+} ion, therefore, the observation of triply charged Ne^{3+} ions would provide an indirect evidence of the double Auger decay process. There has not been much work on the direct measurements of the electrons emitted in the double Auger process.

CHAPTER 2

THEORY

Recoil Induced by Neutrino Emission

In today's theory of elementary particles, neutrinos belong to the family of *leptons.* There are three kinds of neutrinos, electron-type neutrino, muon-type neutrino and tau-type neutrino. They are involved in the nuclear reactions where electrons, muons or taus are created or annihilated.[84-86] A brief induction of neutrino physics is provided in Appendix A. In this section, the emphasis is put on calculating the recoil energy of the ^{37}Cl ions due to the emission of neutrinos in the electron capture reactions.

The object of this study is the ^{37}Ar isotope, which undergoes spontaneous electron capture decay ($^{37}\mathrm{Ar} \rightarrow {}^{37}\mathrm{Cl} + \nu_e$) with 814 keV total reaction energy.[8] The calculation in this section assumes that the electron capture decay is an ideal two-body problem which can be found in many physics text books. The conservation of energy and momentum dictates the recoil energy of the ^{37}Cl ions to be 9.54 eV if a massless neutrino is emitted in the EC decay. If neutrinos with different masses were emitted in this reaction, the ^{37}Cl ions would recoil with different kinetic energies. The recoil energy of the ^{37}Cl ion as the function of the neutrino mass is calculated below using relativistic kinematics.

The first step is to calculate the ^{37}Cl ion recoil energy, E assuming neutrino is massless ($m_\nu = 0$). Using natural units, *i.e.,* assuming speed of light, $c = 1$ and the Plank constant, $h = 2\pi$, the neutrino total energy E_ν has the form

$$E_\nu = P_\nu \tag{2.1}$$

where P_ν is the momentum of neutrino. The ^{37}Cl ion recoil energy, E can be written as

$$E = P^2/2M \tag{2.2}$$

where P and M are ^{37}Cl momentum and mass, respectively. Conservation of momentum and energy requires that

$$E + E_\nu = Q, \quad P = P_\nu \tag{2.3}$$

where $Q = 814$ keV is the total reaction energy. Therefore,

$$E + P = Q, \quad P^2 = E^2 - 2E \cdot Q + Q^2 \tag{2.4}$$

From Eq. (2.2) and Eq. (2.4) one can get

$$E^2 - 2(M + Q)E + Q^2 = 0 \tag{2.5}$$

Since $E << Q << M$, from Eq. (2.5) one can easily get

$$E \cong Q^2 / 2M = 9.54 \text{ eV} \tag{2.6}$$

The next step is to calculate the ^{37}Cl ion recoil energy, E', assuming that neutrino has non-zero rest mass. The total energy of the neutrino, E_ν', now has the form

$$E_\nu' = \sqrt{P_\nu'^2 + m_\nu^2} \tag{2.7}$$

where P_ν' and m_ν are the neutrino momentum and rest mass, respectively. Let P' be the momentum of the ^{37}Cl ion; then conservation of energy and momentum requires

$$E_\nu' + E' = Q, \quad P_\nu' = P' \tag{2.8}$$

From Eq. (2.8) and Eq. (2.9) one can get

$$E'^2 - 2(M+Q)E' + Q^2 = m_\nu^2 \tag{2.9}$$

The condition, $E' << Q << M$ still holds; therefore, Eq. (2.9) becomes

$$E' = (Q^2 - m_\nu^2)/2M \tag{2.10}$$

Comparing Eq. (2.6) with Eq. (2.10), the change of recoil energy, ΔE, due to the neutrino mass is

$$\Delta E = E - E' = m_\nu^2/2M \tag{2.11}$$

Finally, from Eq. (2.6) and Eq. (2.11), one can get the percentage change of the recoil kinetic energy of ^{37}Cl ion, $\Delta E/E$ due to the neutrino rest mass m_ν

$$\Delta E/E = (m_\nu/Q)^2 \tag{2.12}$$

From Eq. (2.12), it is easy to see that a neutrino with 250 keV mass ($E=mc^2$) would result in a percentage change, $\Delta E/E = 9.4\%$ in the recoil kinetic energy of the ^{37}Cl ion. This change corresponds to the difference of recoil energy from 9.5 eV to 8.6 eV. Such a change should be easily detectable in this experimental setup. Unfortunately, all of the above calculations are based upon ^{37}Ar atom being isolated. In reality the ^{37}Ar atom is physisorbed on a cold substrate where charge exchange and other interactions will take place. These interactions will broaden the recoil energy spectrum so that the recoil energy peak overlaps the energy difference, ΔE due to the neutrino mass. The next section is devoted to the discussion of these interactions.

Models on Stimulated Desorption

One of the primary goals of surface science is to understand the surface bond. The wide array of spectroscopic tools employed in this pursuit include the detection of electrons leaving the surface after excitation by radiation in the form of electrons, photons or ions. The surface bond or the local environment of an atom is deduced from the energy and angular distributions of these emitted electrons.[71-75,87] A completely different perspective can be obtained from the analysis of the atomic or molecular species leaving the surface as ions or neutrals. Techniques based on the detection of desorbing ions include electron stimulated desorption and photon stimulated desorption. These process are also called desorption induced by electronic transitions (DIET).[9-12, 48-69]

The electronic excitation leading to ion desorption can be a one-electron excitation, or much more complex and interesting, a multiple ionized and excited state. The dominant mechanism for creating these multiple excited states is the excitation of a core hole in the surface-bonded complex. The decay of these core-hole states results in the creation of multiple valence-hole final states which are much more efficient at inducing desorption than the one-electron excitations.[25] The multiple valence-hole states are intrinsically localized, contain a large amount of energy and have much longer life time than the normal electronic life times on surfaces.[25] In this experiment, the EC decay of ^{37}Ar produces not only a 9.54 eV recoil energy but also a highly excited core-hole state in the ^{37}Cl atoms. Just as in the DIET case, the decay of this initial state will provide additional energy to the ^{37}Cl ions. Therefore, in order to understand the complete recoil energy distribution, it is very important to understand these desorption mechanisms.

The Menzel-Gomer-Redhead (MGR) Model[48,49]

The MGR mechanism for desorption from surface is based on the elementary consideration that kinematic processes, *i.e.*, direct momentum transfer, are insufficiently energetic to cause desorption from surface. Hence, desorption must be due to an electronic excitation of the surface bond. The desorption can be envisaged as a two-step event, so that the desorption cross section has the form

$$\sigma = \sigma_e P \tag{2.13}$$

where σ_e is the primary excitation cross section and P is the escape probability. As shown in Fig. 2.1, the primary excitation is a vertical, Frank-Condon-like excitation from the bonding state (M+A) to the repulsive antibonding state (M+A)*, where M stands for the metallic substrate and A stands for the absorbed atom. This primary excitation is followed by an evolution of both electronic wave functions and nuclear coordinates along a new potential energy curve. The transition from (M+A)* to (M+A) is through the infinite set of states (M*+A) that differ from the (M+A) only by an excitation of the substrate, which

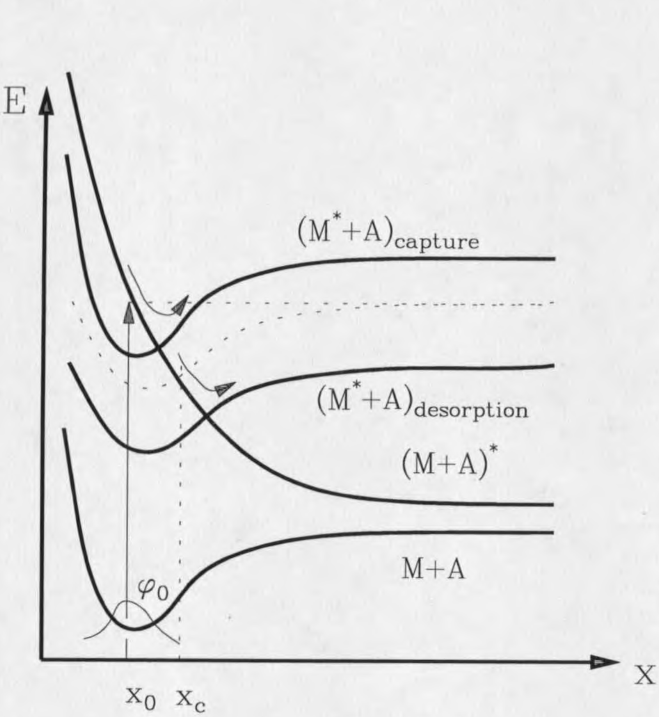

Figure 2.1 The energy level scheme of MGR model. The dash curve (M^*+A) intercepts the antibonding curve $(M+A)^*$ at a critical distance of x_c.

does not affect the bonding. Hence the curve (M^*+A) is identical to the (M+A) but raised in energy. The inverse of this de-excitation process, *i.e.* (M^*+A) → $(M+A)^*$ → desorption, while energetically feasible, is highly improbable because the excess energy in (M^*+A) is de-localized in the substrate and its re-localization in (M+A) bond is very unlikely, whereas (M+A) → $(M+A)^*$ implies an initial localization of the energy to be dissociated. Also as shown in Fig. 2.1, there is a critical distance x_c beyond which recapture cannot occur because the adsorbate A has sufficient energy to escape in the (M^*+A) state. The critical distance x_c is generally found to be ≤ 1 Å. Menzel and Gomer first treated the escape probability P in Eq. (2.13) as

$$P = \exp\left(-\int_0^{t_c}\frac{dt}{\tau}\right) = \exp\left(-\int_{x_0}^{x_c}\frac{dx}{v(x)\,\tau(x)}\right) \tag{2.14}$$

where $\tau(x)$ and $v(x)$ are the lifetime and velocity at position x. Since the reneutralization or de-excitation process involves resonance tunneling, it displays this exponential dependence on the distance from surface. P can then be approximated by

$$P = exp\,(\,-\Delta\tau / \tau\,) \tag{2.15}$$

where τ is assumed to be a constant from x_0 to x_c and $\Delta\tau = [2m\,(x_c - x_0\,) / S_r\,]^{1/2}$, where S_r is the slope of the repulsive curve. This then reduces to

$$P = exp\,(\,-\,c\,M^{1/2}\,) \tag{2.16}$$

where M is the molecular weight of the desorbed species and c is a constant. The energy spread of the desorbing ions can be approximated as

$$\Delta E = S_r\,(x_0)\,\Delta x \tag{2.17}$$

where Δx is the width of the ground state vibration wave function of the adsorbed species.

In 1980 Antoniewicz proposed a modification of the MGR model which recognized that if a species bonded on a surface is ionized, the attractive potential between the positive ion and its image will draw it to the surface. Ionic and neutral desorption then can occur by a mechanism illustrated in Fig. 2.2.[88] Initial excitations occur from (M+A) to some curves lying above the ionic curve (e.g. $(M^-+A^+)^*$). De-excitation from $(M^-+A^+)^*$ to (M^-+A^+) can then result in ion desorption (Fig. 2.2a). A much more obvious application of this model is to physisorption, where there is no bonding structure between A and the surface. Here an excitation from (M+A) to (M^-+A^+) again results in the ion being drawn toward the surface. Upon reneutralization and de-excitation back to (M^*+A) curve, the adsorbate is far enough up on the repulsive part of the curve to desorb. The ion must be drawn to the surface to a distance $X<X_c$ for desorption to occur (Fig. 2.2b).[89,90]

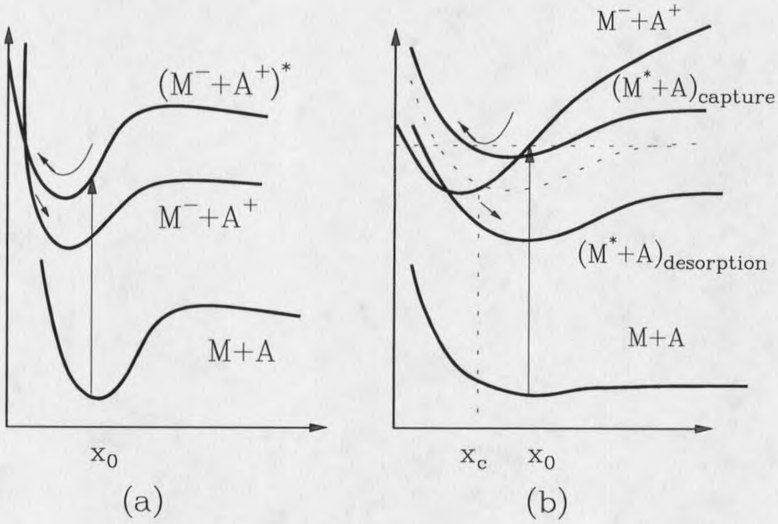

Figure 2.2 Energy level schemes of Antoniewicz Model. (a) Positive ion desorption. (b) Neutral desorption from a physisorption system.

There are some important points derived from these models. First, there exists a threshold for the primary excitations. ESD only happens when the primary electron energy is greater than the threshold. Second, there is a much larger ESD yield for neutrals than for ions. This is because the cross section, σ_e is larger for neutral ESD than ion ESD, and the escape probability *P*, in general, is much smaller for ions than for neutrals, since the processes to neutralize an ion are easier than those to recapture a neutral specie. All of the models discussed above involve only one-electron excitations of the surface bond. Models discussed in the next section will involve more complicated multielectron excited final states.

The Knotek-Feibelman (KF) Model[50]

There is a second general mechanism for desorption, which involves the excitation of a core level followed by the decay to complex desorptive final states rather than the one-electron excitations found in the MGR model. While it has since been generalized to a wide range of adsorption system, the original idea was developed to apply to the desorption of positive oxygen ions (O^+) from TiO_2, where oxygen is bonded in the O^{2-} state. The desorption process implies a large charge exchange where three electrons have to be transferred from the O^{2-} state to the O^+ state.

TiO_2 is called a maximal valency ionic compound. Maximal valency means that the cation is positively ionized to the noble-gas configuration (in NaCl , for example, Na loses the only one of its valence electron and becomes Na^+) and the anions are negatively ionized to the noble-gas configuration (*e.g.* Cl gains one electron and forms Cl^-). The highest occupied level of the Ti^{+4} ion is the Ti(3p) core level at 34 eV below the conduction band and the valence band of TiO_2 is almost exclusively O(2p) in character. Figure 2.3 shows a simplified schematic of the process leading to desorption of O^+ from a ground state of $Ti^{4+}O^{2-}_2$ configuration. As stated above, three electrons must be transferred from O^{2-} to yield O^+ desorption. If the primary ionization radiation removes the electron from the Ti atom's shallowest core, the predominant core-hole decay will be

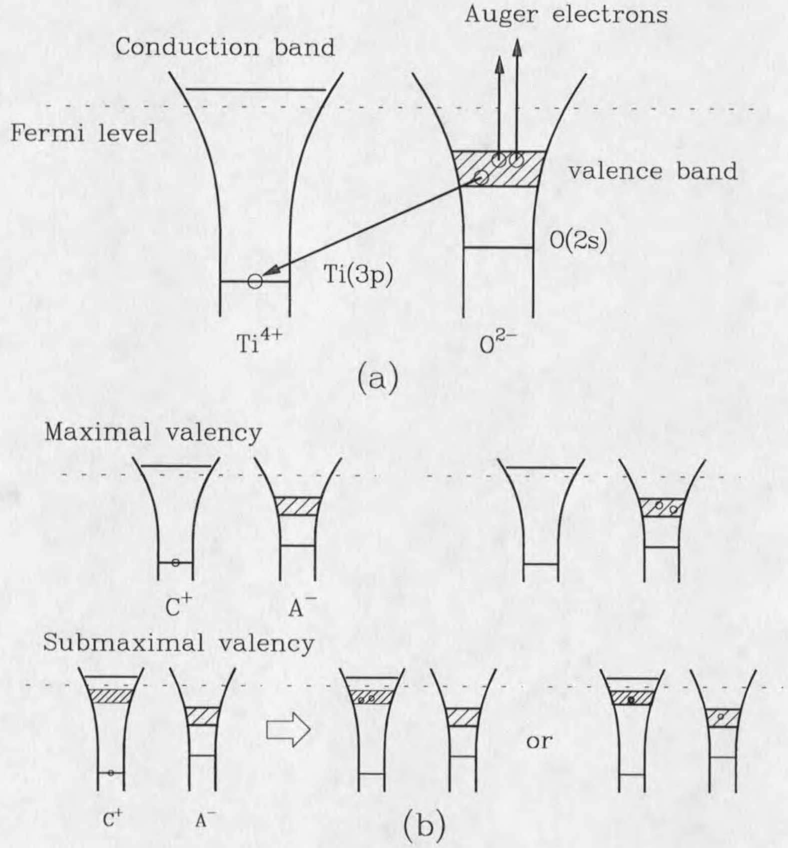

Figure 2.3 (a) The Knotek-Feibelman model for O^+ ion desorption from TiO_2. The initial hole in Ti(3p) is filled by an interatomic Auger transition in which the O^{2-} loses three electrons in its valance band and become the O^+ to desorb from the surface. (b) Comparison between maximal and submaximal valency compounds. Maximal valency results in selective charge transfer from anion A, leading to desorption. In submaximal, charge transfer is shared between cation C and anion A, quenching desorption.

an "interatomic" Auger process because the higher-laying electrons are lacking on the Ti atom. Thus, one valence electron from O^{2-} falls into the core hole and one or two electrons will be emitted from oxygen to release the energy of the decay. The loss of two electrons due to Auger transition and shake-offs (which can occur up to 10% of the time) from the oxygen orbital,[50] plus the third electron which fills the Ti(3p) hole transforms the oxygen to an O^+. The potential in which the O^{2-} is located before the excitation and Auger sequence is the sum of an attractive Madelung term and repulsive core overlap contribution. In its negative state, the atom is in a stable position defined by the minimum in the total potential. However, if the charge on the oxygen changes sign, the Madelung term becomes also repulsive. Thus the oxygen is now in a total repulsive potential and is driven to desorb if it is on the surface.

Another way to cause the desorption of O^+ from TiO_2 is to excite anions (O) instead cations (Ti). In fact, by exciting the M_{23}, M_1, L_{23} and L_1 levels of titanium or L_1 and K levels of oxygen one can get different yields of O^+ depending on the energy available from the core-hole decay and the details of the decay process. Energy conservation becomes important when the core hole is shallow enough that not enough energy is released by decay of an electron from the top of the valence band, or highest valence level, to transfer the necessary charge to cause desorption. Now consider the ionization of the anion A^- to an A^0 and subsequently to an A^+. The first electron drops into the core hole leaving a single valence hole on the anion (A^0) and releasing an energy, *E*. This energy is then available to ionize the A^0 to A^+. If the anion has an ionization energy, I, and the solid has an electron affinity, A, then the available energy, E, must satisfy the condition

$$E > I - A + T \tag{2.18}$$

where T is the extra energy required to remove an electron out of the Madelung potential. The energy T is converted into kinetic energy of the ions as it leaves the surface. If the anion was originally an A^{2-}, then the loss of a valence electron leaves an A^{-}. Removal of a second electron requires an energy equal to the gap energy, E_g plus the screened hole-hole repulsion energy, U. The subsequent $A^0 \rightarrow A^+$ proceeds as before, so the minimum energy condition is

$$E > E_g + U + (I - A + T) \tag{2.19}$$

A good approximation to an unscreened value of U for an atomic species is the difference between its first and second ionization potential.

$$U = I_2 - I_1 \tag{2.20}$$

These conditions are very important for modeling charge exchange and Coulomb repulsion of the desorbing ^{37}Cl ions with their neighbors in this work.

Desorption Due to "Coulomb Explosion" [25]

While the original formulation of the Auger model was to explain the desorption of ions from ionically bonded surfaces, it was soon demonstrated that ions could be desorbed from covalently bonded surface complexes by essentially the same mechanism. In the simplest analysis, the product of an Auger decay of a core hole in a covalent system is a two or three valence-hole final state. Hence, one can envisage a "Coulomb explosion" as observed in gas-phase[91] molecules, where the highly repulsive final state results in the production of ionic fragments of the parent species. The presence of multiple valence holes in a covalent system can result in a repulsive interaction between the unscreened nuclei and subsequent production of ion fragments. The multiple holes thus represent energy stored in the bond. When two holes exist on an atom or in a bond the most obvious way to relieve the large repulsive energy is for one hole to hop away before nuclear motion can occur. Typical uncorrelated one-hole hopping times are of the order of 10^{-16} s, whereas desorption times are of the order of 10^{-13} s. So the life time of hole is too short to affect the motion of nuclei. However, one-hole hopping is often slowed by hole-hole correlation which can block resonant one-hole hopping process. The importance of hole-hole correlation was first pointed out by Cini[92] and Sawatsky[93] in explaining the existence of atomic-like Auger spectra in marrow d-band metals. This process has also been observed in insulators[94] and gas-phase molecules.[95] This many-body effect can make the Auger-induced desorption process effective for covalent materials as well as ionic materials.[96-100]

Now consider a simple Hubbard-like Hamiltonian, as in Eq. (2.21), describing an electron in a system with bandwidth W. When two holes are created on an atom or in a bond, the correlation energy between the two holes is given by $U_{eff.}$, which can have important contributions due to screening.[92,93-95]

$$H = \sum_{i\sigma} \varepsilon_b C_{i\sigma} C^+_{i\sigma} + \sum_{ij\sigma} W_{ij} C^+_{i\sigma} C_{j\sigma} + \sum_{i} U_{eff} C^+_{i\vee} C^+_{i\wedge} C_{i\vee} C_{i\wedge} \qquad (2.21)$$

Figure 2.4 displays the terms in this Hamiltonian schematically. Typical one-hole hopping times in such system are of order of $\tau \approx 1/W$ (Fig. 2.4 (a)). If $U_{eff} > W$, resonant one-hole hopping is essentially blocked and $\tau >> 1/W$, because it involves either energy transfer during the transition or a complicated multiple-hole motion (Fig. 2.4 (b)).[92,93] The highly repulsive Auger final state is thus given an intrinsically long life time due to this

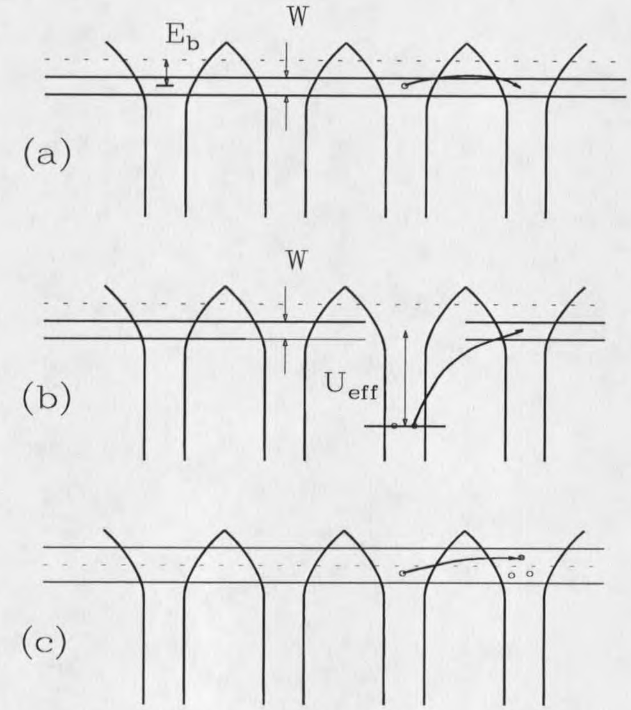

Figure 2.4 Schematic displaying terms of a Hubbard Hamiltonian with intrasite Coulomb term U_{eff}. (a) Single valence hole $\tau \approx 1/W$. (b) Two valence-hole states with $U_{eff} > W$ have one or two hole hopping $\tau >> 1/W$. (c) Presence of unfilled orbital can provide fast charge transfer channel hence reduces the chance of desorption.

correlation, possibly of the order of 10^2 times the normal one-hole lifetime, which allows sufficient time for nuclear motion to relieve the energy. Therefore, factors which increase U_{eff} and /or decrease W will enhance desorption.

U_{eff} contains both an intrasite Coulomb repulsion term and a screening term.[95] The intrasite (or intrabond) repulsion term is roughly approximated for atoms by the difference between the second and first ionization potential (Eq. (2.20)) and is inversely proportional to the ionic radius. The screening term is enhanced by the presence of unsaturated bonding, which allows very efficient charge transfer to occur (as shown in Fig 2.4(c)), hence reduces the chance of desorption.[92-95] The transfer of a charge onto the atom from a neighbor is equivalent to the hole being transported from screened site, both from the standpoint of energy and total charge.

In this work, the ^{37}Cl ion has an initial state with one core hole which will also result in multiple-hole final states. One of the channels to release the trapped energy in these multiple-hole states is the hopping of one of the holes from ^{37}Cl ion to its neighbor, or equivalently, transferring one electron from the neighbor to ^{37}Cl ion. Further hopping of the holes may be blocked because of energy restriction, *e.g.,* a single charged ^{37}Cl$^+$ ion cannot exchange charge with a neighboring Ar atom because the first ionization potential of Cl is less than that of Ar. Therefore, there is enough time for the ^{37}Cl nucleus to move. The ionized ^{37}Cl atom will obtain the kinetic energy through Coulomb interaction with its neighbor ions. The details of this model will be developed later.

Theory of Auger Transition

Auger Effect

The inner shell vacancy of an atom with multiple electrons can be created by photon irradiation,[87] energetic electron irradiation[70-75] or in this work, an electron capture process. Two of the channels the excited initial state can decay through are the radiative transition where an electron in a higher energy level jumps down to the vacancy and releases energy in the form of a photon, and the non-radiative transition where an electron in higher energy level jumps down to the vacancy with the energy transferred to another electron to escape from the atom. The latter transition is called Auger effect.[70-75]

Table 2.1 Number of Electrons, Symbols and Energies (eV) for Ar and Cl Core Levels[24]

n	1	2				3			
1	0	0	1		0	1		2	
j	1/2	1/2	1/2	3/2	1/2	1/2	3/2	3/2	5/2
# of *e*	2	2	2	4	2	2	4	4	6
Symb	K	L_1	L_2	L_3	M_1	M_2	M_3	M_4	M_5
E_{Ar}	3202.9	320.0	247.3	245.2	25.3	12.4	12.4		
E_{Cl}	2822.4	270.2	201.6	200.0	17.5	6.8	6.8		

An atom with multiple electrons can be approximately described in terms of single electron wave functions, single electron states and energy levels. These wave functions are usually calculated by self-consistent methods. If spin-orbit coupling is considered, a single electron state can be described by the four quantum numbers *n, l, j* and m_j. as shown in Table 2.1. Where *n* is the principle quantum number, *l* is the orbital angular momentum quantum number, *j* is the total angular momentum quantum number and m_j is the quantum number for the *z*-component of the total angular momentum. An Auger transition can be described by three letters as W_i X_p Y_q where W_i stands for the initial state core hole, X_p and Y_q stand for the two holes in the final state.

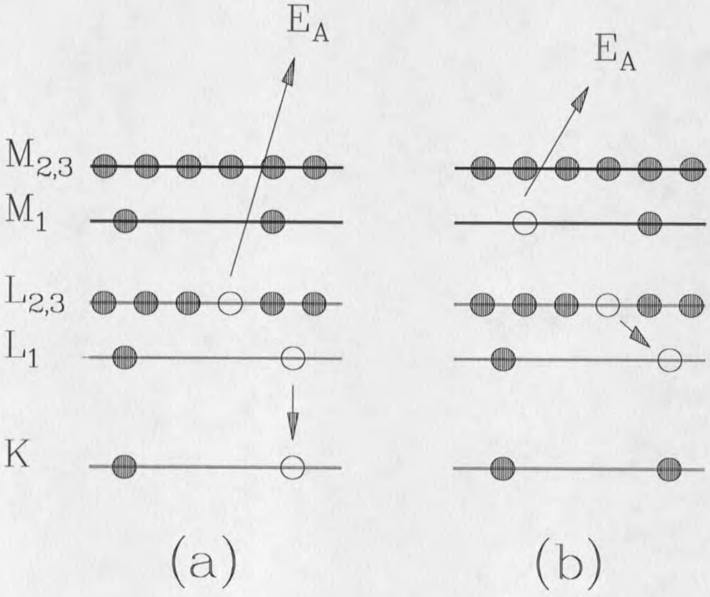

Figure 2.5 (a) KLL Auger transition. (b) LLM Coster-Koing Auger transition.

The Auger transitions involving $n = 1$ and $n = 2$ levels are called KLL Auger series. In fact, there are six possible transitions in this series, KL_1L_1, KL_1L_2, KL_1L_3, KL_2L_2, KL_2L_3 and KL_3L_3. If one of the final state holes is in the same shell as the initial hole, such as $L_1L_2M_1$, this kind of Auger process is called Coster-Konig (C-K) transition as shown in Fig. 2.5. A C-K transition has a much shorter life time than the regular Auger process.[70,74,76] Therefore, according to the uncertainty principle, $\Delta E \cdot \Delta t \geq h/2\pi$, the energy spreads of the C-K transitions are larger than those of regular Auger transitions. Sometimes the energy spread of a C-K transition can reach as high as 10 eV. The C-K transitions can also affect the probabilities of other Auger transitions. For example, the existence of an $L_iL_pY_q$ C-K transition will reduce the chance for an L_iXY Auger transition and increase the chance for an L_pXY Auger transition.[76] The effects of the C-K transition might play an important role in explaining the features in the ^{37}Cl Auger spectrum.

The discussion above agrees quite well with Auger experiments for large Z-number atoms. However, it is not quite accurate when applied to middle range or small Z-number atoms. For example, there are five KLL peaks for Ar instead of the six predicted above. The reason for this is the complexity of the angular momentum coupling of the two holes in final states of the Ar atom. Since each subshell in the Ar atom is fully occupied with electrons before the transition, the orbital, spin and total angular momentum in these subshells are all zero ($L = S = J = 0$). These subshells are called closed subshells. According to quantum mechanics, the coupling of two holes is identical to the coupling of two electrons in a closed subshell. For Ar KLL Auger transition, the two holes in the final state are all in the L-subshell. These two holes are coupled with the Russell-Saunders coupling scheme or the L-S coupling model.[75] In this coupling model, the total spin angular momentum, S is formed by adding the spin angular momentum of the two holes, s_1 and s_2, *i.e.*, $S = s_1 + s_2$. The total orbital angular momentum, L is formed by adding the orbital angular momentum of the two holes, l_1 and l_2, *i.e.*, $L = l_1 + l_2$. Then the total angular momentum, J is formed by adding the total spin and orbital angular momentum, *i.e.*, $J = S + L$. The adding of two angular momentum is accomplished according to the angular momentum addition rule in quantum mechanics, *e.g.*, $J = |L-S|$, $(L\text{-}S+1)$, ..., $(L+S)$. An L-S coupled state can be expressed in the form of the *spectral term*, ${}^{2S+1}L_J$. The KLL series of Ar Auger has six final states described in spectral terms, ${}^1S_0$, ${}^1P_1$, ${}^3P_{2,1,0}$, ${}^1S_0$, ${}^3P_{2,1,0}$, and ${}^1D_2$. as shown in Table 2.2, where ${}^3P_{2,1,0}$ is excluded for violating the conservation of parity. An Auger transition with L-S coupling in its final state is usually described by the spectral term and the WXY symbol. For example, the symbol $KL_1L_1({}^1S_0)$ describes a KL_1L_1 Auger transition whose final state has zero spin angular momentum, zero orbital angular momentum and zero total angular momentum.

Table 2.2 Final States of Ar KLL Auger Series[81]

Final State Holes	Spectral Terms
$2s^2p^6$	${}^1S_0$
$2s^12p^5$	${}^1P_1$, ${}^3P_{2,1,0}{}^*$
$2s^22p^4$	${}^1S_0$, ${}^3P_{2,1,0}$, ${}^1D_2$

*${}^3P_{2,1,0}$ is excluded for violating the conservation of parity.

Auger Energies and Intensities

Since the Auger transitions are determined by the electronic configuration of the atom studied, each element has its own set of Auger peaks with characteristic energies and structures.[70-75] The energy of the Auger electrons can be in principle determined by the difference of the total energies before and after the transition. Supposing an isolated atom with atomic number Z undergoes an Auger transition *WXY*, the energy available for an *X* electron to fill the *W* vacancy is $E_W(Z) - E_X(Z)$, where $E_W(Z)$ and $E_X(Z)$ are the binding energies of electrons at the *W* and *X* levels. Therefore the kinetic energy of the *Y* electron obtained in this Auger transition is

$$E_{WXY}(Z) \cong E_W(Z) - E_X(Z) - E_Y(Z) \tag{2.22}$$

where $E_Y(Z)$ is the binding energy of an electron in the *Y* level. Eq. (2.22) is an approximation because $E_Y(Z)$ is the binding energy of the *Y* level when all the inner shells below the *Y* level are filled, whereas in Auger transition a hole exists below the *Y* level. Therefore it takes a higher energy, $E_Y'(Z)$ to ionize an electron from the *Y* level due to less screening. In fact, $E_Y'(Z)$ is between $E_Y(Z)$ and $E_Y(Z+1)$.[75]

$$E_Y'(Z) = E_Y(Z) + \beta[\, E_Y(Z+1) - E_Y(Z)\,] \tag{2.23}$$

where β is between zero and one. Hence, the Auger energy of the *WXY* transition is

$$E_{WXY}(Z) = E_W(Z) - E_X(Z) - E_Y(Z) - \beta[\, E_Y(Z+1) - E_Y(Z)\,] \tag{2.24}$$

Similarly, the Auger energy of the *WYX* transition is

$$E_{WYX}(Z) = E_W(Z) - E_Y(Z) - E_X(Z) - \beta'[\, E_X(Z+1) - E_X(Z)\,] \tag{2.25}$$

From a quantum mechanics point of view, the *WXY* transition is identical to the *WYX* transition. Therefore, $E_{WXY}(Z)$ is equal to $E_{WYX}(Z)$. A semi-empirical way to calculate the Auger energy is to take the average of $E_{WXY}(Z)$ and $E_{WYX}(Z)$ and set β and β' to be unity[101]

$$E_{WXY}(Z) = E_W(Z) - 1/2\,[\,E_X(Z+1) + E_X(Z)\,] - 1/2[\,E_Y(Z+1) + E_Y(Z)\,] \qquad (2.26)$$

The Auger electrons emitted from solid have to overcome the work function, φ_S. The Auger electron energy, $E_{WXY}'(Z)$ then becomes

$$E_{WXY}'(Z) = E_{WXY}(Z) - \varphi_S \qquad (2.27)$$

By reaching the electron analyzer with work function φ_A, the Auger electron energy, $E_{WXY}''(Z)$ then becomes

$$E_{WXY}''(Z) = E_{WXY}(Z) - \varphi_A \qquad (2.28)$$

Their relations are shown in Fig. 2.6.

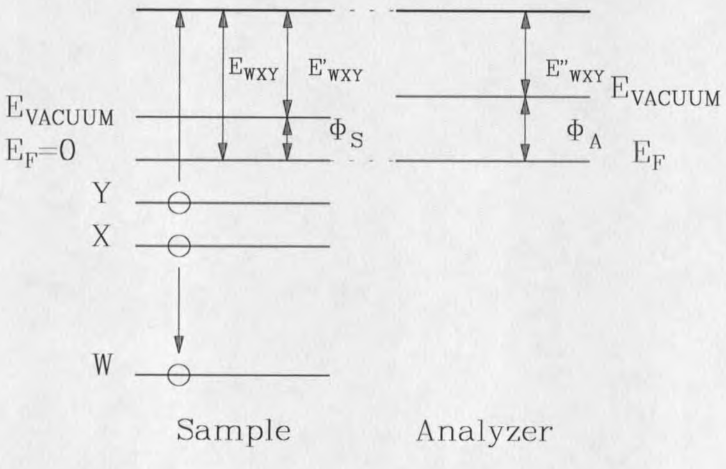

Figure 2.6 Relation between Auger electron energy E_{WXY} and the kinetic energy when Auger electron reaches analyzer, E''_{WXY}

For a conventional Auger process whose initial vacancy is created by electron or photon irradiation, both the initial ionization cross section and the Auger transition probability contribute to the intensities of Auger peaks.[75] The situation is much simpler in this work where the initial vacancy is created by electron capture. Thus the Auger peak intensities will be proportional to the Auger transition probabilities. By calculating the electron-electron interaction the Auger transition probability, W_A can be calculated by the Golden Rule as

$$W_A = \frac{2\pi}{h}\left|\iint \rho(k)\phi_f(r_1)\,\phi_f(r_2)\frac{e^2}{|r_1 - r_2|}\phi_i(r_1)\,\phi_i(r_2)dr_1dr_2\right|^2 \qquad (2.29)$$

where $\rho(k)$ is the state density and $\phi_f(r_1)$ is the initial hole state, $\phi_i(r_1)$ and $\phi_i(r_2)$ are the states electrons come from and $\phi_f(r_2)= e^{ik\cdot r}$ is the emitted Auger electron.[75]

All of the above discussions are based on the one-electron approximation and the assumption that the electron-electron interaction is weak enough so that it does not shift too much the core levels, distort the charge distribution or modify the transition rates. However, these conditions do not always hold and in those cases the one-electron orbital picture will break down. The electron-electron interaction induces shake-up and shake-off effects, where the transition of one electron causes another electron to be excited to a higher energy level or above the vacuum level. These effects make the Auger spectra much more complex. A self-consistent treatment will be needed for these kinds of Auger transitions.[102] Some theoretical and experimental results on Ar LMM Auger energies, intensities and transition probabilities are listed below in Table 2.3 and Table 2.4.

Table 2.3 Ar LMM Auger Peak Energies and Relative Intensities.

Transitions	E_{cal}(eV)$^+$	Spectral Terms	E_{exp}(eV)$^{++}$	Intensity(ab.)$^{++}$
$L_2 M_{2,3} M_{2,3}$	207	$^3P_{0,1,2}$	207.23	139
		$^1D_2$	205.62	183
		$^1S_0$	203.23	55
$L_3 M_{2,3} M_{2,3}$	205	$^3P_{0,1,2}$	205.21	272
		$^1D_2$	203.47	270
		$^1S_0$	201.09	100
$L_2 M_1 M_{2,3}$	193	$^3P_{0,1}$	193.08	37
		$^1P_1$	189.49	32
$L_3 M_1 M_{2,3}$	191	$^3P_2$	191.13	87
		$^1P_1$	187.33	53
$L_2 M_1 M_1$	178	$^1S_0$	180.06	18
$L_3 M_1 M_1$	176	$^1S_0$	177.91	34

$^+$ Calculated from Eq. (2.26) to Eq. (2.28) and taking φ_A=5.0 eV; $^{++}$ Reference [29]

Table 2.4 (a) Ar Auger Transition Probabilities (%) for a K-hole Initial Vacancy.[76]

KL_1L_1	KL_1L_2	KL_1L_3	KL_1M_1	KL_1M_2	KL_1M_3	KMM
6.89	7.59	14.54	1.53	0.71	1.36	0.67
	KL_2L_2	KL_2L_3	KL_2M_1	KL_2M_2	KL_2M_3	
	1.39	34.44	0.74	0.25	2.87	
		KL_3L_3	KL_3M_1	KL_3M_2	KL_3M_3	
		19.55	1.42	2.87	3.30	
KL_1L_1=6.89% $KL_1L_{2,3}$=22.13% $KL_{2,3}L_{2,3}$=55.38% KLM=15.05% KMM=0.67%						

Table 2.4 (b) Ar Auger Transition Probabilities (%) for L-hole Initial Vacancies.[76]

$L_1L_2M_1$	$L_1L_2M_2$	$L_1L_2M_3$	$L_1L_3M_1$	$L_1L_3M_2$	$L_1L_3M_3$	$L_1M_2M_3$	$L_1M_3M_3$
17.81	7.42	7.50	34.68	7.33	20.83	.007	.068
$L_1M_1M_1$	$L_1M_1M_2$	$L_1M_1M_3$	$L_{2,3}M_1M_1$	$L_{2,3}M_1M_2$	$L_{2,3}M_1M_3$	$L_{2,3}M_2M_3$	$L_{2,3}M_3M_3$
.769	1.20	2.39	1.09	0.72	22.83	31.63	45.00
$L_1L_{2,3}M_1$=52.50% $L_1L_{2,3}M_{2,3}$=43.07% L_1MM=4.43% $L_{2,3}M_1M$=24.64% $L_{2,3}M_{2,3}M_{2,3}$=76.36%							

In this thesis work, the emphasis is put on the study of Auger decay cascades of the initial hole in the K-shell of ^{37}Cl atom, especially, the LMM Auger transitions. As discussed in the Chapter 1, the LMM Augers of ^{37}Cl are expected to be similar to the Ar Augers in structure and Cl Augers in energy. The above tables provide a very convenient

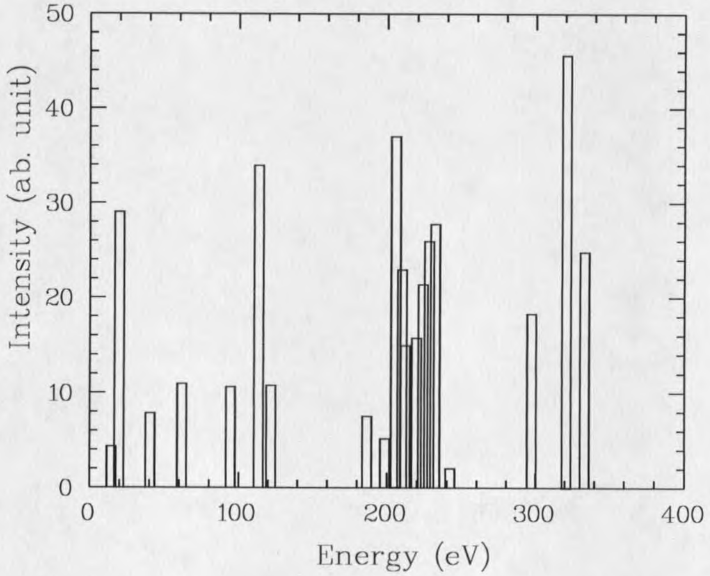

Figure 2.7 The Auger spectrum predicted by the RACS for Ar with the initial 1s hole.

reference for the comparison. The similar case like the decay of the ^{37}Cl initial state can only be found in the theoretical calculation. In 1992, Omar and Hahn reported the study of the decay of an Ar atom with a 1s-hole.[29-34] All possible Auger transitions with their shake-ups and shake-offs during the production and decay of an initial 1s hole in Ar are calculated by using the model of radiative Auger cascade transitions with the shake-off effect (RACS). The calculated Auger spectrum[31] is shown in Fig. 2.7. After Auger decay, the Ar atom is ionized in different charge states.[29-34] The charge states of the Ar ions are determined by the different decay channels and shake-offs. Omar and Hahn also calculated the final charge state distribution of Ar ions (FCSD) as shown in Table 2.5.[33]

Table 2.5 The Final Charge States of Ar after Auger Transitions of an 1s Initial Hole.

Charge	1	2	3	4	5	6	7
$Y_{RACS}(\%)$[31]	0.8	6.8	10.0	42.4	28.0	10.3	1.7
$Y_{EXP1}(\%)$[104]		2.2	8.8	41.5	33.3	11.5	2.7
$Y_{EXP2}(\%)$[103]		9.9	8.8	43.9	25.8	9.9	1.3

Double Auger Transition

In a normal Auger process, filling of a vacancy in an inner shell by an outer-shell electron leads to the emission of a second outer-shell electron. However, if the initial vacancy is in a deep inner shell, the transition of the outer-shell electron can sometimes cause the ejection of two electrons simultaneously (Fig. 1.4(b)). This transition is called a double Auger decay process.[4, 40-43] The double Auger decay process was first reported by Carlson and Krause from the observation of Ne^{+3} ions in the gas-phase Ne Auger decay.[40] They concluded that the double Auger decay process accounted for the creation of Ne^{+3} ions because in a normal Auger process a Ne atom could not lose three electrons at the same time. From the yield of Ne^{+3} ions they also concluded that double Auger decay probability was about 8%.[40]

In the one-electron model, the double Auger decay probability has to be zero because the initial ψ_i and final ψ_f wave functions differ by more than two one-electron states. In this case, the matrix element $\langle \Psi_f | V = 1/r_{12} | \Psi_i \rangle$ determining the amplitude of the double Auger process is zero. Therefore, many-electron correlation has to be taken into account to calculate the double Auger decay probability. By using many-body perturbation theory,[4] the amplitude M of the double Auger decay can be calculated from the electron-electron interactions, $\sum_{i=1}^{9} M_i$ as shown in Eq. (2.30) and Fig. 2.8.

$$\begin{aligned}
M_1 &= \sum_k \frac{\langle iq_1|U|f_1k\rangle\langle kq_2|U|f_2f_3\rangle}{\varepsilon_i + \varepsilon_{q_1} - \varepsilon_{f_1} - \varepsilon_k}; \\
M_4 &= \sum_k \frac{\langle q_1q_2|U|f_1k\rangle\langle kq_1|U|f_1f_2\rangle}{\varepsilon_{q_1} + \varepsilon_{q_2} - \varepsilon_{f_1} - \varepsilon_k}; \\
M_7 &= \sum_k \frac{\langle iq_2|U|f_1k\rangle\langle kq_1|U|f_2f_3\rangle}{\varepsilon_i + \varepsilon_{q_2} - \varepsilon_{f_1} - \varepsilon_k}
\end{aligned} \tag{2.30}$$

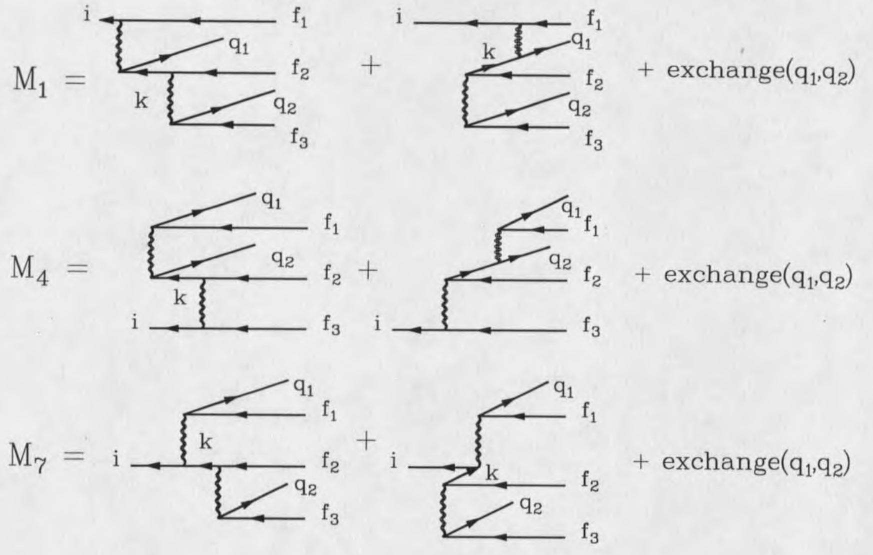

Figure 2.8 Brueckner-Goldstone diagrams for the partial amplitudes M$_1$, M$_4$ and M$_7$. Lines with arrows to the left and to the right denote holes and particles, respectively.

Where M$_i$ are the partial amplitudes of the process and $\langle pq|U|rs\rangle = \langle pq|V|rs\rangle - \langle pq|V|sr\rangle$ is the difference of the "direct" and the "exchange" matrix elements of the Coulomb interaction; *i* is the initial vacancy and f_1, f_2, f_3 are the final vacancies; q_1 and q_2 are the double Auger electrons; and ε is the one-particle Hartree-Fock energy. Other amplitudes (M$_2$, M$_3$, M$_5$, M$_6$, M$_8$ and M$_9$) can be obtained out of M$_1$, M$_4$ and M$_7$ by the cyclic replacement of the elements f_1, f_2 and f_3, respectively. Summation over *k* in Eq. (2.30) implies the summations over hole and discrete electron levels and integration over continuous electron spectra. Figure 2.8 shows the Bruckner-Goldstone diagrams of the partial amplitudes M$_1$, M$_4$ and M$_7$. The transition energy in a double Auger decay can be expressed as

$$E_{tot} = E_f - E_i \tag{2.31}$$

where E_f and E_i are the energies of initial and final states, respectively. The energy E_{tot} is continuously distributed between the two emitted electrons. Therefore, the total probability of the double Auger decay process is determined by the expression

$$\Gamma_i^{DA} = \int_0^{E_{tot}} \gamma(E_1) \tag{2.32}$$

where $\gamma(E_1)$ is the probability that the first electron, *e.g.*, q_1 has the energy E_1. The energy E_1 is given by

$$\gamma(E_1) = 2\pi|M|^2 \tag{2.33}$$

There are several models which can be derived from the diagram above. The first one is the virtual inelastic scattering model as shown in Fig. 2.9(a) where the imaginary part of M_4 dominates in the total amplitude, *i.e.*,

$$|M| \approx |\mathrm{Im}\, M_4| \approx \langle k_0 i|U|f_2 f_3\rangle\langle q_1 q_2|U|f_1 k_0\rangle \tag{2.34}$$

where k_0 is an "intermediate" Auger state that satisfies $\varepsilon_0 = k_0^2/2m$ and $\varepsilon_0 = \varepsilon_{f_2} + \varepsilon_{f_3} - \varepsilon_i$. In this case, a normal Auger decay of the initial hole i occurs and the intermediate state k_0 is created; then the k_0 state is inelasticly scattered by electron in f_1 state. The total probability in this case is

$$\Gamma_i^{DA} \approx \Gamma_{i \to f_2 f_3 k_0}^{A} \sigma_{k_0} \tag{2.35}$$

where $\Gamma_{i \to f_2 f_3 k_0}^{A}$ is the probability of normal Auger decay and σ_{k_0} is the cross section of the inelastic scattering of the k_0 Auger electron with an electron in an f_1 state. The energy distribution between the two outgoing electrons is determined by the inelastic scattering process of the k_0 Auger electron, and if ε_0 is high enough, $\varepsilon_{q_2} >> \varepsilon_{q_1}$.

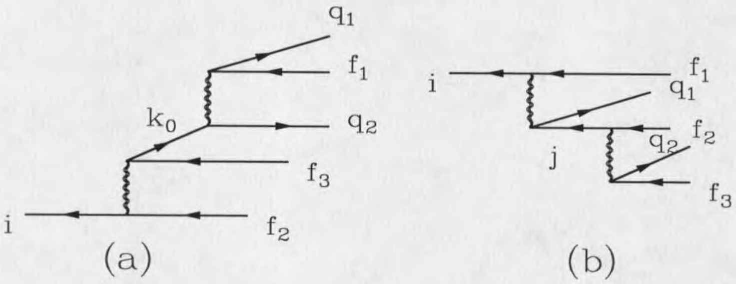

Figure 2.9 (a) Virtual inelastic scattering model. (b) Cascade mechanism.

The second model of the double Auger decay process is the cascade mechanism as shown in Fig. 2.9(b) The initial hole i can decay through the normal Auger transition, producing a vacancy in one of the intermediate shells. This intermediate vacancy, in turn, can decay via another Auger transition. The corresponding probability for this model is

$$\Gamma_i^{DA} \approx \Gamma^A_{i \to f_1 j q_1} \Gamma^A_{j \to f_3 q_2} \Gamma_j^{-1} \tag{2.36}$$

where j is the intermediate hole and Γ_j is the total width of this hole. The energy spectrum has two lines centered at $\varepsilon_{q_1} = \varepsilon_{f_1} + \varepsilon_j - \varepsilon_i$ *and* $\varepsilon_{q_2} = \varepsilon_{f_2} + \varepsilon_{f_3} - \varepsilon_j$.

The third model of double Auger decay is the shake-off model where the initial hole, i decays through normal Auger decay, $i^{-1} \to f_1^{-1} f_2^{-1} + q_1$. Then, the atomic field caused by this transition shakes off another electron q_2 from the f_3 level. The probability of the double Auger decay process for this model is

$$\Gamma_i^{DA} = \Gamma_{i\to f_1 f_2 q_1}^{A} \left| \langle q_2 | f_3 \rangle \right|^2 \tag{2.37}$$

where the second factor is the overlap integral. There are all together six combinations out of q_1, q_2 and f_1, f_2, f_3 states for the overlap term. The energy distribution between the two electrons, ε_{q_1} *and* ε_{q_2}, is highly asymmetric, *i.e.,* one of them takes most of the E_{tot} and the other has little share of the energy.

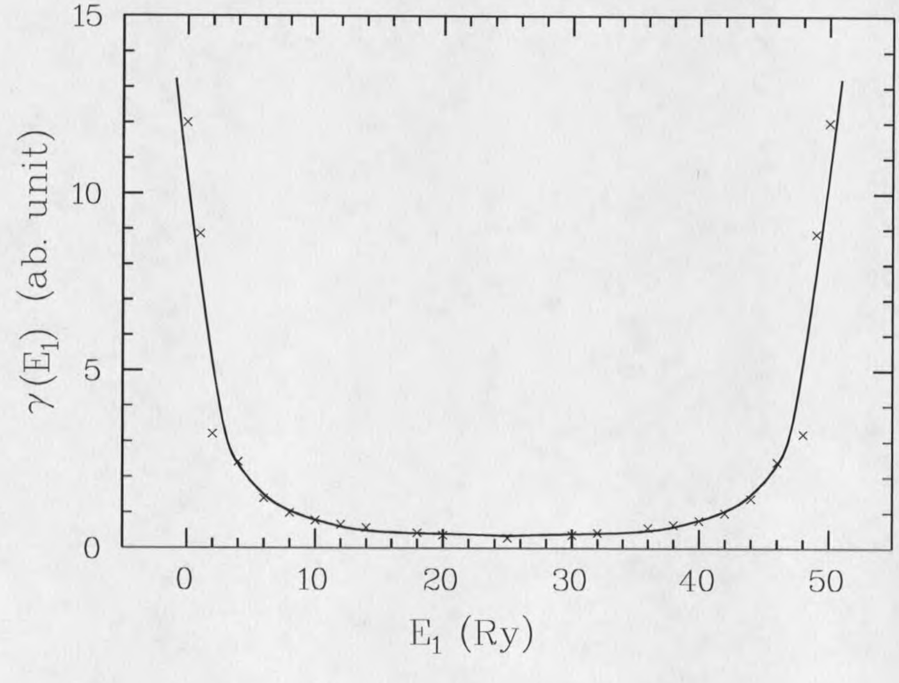

Figure 2.10 Dependence of the double Auger decay probability on the energy of one of the outgoing electrons in the Ne $1s^{-1} \rightarrow 2s^{-2}\ 2p^{-1} + q_1 + q_2\ (^2S)$ double Auger transition. Calculated by many-body perturbation theory.

The results of the many body perturbation theory (MBPT) calculation of the energy distribution of the two electrons for Ne double Auger decay[4] are shown in Fig. 2.10. It is clear that the electrons share the E_{tot} in the way that one of them takes most of the energy and the other takes the small balance of the energy. Since there are very few references on the double Auger decay,[4, 40-44] the experiment results of this research work on the double Auger decay probability and the energy distribution will be compared with the theoretical calculation of the Ne work[4] quoted above.

CHAPTER 3

EXPERIMENT

Experimental Setups

The main feature of this experiment is to measure the time-of-flight of the recoiled ^{37}Cl ions by using coincidence techniques.[105-109] The ^{37}Ar atoms were physisorbed on a cold flat substrate inside an UHV system. When electron capture occurs, the ^{37}Ar nucleus becomes a ^{37}Cl nucleus and a neutrino is emitted. The recoil due to the emission of neutrino could cause the ^{37}Cl ion to desorb from the substrate (Fig. 1.1, Fig. 1.2). Meanwhile, the capture of a deep core-level electron in the ^{37}Ar atom would also result in a highly excited initial state in the daughter ^{37}Cl atom. This initial state could then decay through radiative (x-ray) or non-radiative (Auger) relaxation and cause the ionization of the ^{37}Cl atom. Therefore, if the desorption were to happen, both the ^{37}Cl ion and the Auger electron would escape from the surface simultaneously. By using two detectors with one of them detecting ions and the other detecting selected Auger electrons, the time-of-flight of the ^{37}Cl ions could be obtained by comparing the time difference between ions and electrons arriving at the two detectors. Because the electrons are much faster than the ions, this time difference is essentially the time-of-flight of the

^{37}Cl ions. The difficult part in this experimental concept is that the detected ions and electrons must come from the same EC decay to give a meaningful time difference. This problem was solved by using coincidence techniques. The details of this technique will be discussed later. The Auger transition study in this work was carried out by using a double pass cylindrical mirror analyzer (CMA) to directly measure the emitted Auger electrons from the ^{37}Ar atoms absorbed on the back side of the substrates. The double Auger study also applied coincidence techniques to identify the correlation among the emitted Auger electrons. In the past three years, different ^{37}Ar sources, substrates, detectors and electronics have been used in this research work. The following sections will be devoted to describe in detail each part of the experimental setups.

The UHV System

The experiments were performed in an UHV system as shown in Fig. 3.1. The system was pumped mainly by an ion pump and a Ti-sublimator (TSP). A turbo-molecular pump was also provided to the system through a shut-off valve for baking and rare gases pumping. The typical base pressure of this system was about 5 x 10^{-11} Torr. The substrates in this experiment were mounted to a cold finger of a closed-cycle helium refrigerator. The two parts of the helium refrigerator were connected by a pair of helium transfer tubes. The device could deliver about 10 watts of cooling power to the cold finger at a temperature of 20 K. With proper shielding the substrates could reach as low as 16 K in this work. The temperature of the substrate was monitored by a thermocouple of Au/.07%Fe and chromel. This type of thermocouple has excellent sensitivity at low temperatures (17 μV/K at 10 K). During the experiment, the He refrigerator also served as a cold trap for

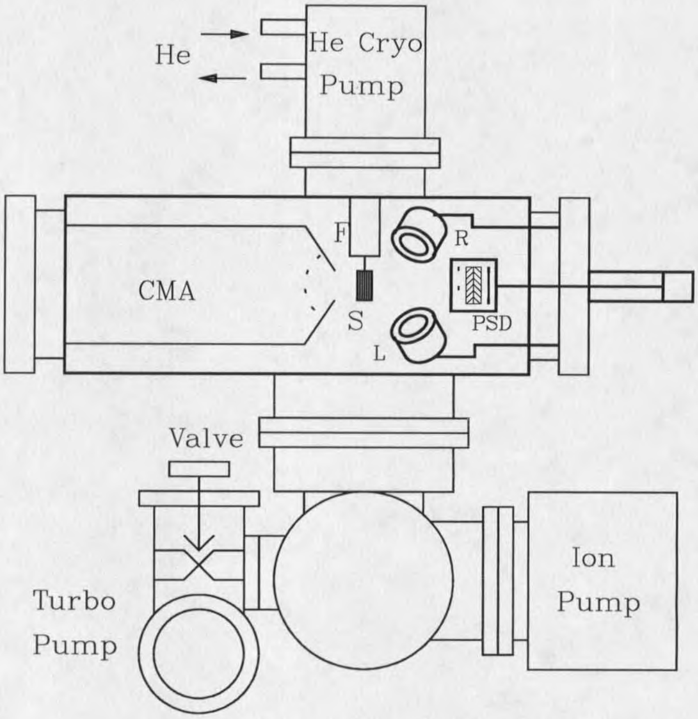

Figure 3.1 The UHV system of this work. F is the cold finger, S is the substrate and PSD, L and R are detectors.

the residual gases because the ion pump was turned off to prevent ions created inside the ion pump to affect the measurement. The working pressure in this circumstance was about 2 x 10^{-10} Torr. The refrigerator was mounted on a manipulator on the top of the chamber with x, y, z and tilt motions so that substrates could be brought to the focal point of the CMA or other selected points inside the system. In the early stage of the experiment, the CMA was also used to determine whether Ar was adsorbed on the substrates at certain temperature. At 16 K, the Ar Auger peak was clearly visible only when an Ar pressure of 10^{-7} Torr was maintained in the chamber during measurements in order to balance the electron-induced desorption (ESD) effect on the substrates. Figure 3.2 shows the adsorbed Ar and the substrate Auger peaks at different temperatures.

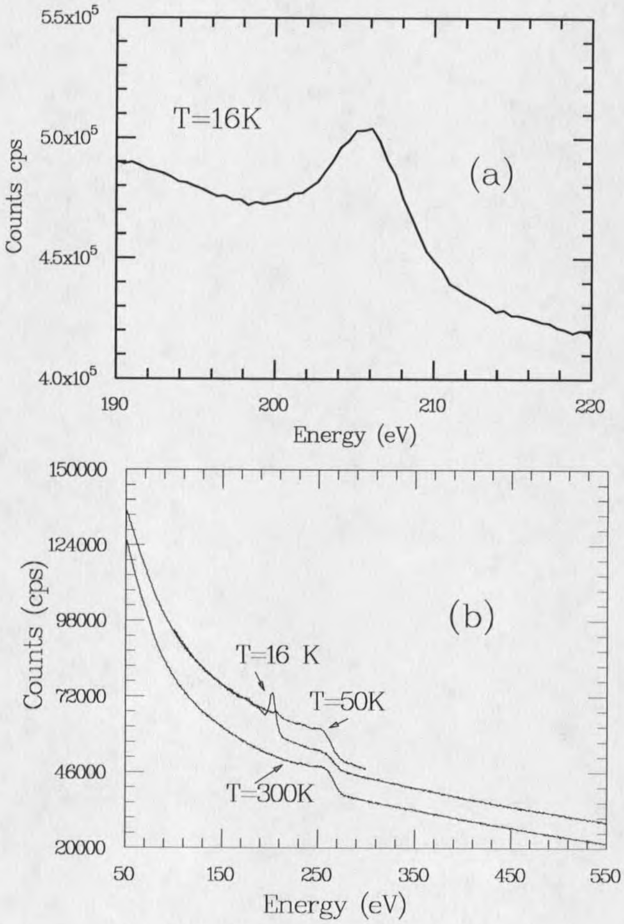

Figure 3.2 (a) Ar Auger peak from the Au/Si(111) substrate at 16K. (b) Ar and carbon Auger peaks from the pyrolytic graphite substrate at 16K, 50K and 300K.

The Substrates

There were two sets of substrates prepared in this experiment. The first substrate was a 1 x 1 cm^2 Si(111) wafer. Both polished sides of the wafer were coated with thick (0.2-0.3 μm) gold films in another vacuum chamber. Scanning electron microscope images showed a smooth film across the entire substrate with slight variations in topography visible only at the highest resolution of the microscope (~200Å). The last several layers of gold were evaporated on the substrate under *in situ* UHV conditions to ensure a clean surface. The CMA was used to monitor the substrate cleanliness. Auger spectroscopy showed no measurable contamination of the substrate surface at 16 K.

A major concern of the properties of the substrates was the back-scattering effect from the substrates. These back-scattered ^{37}Cl ions would have a different energy compared to those directly desorbed ions, and thus the recoil spectrum would be broadened. The back-scattering cross section is proportional to the square of atomic number, Z. Hence, the substrates had to use materials with low Z number.[26-28] One of the other considerations was that the substrate material had to be conductive so that it would not become charged when charged particles left the surface. Considering these conditions, carbon became a good candidate. Therefore, the second substrate was a high grade pyrolytic graphite (HPG) of 12 x 10 cm^2 area and 2 mm thick. The fresh cleaved HPG was examined by using a scanning tunneling microscope (STM) in the air, which revealed an atomically flat surface. The HPG was cleaved again from both sides right before being put inside the UHV chamber. Auger spectroscopy showed no measurable contamination of the substrate surface at 16 K (Fig 3.2 (b)). Argon physisorption and desorption were also monitored by a quadrapole mass spectrometer (QMS). It was found that Ar started to physisorb (multilayers most likely) at around 30 K and desorbed completely above 55 K on this substrate (Fig. 3.3).

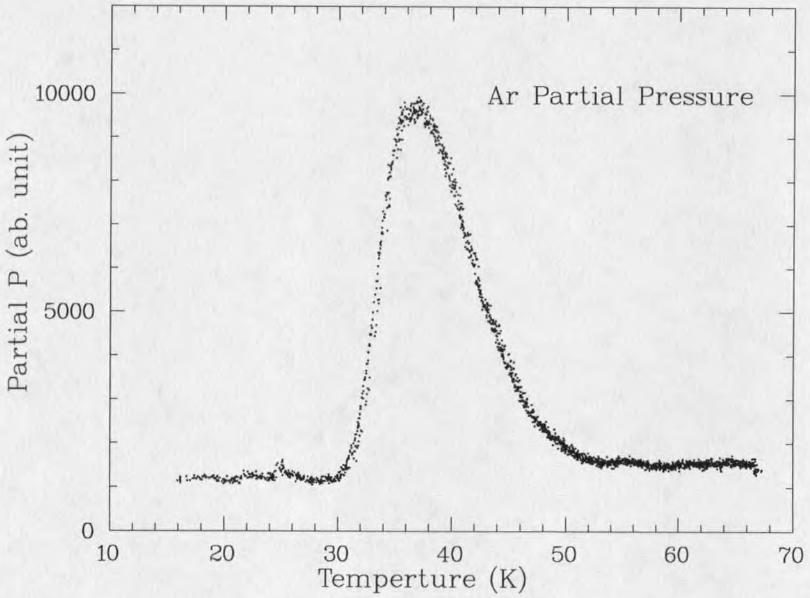

Figure 3.3 The temperature programmed desorption (TPD) spectrum of Ar from the HPG substrate.

Maintaining a good thermal contact between the substrate and the cold finger was very critical for obtaining the desired low temperature. Figure 3.4 shows the mounting bridge between the HPG and the cold finger. The bridge was machined with ultrahigh purity (99.999%) copper to increase the thermal conductivity at low temperature. (At

20K, copper with 99.999% purity is 10 times more thermally conductive than the one with 99.9% purity) The sapphire plates with high thermal conductivity and electrical resistance at 20 K served to isolate the substrate electrically

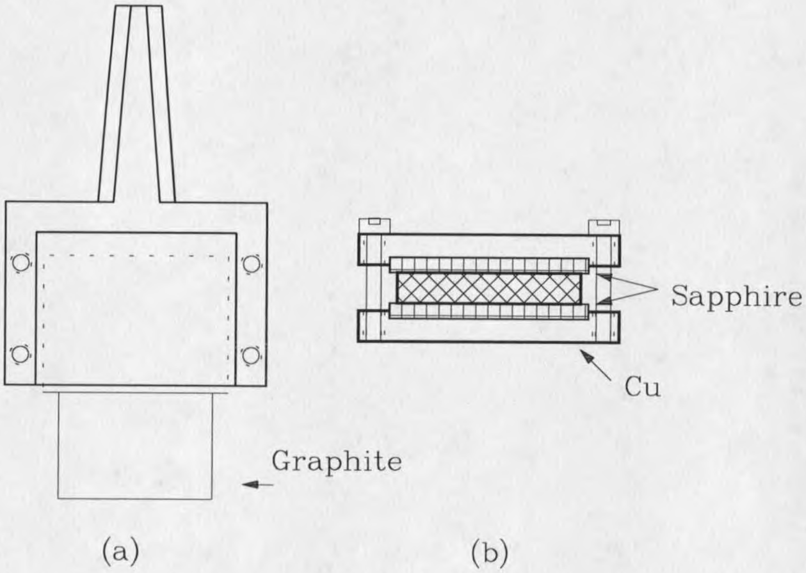

Figure 3.4 The mounting bridge between the graphite substrate and the cold finger. The sapphire plates can isolate the graphite substrate from ground. The bridge is soldered to the cold finger with indium.

The Detectors

Since the success of this work depends largely on the accuracy of coincidence time-of-flight measurements, several special requirements had to be met by the detectors which triggered the timing circuits. First, the detectors had to be able to output very sharp pulses. The time resolution of an electron-electron coincidence measurement must be better than a nanosecond. Therefore, the pulse output from the detector had to be in the order of nanosecond. Second, most of the measurements in this work required a large signal to noise ratio, so the detectors had to have very little background noise. A dark count rate in the range of a few counts per second was preferred. Third, the detectors had to be able to detect both electrons and positive ions by simply switching the electrical bias from outside the UHV chamber. Fourth, the detectors had to have stable gain over the time of experiment. Considering all the requirements above, channel electron multipliers (channeltron) and microchannel plates (MCP) made by Galileo Electro-Optics were adopted to develop the detectors.

There were three generations of detectors developed for this work. The first one used channeltron multipliers.[110] A channeltron is spiral glass tube two millimeters in diameter with materials with high secondary electron emission yield coated inside the tube. When a single electron strikes the tube entrance, several secondary electrons will be created. These electrons will then create even more electrons like an avalanche. A channeltron can detect both positive and negative charged particles by changing the bias voltage. Fig. 3.5 shows the schematic of the home made detector with the channeltron biased for electron detection. The channeltron was mounted inside a metallic cylinder by ceramic rods. Three screens were mounted in front of the channeltron entrance with the first and third screen grounded and the middle screen biased by screen voltage, V. The middle screen served to stop particles with energy lower than qV, where q is the charge of the particle. A positive voltage was used to retard positive ions and negative voltage to retard negative ions and electrons. By scanning the screen voltage, an integrated energy spectrum could be measured. The gain of this detector was about 10^7, the dark count was ~ 1 cps, and the full width at half-maximum (FWHM) of the output pulse was about 4 ns.

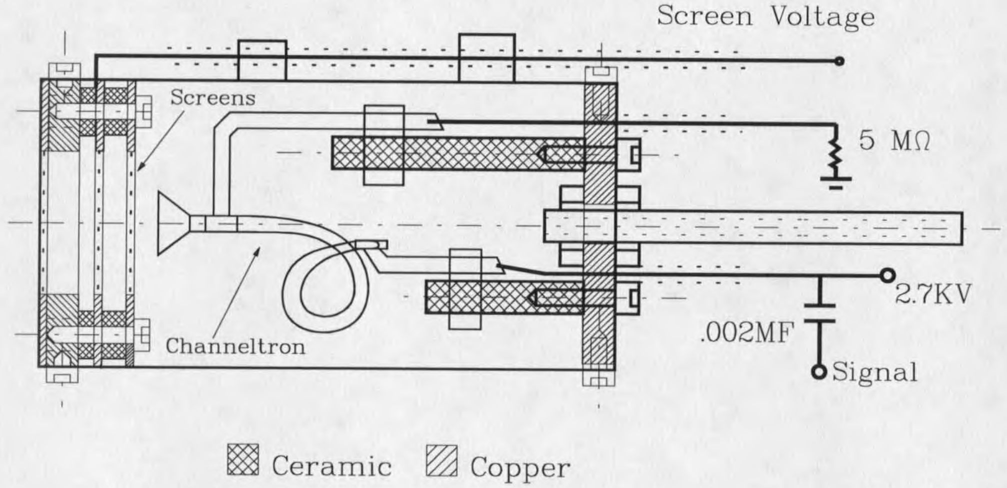

Figure 3.5 Detailed cross section diagram of the first home-made detector with channeltron multiplier. Detector is biased for electron detection.

There were some disadvantages for the first generation detectors with channeltron multipliers. As shown in Fig. 3.5, the front entrance of the channeltron was a cone shape. When electrons or ions reached different parts inside the front cone surface, they could have different flight distances. This would bring errors in the time-of-flight measurements. The four-nanosecond FWHM pulse width was also not satisfactory for accurate time measurements. Therefore, the next generation detectors employed microchannel plates (MCP)[111] to substitute channeltron multipliers. A MCP is an array of about 10^6 miniature electron multipliers. Each one of them works like a tiny channeltron. Typical channel diameters are in the range of 10-100 μm and the length to diameter ratios are between 40 and 100. Parallel electrical contacts to each channel are provided by the deposition of metallic coatings on the front and rear surfaces of MCP, which then serve as input and output electrodes. The total resistance between electrodes is about 10^9 Ω. Such MCP, used singly or two of them in a cascade, allow electron multiplication factor of 10^4-10^7 coupled with ultrahigh time resolution (<1 ns). The spatial resolution of the MCP is limited only by the channel dimensions and spacing. The channel diameter of the MCP used in this work is 12 μm and the center-to-center spacing is 15 μm. The MCPs have direct sensitivity to charged particles like electrons and ions (Fig 3.7 (a)), and energetic photons like x-rays and UV light. Therefore, they have been widely used in imaging, surface science and nuclear physics.[111]

Each of the new detectors used two MCPs in cascade. Each MCP was one inch in diameter and 400 μm thick. The mounting assemblies and electrode connections for the MCP's were home-constructed as shown schematically in Fig. 3.6. Each detector had three screens in front of the MCPs with the middle screen serving as a retarding screen. These detectors produced stable and reliable noise-free sharp negative pulses at an average height of 50 mV and with FWHM less than 1 ns. The dark count rate was about 2-3 cps. A pulse height spectrum of each MCP was measured in order to set the trigger thresholds in the amplifiers above electronic noise (Fig.3.7(b)).

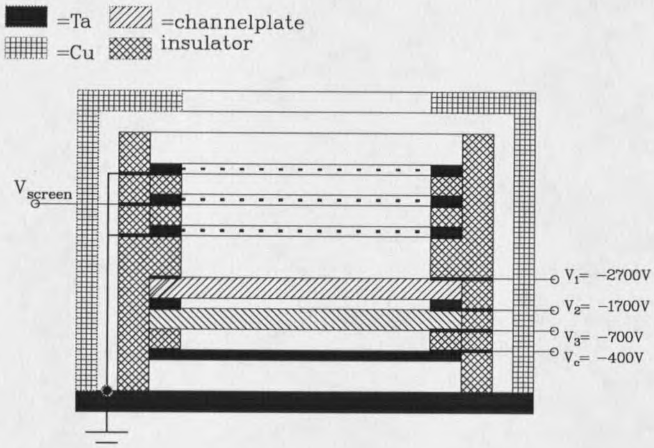

Figure 3.6 Cross section diagram of MCP based detector. Detector is biased for positive ion detection.

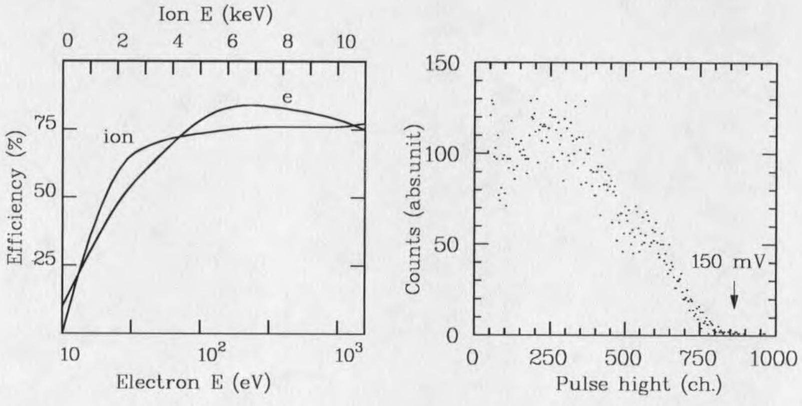

(a)
(b)

Figure 3.7 (a) Electron and ion detection efficiency of MCP. (b) A typical pulse high distribution spectrum of the MCP used in this work.

In the ion counting mode, a negative high voltage of -2.7 kV was applied between the front MCP and the ground to prevent KLL Auger electrons (E<2.6 keV) from entering the detector and contributing to the positive ion signal. This voltage also accelerated the positive ions to an energy at which their detection efficiency was maximized (Fig. 37(a)). In this case, a -2.0 kV voltage was maintained between the front and rear of the MCPs which made the voltage across each MCP to be 1.0 kV.

The Position Sensitive Detector

Sometimes it is necessary to acquire spatial information of the detected particles. For example, the flight distances between sample and MCP detector were different for electrons or ions arriving at different points on the front MCP. Compensation could be made for the flight path if one could know the exact location where the particle had landed. In the past ten years a variety of imaging multichannel detectors have been developed.[112-120] The tremendous parallel collection advantage inherent in these devices can also be used to greatly reduce data-acquisition times and increase detection sensitivities. In this work, a microchannel plate with resistive anode encoder (MCP-RAE)[112-118] two-dimensional detector was developed.

Instead of a conductive plate behind the rear MCP to collect the multiplied electrons and output pulse signal, the MCP-RAE detector uses a plate with evenly coated resistive film which outputs signals encoded according to the location where electron hits the front MCP. The theoretical formulation of the encoding mechanism is briefly described here.[112] Considering a planar resistor whose surface resistivity is denoted r and whose electrostatic capacitance per unit area is denoted c, if the potential at a position (x,y) is V and the vector surface current density is $\boldsymbol{S}$, then Ohm's law and the law of charge conservation require

$$r\boldsymbol{S} + \nabla V = 0 \qquad (3.1)$$

and

$$\nabla \cdot \boldsymbol{S} + c\,V = J \qquad (3.2)$$

where J is the incident source of current driving the anode. Combining Eq. (3.1) and Eq. (3.2), the two-dimensional time-dependent diffusion equation becomes

$$\nabla^2 V - rcV = -rJ \qquad (3.3)$$

This equation is subject to suitable boundary conditions defined by the edges of the anode. An appropriate model for the driving signal J is a delta function in space and time

$$J(x,y,t) = Q\,\delta(t)\,\delta(x - x_0)\,\delta(y - y_0) \qquad (3.4)$$

with Q is the total charge delivered by the event and (x_0,y_0) is the event location on the anode. An important special case of Eq. (3.3) is the situation where the total terminal charge signals are of interest but the detailed diffusion pulse shapes are not. For this case, the dc (time average) part of Eq. (3.3) and Eq. (3.4) can change to a Poisson equation

$$\nabla^2 V = -rJ \qquad (3.5)$$

where J is now the function of location (x,y) only. Equation (3.5) is not analytically solvable for arbitrary boundary conditions. It has, however, been solved for several special cases of interest for position sensing with solid state detectors, gas counters and

MCP's[112]. The simplest case is when the resistive surface is infinite in extent. In this case, the current, I extracted at a point l distance away from the source will be inversely proportional to l.

$$I \propto 1/l \tag{3.6}$$

This means that far away from the source, the signal output will be lower. Therefore, in principle the distance could be obtained by knowing the relative magnitude of the signal.

One practical solution to the boundary problem of Eq. (3.5) leads to the development of the MCP-RAE. In 1972 Augustyniak[121] *et. al.* reported their design which involved terminating the edges of a uniform resistive surface with resistivity, r by four concave circular arcs having radius of curvature, a and resistance per unit length, R_L, as shown in Fig. 3.8. The relation is

$$R_L = r/a \tag{3.7}$$

By using this design, which followed the suggestion by the Gear theorem, the anode could be operated in a distortionless manner. The Gear theorem states that a uniform current flow in an infinite sheet having a resistivity r is unaffected by a circular hole of radius, a if the hole is bordered by a line resistor of value $R_L = r/a$. This theorem holds for any arrangements of the holes. One of such arrangement is just the design by Augustyniak as shown in Fig. 3.8. In this design the four corners of the plate would share the incident charge Q in the way as if the plate is infinite in extent, *i.e.*, the currents, I_a at the four corners would be inversely proportional to the distance between the event point (x,y) and the corner vertices. Therefore the event position (x,y) can be obtained as

$$x = d\,\frac{I_1 + I_4}{I_1 + I_2 + I_3 + I_4}, \quad y = d\,\frac{I_1 + I_2}{I_1 + I_2 + I_3 + I_4} \tag{3.8}$$

where d is the length of the side of the anode and the coordinates are shown in Fig. 3.8.

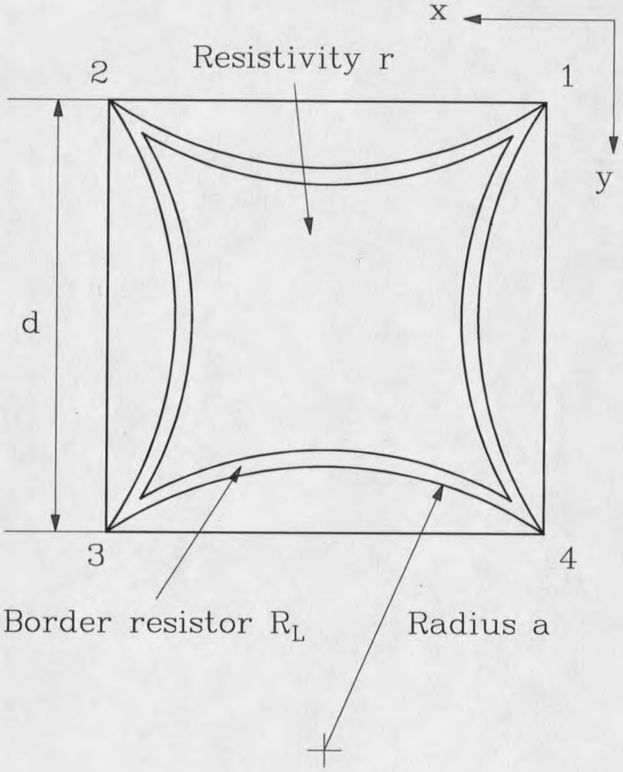

Figure 3.8 Geometry of a circular arc terminated resistive anode encoder. Electrical connections are made at the four corners.

In this work, a 100kΩ resistive anode encoder (RAE) with 1x1 inch size made by Quanta Inc. was used. Figure 3.9 shows a diagram of this home-constructed MCP-RAE detector with biased voltages for ion detection. The detailed design diagrams of each part are provided in Appendix B. This MCP-RAE detector provided very high dynamic gain

(10^7), very low background noise (1 cps) and superb time and spatial resolutions. The time resolution of a detector is mainly determined by its output pulse width. Because the signals from the four corners in this detector were of the order of 100ns, a special arrangement was made to extract the timing pulse from the rear side of the second MCP. In this way, a sub-nanosecond time resolution was achieved. The spatial resolution was checked by putting a mask with tiny holes in front of the detector and looking for the output image of these holes. The diameter of these mask holes was 0.2 mm. The resulting images of these holes had a FWHM of less than 0.2 mm diameter, indicating that the spatial resolution of this detector was better than 1/100, the specification of an MCP-RAE detector commercially made by Quanta Inc.. The success of the whole operation relied largely on the performance of this detector.

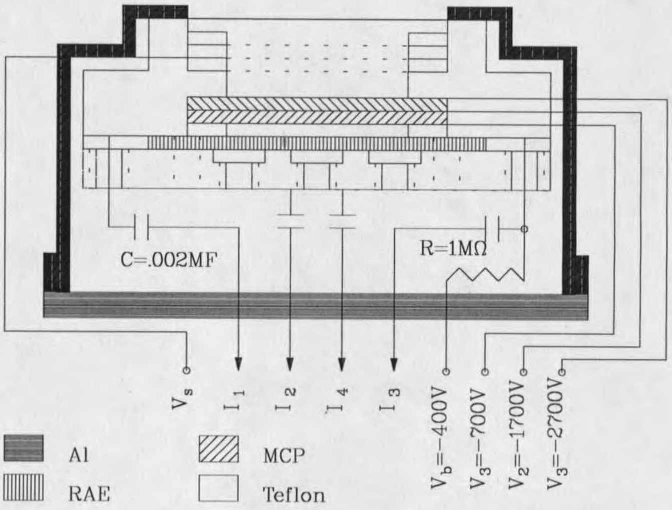

Figure 3.9 Cross section diagram of the home-constructed MCP-RAE detector. Biased for positive ion detection.

The Radioactive ^{37}Ar Sources

With a half life of 35 days, the ^{37}Ar cannot survive in nature. Argon has an atomic number of eighteen and is located between Cl and K in the periodic table. There are eleven isotopes ranging from ^{34}Ar to ^{44}Ar. The stable isotopes of Ar include ^{36}Ar (0.337%), ^{38}Ar (0.063%) and ^{40}Ar (99.6%). All the unstable isotopes with atomic weight lighter than A = 38 decay through electron capture and those heavier than A = 38 decay by beta decay.[24] Therefore, the isotope ^{37}Ar needed in this experiment had to be prepared by designated nuclear reactions. There are several ways to produce ^{37}Ar from its stable isotope or neighboring elements. The difficulties involve obtaining enough reaction cross section so that the concentration of the produced ^{37}Ar is large enough and the safety concern on how to handle these radioactive materials. For this experiment, ^{37}Ar was produced by either ^{36}Ar(n,γ)^{37}Ar or ^{40}Ca(n,α)^{37}Ar reactions[122] in the Brookhaven National Laboratory and extracted locally as described below.

The first ^{37}Ar source prepared for this work was produced from the stable isotope ^{36}Ar through the nuclear reaction ^{36}Ar + n $\rightarrow$ ^{37}Ar + γ involving high energy neutrons in the center of a nuclear reactor.[122] A quartz ampoule filled with 10 ml of ^{36}Ar enriched to 99.5 atom% was purchased from Isotech Inc.. The neutron capture cross section for this reaction is 5 barn;[8] irradiation with a flux of 10^{14} n/cm^2-s for seven days would produce 7 x 10^{16} atoms of ^{37}Ar corresponding to 0.03% concentration in the remaining ^{36}Ar atoms. There were about four weeks waiting time for the short-lived radioactivity produced in the irradiation to die down to an acceptable level for handling. Therefore, the final source used in the experiment would have 4 x 10^{16} atoms of ^{37}Ar corresponding to an activity of 250 mCi and a 0.015% fraction of the ^{36}Ar gas. Since the density of $^{36/37}$Ar atoms on the surface is 7 x 10^{14}/cm^2 for a monolayer, the initial number of ^{37}Ar atoms on the surface would be 1 x 10^{11} atoms for a monolayer on the 1 cm^2 substrate surface, corresponding to an initial decay rate of 2.3 x 10^4/s.

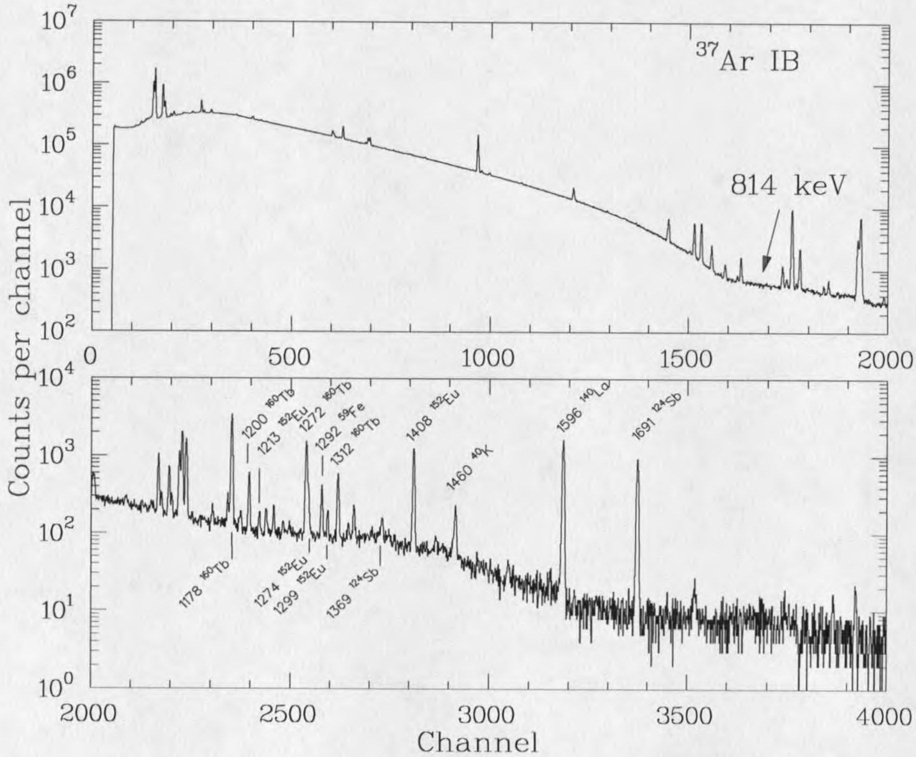

Figure 3.10 The gamma ray spectrum of the radioactive gas source taken by an HP-Ge detector. The dominant feature is the ^{37}Ar IB radiation and the background activity mostly comes from the quartz ampoule materials excited by the neutron bombardment.

The irradiated ampoule was transported from the reactor to the laboratory in a heavily lead-shielded container. After the initial check by the nuclear security officer, a gamma ray spectrum was taken by an HPGe-detector which revealed the characteristic ^{37}Ar internal bremsstrahlung (IB) and other radioactive background as labeled in Fig. 3.10. This assured that the ^{37}Ar was indeed produced by the bombardment of the fast neutrons in the center of the nuclear reactor. The ampoule was then introduced into another vacuum chamber which was baked at 150° C for 12 hours and then pumped down to 10^{-8} Torr. The ampoule was then broken mechanically with a piston attached to a linear feed-through. A gamma ray spectrum was taken again just outside the source chamber

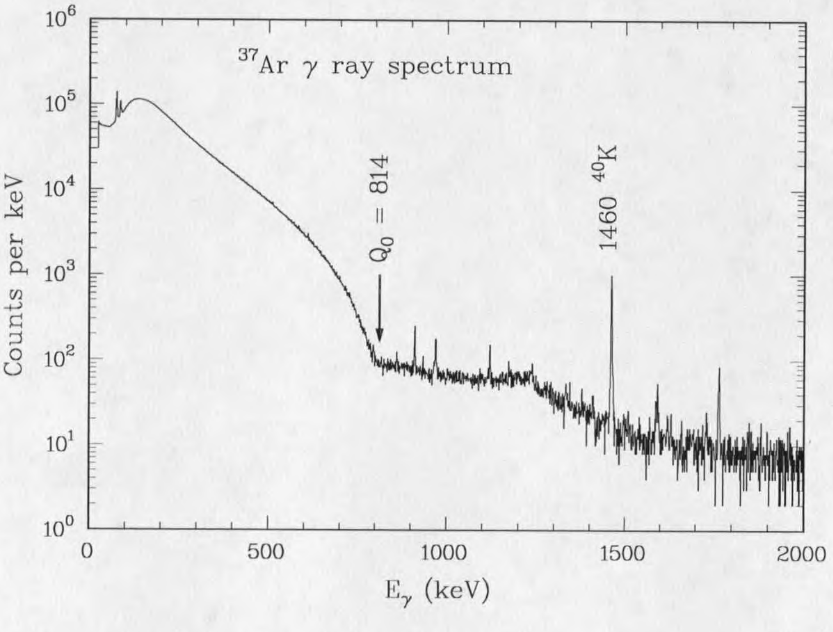

Figure 3.11. The gamma ray spectrum of the ^{37}Ar gas source after the ampoule was broken. Noted that most of background radioactivity was blocked and the ^{37}Ar IB radiation dominated the spectrum.

which confirmed the purity and strength of the radioactive gas. The dominant feature of the spectrum was the continuous internal bremsstrahlung radiation which had an end-point energy at 814 keV (the Q value of ^{37}Ar decay).[8] Otherwise, the most prominent feature was the 1460-keV ^{40}K line due to the room background (Fig. 3.11).[8] The gas was leaked into the main chamber via a Varian leak valve which had an excellent dosage control. There was a second leak valve for research grade Ar gas (^{40}Ar) which was also used in some parts of the experiment.

The recipe described above could produce only a very small fraction of ^{37}Ar among the huge background of ^{36}Ar. The low concentration of ^{37}Ar demanded a higher total dosage in the experiment to get the required activity. As discussed in the first chapter, this means each ^{37}Cl atom would have more surrounding ^{36}Ar atoms, hence more chances to exchange charges. To get a higher concentration of radioactivity, the second ^{37}Ar source was prepared by a different way. The isotope ^{40}Ca was used to produce ^{37}Ar by the ^{40}Ca (n,α)^{37}Ar reaction. Half of a gram high-purity ^{40}Ca isotope was bombarded by fast neutrons for three days near the center of the nuclear reactor. The nuclear reaction ^{40}Ca + n $\rightarrow$ ^{37}Ar + ^{4}He (α) took place and ^{37}Ar and ^{4}He gases were created inside the ^{40}Ca solid. The cross section of this reaction is about 0.5 barns and the total yield of ^{37}Ar was about 20 mCi. Without the background of ^{36}Ar, the impurities now were mainly the residual gas inside the source chamber. By this method a tenfold more concentrated ^{37}Ar source was produced.

The procedure of handling of the radioactive source was similar to the previous one except the solid ^{40}Ca sample had to be melted in order to extract the ^{37}Ar trapped inside. It was found that the ^{40}Ca would react with the quartz ampoule when heated above the melting point of Ca at 840 °C. To solve this problem, the ^{40}Ca sample was doubly vacuum sealed under 10^{-8} Torr pressure before the irradiation (Fig. 3.12). After the irradiation, the ampoule was heated up to 950^{0}C in air for five minutes. This would completely melt the Ca solid and release the trapped ^{37}Ar gas. The inner sealed ampoule was broken during the heating because of the chemical reaction between Ca and quartz (SiO_2) but the outer ampoule would hold until being broken mechanically inside the source chamber. The gas obtained this way was ten times more concentrated than before, but the residual gas which made up for the impurity background was still too high. A

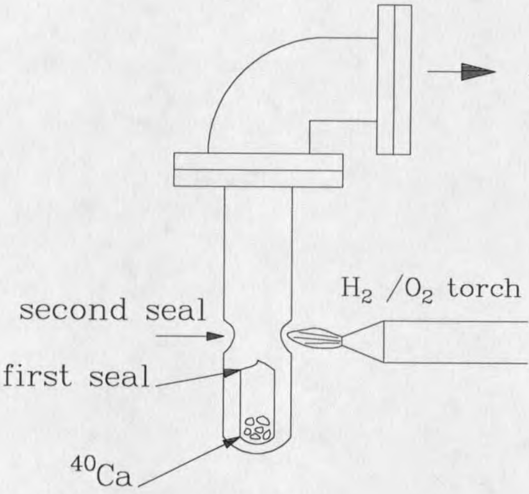

Figure 3.12 Double sealing ^{40}Ca within quartz ampoules under high vacuum.

getter pump which is inactive with Ar but highly reactive with other residual gas will be required to purify the gas source in future experiments.

Coincidence Techniques and Electronic Systems

In many physical studies the interesting physical events may be submerged in a large background of other events which share the same physical characteristics, such as energy, momentum, mass, etc., and the only trace of the events of interest is their characteristic time sequence. Utilizing this intrinsic time correlation, coincidence technique identifies physical events which happen as the result of the same physical process. This technique has been widely used in nuclear physics and some studies in surface and atomic physics.[105-109] In this research work, coincidence techniques were applied together with other surface analysis techniques to study the desorption of ^{37}Cl ions and the Auger relaxation.

A typical coincidence measurement setup was employed in the early phase of the experiment. The design of the setup is shown in Fig. 3.13. It consists of two MCP detectors with retarding screens, two time filter amplifiers (TFA), two constant fraction discriminators (CFD), a time-to-amplitude converter (TAC) and a multichannel analyzer (MCA) driven by a personal computer. One primary object of this system was to determine whether the signal detected by the second detector was a true coincidence with the one detected by the first detector, *i.e.,* did the two signals arrive at the two detectors close enough in time to have originated from the same physical process? The two output signals from different MCP detectors were amplified, shaped, and fed into the TAC with one of them starting and the other stopping the timing circuits. The TAC then output a pulse whose height was proportional to the difference of the arrival times of the two input pulses. A computer driven MCA would then record the histogram of the TAC pulses.

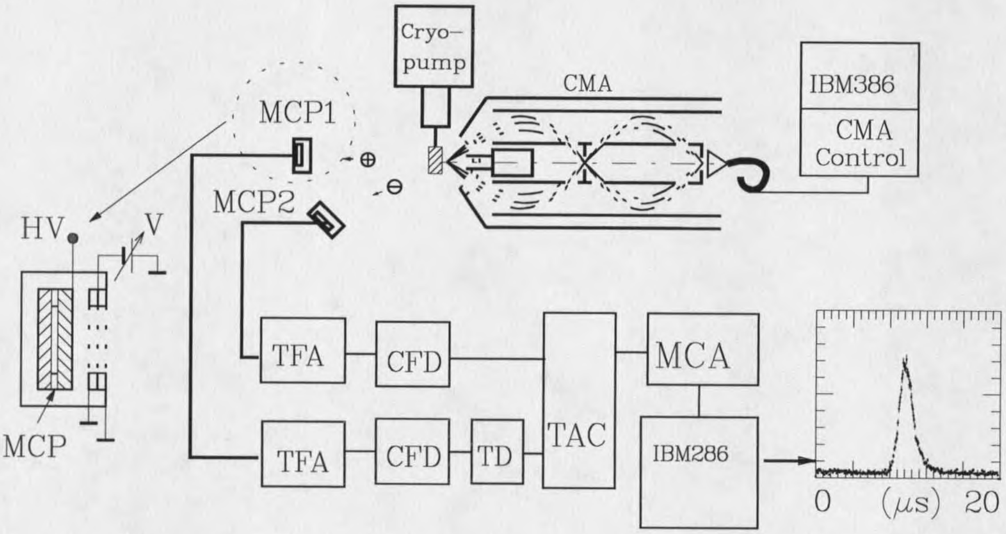

MCP: Microchannelplate
TFA: Timing Filter Amplifier
CFD: Constant Fraction Discriminator
TAC: Time-to-Amplitude Convertor
MCA: Multichannel Analyzer
TD: Time Delay
CMA: Cylindrical Mirror Analyzer
V: Retarding Screen Voltage

Figure 3.13 The schematic diagram of the first coincidence measurement system.

A time coincidence of two signals from the same physical process is called a *true* or *real* coincidence. It is also possible for signals from different processes to trigger the timing circuits, this would produce an unwanted *chance* or *accidental* coincidence.[122] In principle, discriminating between true and accidental coincidences is relatively easy. After accepting the first signal to start the timing circuit in TAC, only a short period of time (time range of TAC) is waited for the second signal to arrive to trigger the stop. The longer the waiting period, the greater the possibility of having an accidental count. The pulse height spectrum of TAC in the MCA provides a trivial mean to distinguish between true and accidental coincidences. The pulse heights, and thus the time differences corresponding to the starting and stopping signals of true coincidences have a finite fixed time relationship. Accidental coincidences, however, representing random signals, have no definite time relationship. Therefore, accidental coincidences produce a uniform range of pulse heights whereas true coincidence produced a signal unique pulse, *i.e.,* a peak as shown in Fig. 3.14.

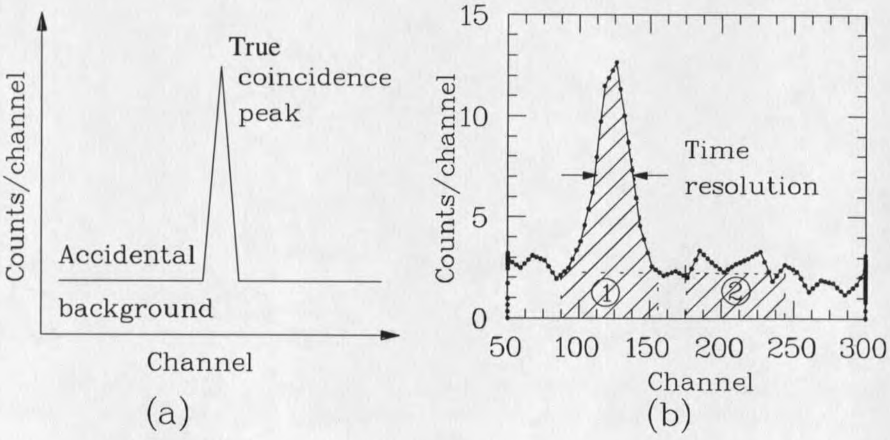

(a) (b)

Figure 3.14 Coincidence peak from (a) ideal detectors and (b) real detectors (Si Auger electrons and primary excitation electrons). The area in region 1 gives true + accidental coincidences; region 2 gives accidental coincidence, and their difference gives the true coincidence.

The electronics of this system is also shown in Fig. 3.13. The two MCP detectors were biased with the center one for positive ion detection and the side one for electron detection in the ^{37}Cl ion recoil velocity measurements. Electrons with different energies could also be selected by the retarding screens. The TFA (model 474, Ortec) supplied variable gains and time integration constants to match the output pulses of the MCP detectors. The CFD (model 584, Ortec) transferred the amplified signals from the TFA into sharp negative pulses of 500 ps FWHM for better time resolution. The TAC (model 2143, Canberra) had a time range from 20 ns to 1 ms. The MCA (Ortec 4000) had 4092 channels for histograming. Since the electrons are much faster than the ions (typically 10^4 times faster), the time difference obtained from the coincidence peak in the histogram was effectively the time-of-flight of the ^{37}Cl ions. The velocity could then be obtained by either knowing exactly the distance between the sample and the center detector or by shifting the center detector a known distance and measuring the shift of the coincidence peak. The integrated recoil energy spectra of the ^{37}Cl ions were also directly measured with the center MCP detector alone by scanning the retarding screen voltage. The ^{37}Cl Auger energies were directly measured by the CMA facing the other side of the sample. The coincidence measurements and the MCP or CMA scanning were both controlled by a personal computer with home-made interface and programs.

A much more sophisticated system for coincidence measurement, equipment control and data acquisition was developed in the later phase of the experiment. Three MCP detectors with one of them position sensitive (MCP-RAE) were used in the new system. The entire chain signal amplifying, shaping, logic operating, timing and recording processes were conducted on a NIM bin and a CAMAC crate which could interface directly with a personal computer at very high speed. The experimental data could be stored in an event-by-event basis on a 2.3 GB magnetic tape with all the timing and spatial information in a pre-selected manner. After the experiment, the actual physical processes could be revisited by simply replaying the tapes. The schematic diagram and the logic block diagram of this system are shown in Fig. 3.15 and Fig. 3.16, respectively.

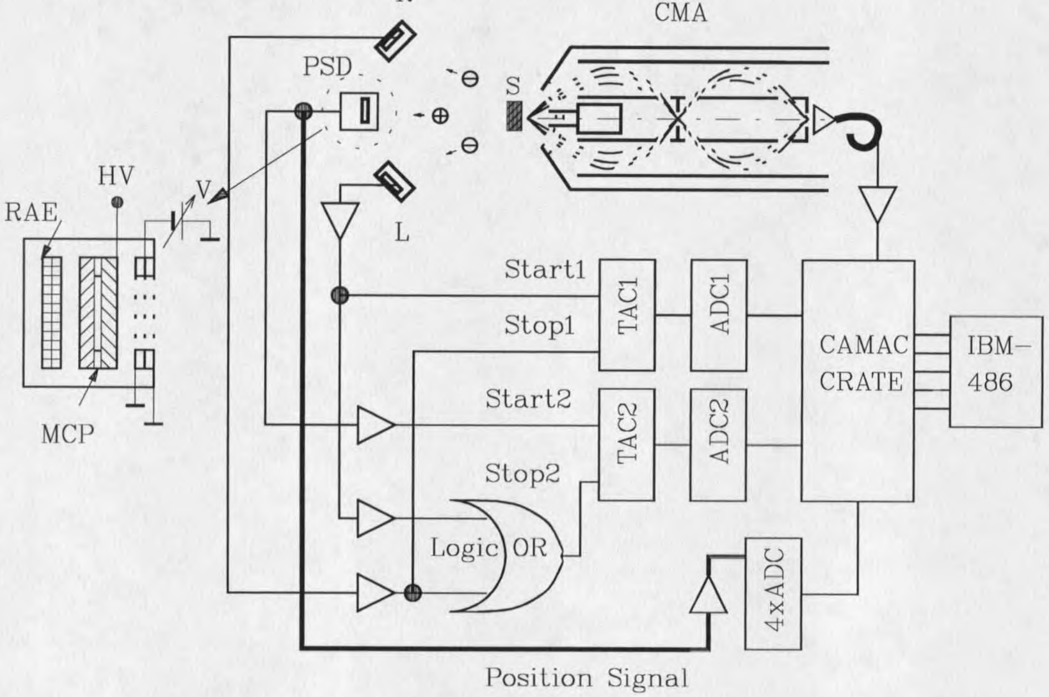

Figure 3.15 The schematic diagram of the second coincidence measurement system.

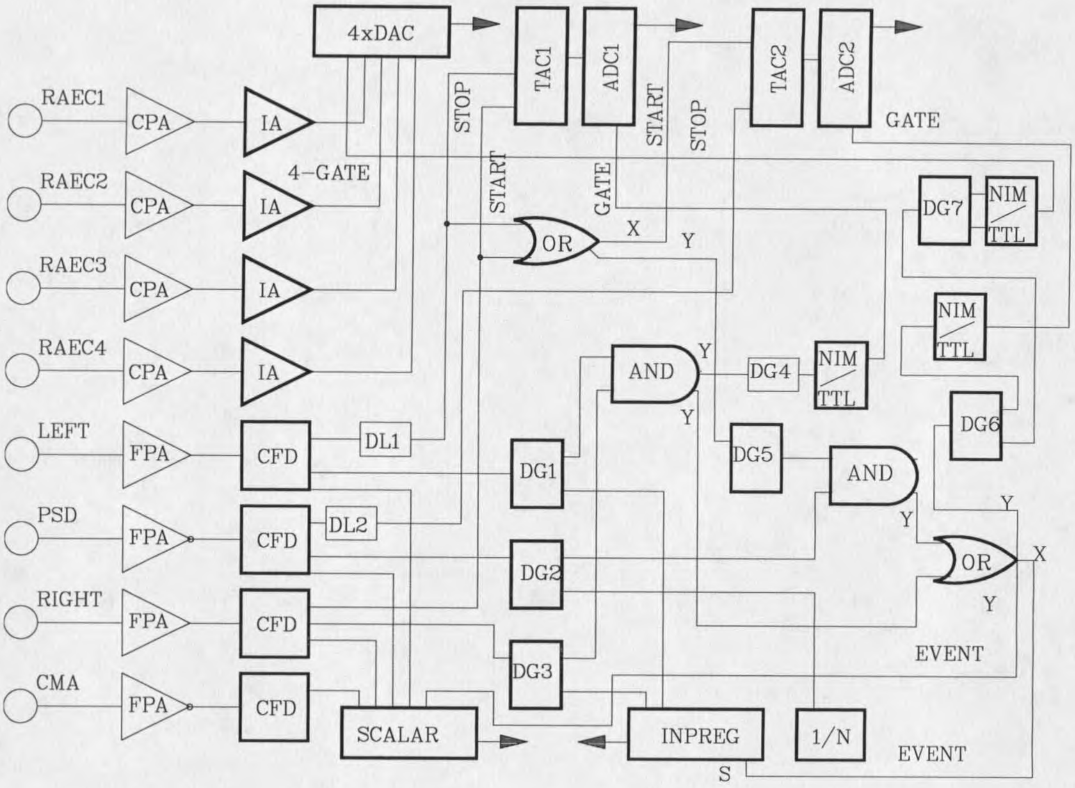

Figure 3.16 The logic block diagram of the second coincidence measurement system. Some of the symbols are explained in the text.

The detailed descriptions of each component are omitted here and only the operation concepts will be discussed. Each block in Fig. 3.15 and Fig. 3.16 was mounted either on a CAMAC crate or on a NIM bin. Three timing signals came from the left MCP detector (L), the right MCP detector (R) and the middle MCP-RAE position sensitive detector (PSD). Each signal was amplified and shaped by a fast timing amplifier (FTA) and a constant fraction discriminator (CFD). The outputs of these CFDs would be properly delayed and gated by the delay and gate generators (DG) before fed to the time-amplitude-converters (TAC) to generate coincidence spectra. Coincidences between L and R were registered at TAC1 and ADC1. Coincidences between either L and PSD or R and PSD were registered at TAC2 and ADC2. The ADC1 and ADC2 are the analog-to-digital converters for the first and second TACs, respectively. The PSD also sent out four position signals which were amplified by the charge pre-amplifiers (CPA) and linear amplifiers (LA) before reaching the ADC-quadruplets (4xADC). The digitized position signals from the 4xADC were then compared by the personal computer to calculate the positions of the detected particles.

Each of the CAMAC crate based devices needs a timing gate, a NIM or TTL logic pulse with right time sequence and duration to synchronize the operations. A timing gate of a device provides the exact time window within which certain operation will be executed. These timing gates were generated by the timing signals through the logic operating device (logic *AND*, logic *OR*, etc.) and the DGs. For example, the timing gate of the TAC1 coincidence registration was generated by the logic *AND* of L and R signals, *i.e.*, both L and R signals had to be present within the duration of the timing gate to trigger the recording of an event in TAC1. The timing gate of TAC2 was generated by the logic *AND* of the PSD signals and the results of the logic *OR* of L and R signals, *i.e.*, either L and PSD or R and PSD signals had to be present to trigger the recording of an event in TAC2. The identification between the two kinds of coincidence events in TAC2 was achieved by the input register (INP.REG) which would record whether PSD was in coincidence with L or R. The position information register 4xADC and the single rate counter SCALAR were gated by the *event gate.* The event gate was generated by the logic *OR* of the TAC1 timing gate and the TAC2 timing gate. Therefore, the position signals and the single counts were saved on the tapes through the personal computer whenever an event was registered in either TAC1 or TAC2. If a higher sampling rate was desired, the event gate could also be created by adding (logic *OR*) every Nth of the PSD single counts to the original event gate. This would save the position signals and the single counts either on each coincidence count or on each Nth PSD count.

In the block diagram shown in Fig. 3.16, the timing gate of TAC2 was actually the event gate. This means the TAC2 would register an event whenever TAC1 or TAC2 was triggered. This would provide a mean of examining a three-event coincidence, *i.e.,* L, R and PSD detectors receiving signals simultaneously. The registered data on TAC1/ADC1, TAC2/ADC2, 4xADC, SCALAR and other related parameters could be written to a magnetic tape as a *word* in an event-by-event manner. By replaying the tape, these words would be retrieved by the computer in their actual time sequence. The interface between computer and the CAMAC crate was controlled by the program developed by Dr. Hindi.

Experimental Procedure

Before any actual measurement, considerable efforts had been made to fine-tune the electronic system. The gain of each amplifier was carefully adjusted to meet the requirements of time and spatial measurements. The pulse shapes were examined at each of the amplifiers with an oscilloscope to ensure the right amplitudes and widths. Each timing gate was logically planned and generated in the right time sequence and for the right time duration. Several combinations of the amplifiers were tested and the best choice for each measurement was decided. Software was debugged and some applications were programmed on the spot. It took at least a month before each round of measurement to prepare the electronic system and the radioactive gas source.

The typical experimental procedure involved cooling the substrate from room temperature to 16K in about 3 hours, and dosing the sample with radioactive ^{37}Ar. For the ^{37}Cl ion recoil time-of-flight measurements, the dosage was usually about 1 L (1 L $=10^{-6}$ Torr x 1 s = 5 x10^{-9} Torr x 200 s) of $^{37/36}$Ar gases or ^{37}Ar made from ^{40}Ca(n,α)^{37}Ar mixed with the residual gases in the source chamber. The sticking coefficient of Ar at 16 K is nearly unity; hence 1 L dosage would produce a monolayer (1 ML) coverage (the actual coverage might be a little high because the local partial pressure near the dosing nozzle could be higher than the ion gauge reading). Two independent measurements were conducted simultaneously: The CMA was used to measure the kinetic energy distribution of the Auger electrons emitted following the EC decay of ^{37}Ar, and the MCP's were used to measure the time-of-flight of the desorbing ions by recording the coincidences between the ^{37}Cl ions and the Auger electrons following the EC decay of ^{37}Ar. The counting electronics for this measurement is shown in Fig 3.13 and Fig 3.16. The ion detector was biased -2700 V at the front side of the first MCP to prevent fast Auger (KLL) electrons from entering. The electron detector had a screen voltage, V_S = -50V to measure both

KLL and LMM Auger electrons, or V_S = -250 V to measure only KLL Auger electrons. For the recoil energy (near 9.5 eV) and the flight distance (4-6 cm) of interest in this measurement, the time-of-fight of the ^{37}Cl ions was about 10 μs. Therefore, the time range of the TAC was set at 20 μs full scale to balance the time resolution and accidental rate. Because of the low counting rate, all other sources that could contribute to ion or electron counts were shut off during the measurement. The ion pump, ion gauge and electron gun were turned off and even the view ports were covered to prevent room light from getting into the MCPs. The system was maintained under UHV conditions (2 x 10^{-10} Torr) by the He cryopump that also cooled the sample. A fresh layer of Ar gas was adsorbed every 8 hours for measurements with 1 L coverage.

For some surface interaction studies multiple layers of Ar gas were adsorbed. The energy and charge distributions of ^{37}Cl ions at various coverage were measured directly by scanning the retarding screen voltage of the ion MCP detector from 0 to +20 V. The time-of-flight of ^{37}Cl ions was measured by coincidence techniques for different coverage. The same measurements were also conducted for the ^{40}Ar and $^{36/37}$Ar mixture.

In the ^{37}Cl double Auger study, 6 to 10 L of ^{37}Ar source was dosed every 20 hours. The MCP detectors were all biased for electron detection. In the EC decay, a KLL Auger electron will always be followed by the LMM Auger cascade electrons. Coincidence is expected for two detectors receiving KLL and LLM Auger electrons. However, if one biases both detectors with screen voltage of -250V, there should be no

LMM Auger electrons detected. In this case, the two MCP detectors should not yield any true coincidence counts unless there is double Auger decay with both of the electrons emitted having kinetic energy higher than 250 eV. The probability of the double Auger process and the energy distribution of these double Auger electrons were measured using coincidence techniques. The correlation between the KLL Auger electrons and each LLM and LMM Auger peaks were also examined by using coincidence techniques. By measuring two sets of coincidence simultaneously and recording them in the real time sequence, the triple coincidence, *i.e.,* all three detectors receiving signals at the same time, could then be examined by replaying the recording tape.

Most of the above measurements were repeated by using different substrates and different Ar sources. The results reported here for the ^{37}Cl ion time-of-flight and surface interaction studies were mostly obtained from the experiments using the first radioactive gas source and the first experimental setups. The results of ^{37}Cl Auger relaxation studies were obtained from the experiments using both radioactive gas sources and both experimental setups. A triple-event coincidence measurement was attempted in the last experiment to study the double Auger decay.

CHAPTER 4

RESULTS AND DISCUSSIONS

Desorption due to Recoil Induced by Neutrino Emission

Energy Distribution of ^{37}Cl Ions

In this section the energy distribution of the ^{37}Cl ions desorbed due to recoil induced by neutrino emission will be presented. In order to gain a better understanding of the experimental results, one should first have some idea about what to expect from these measurements if the ^{37}Cl ions had no interaction with its surroundings. Ideally, without interaction or a massive neutrino, the recoil energy of the ^{37}Cl ions should be well defined (9.54 eV) as calculated in Chapter 2. In reality, there are many factors which might contribute to the broadening of the energy spectrum even without the substrate surface interactions. These "intrinsic factors" which affect the energy spectrum of the isolate atoms will be discussed first.

As discussed in the Chapter 2, an isolated ^{37}Ar atom decays 90% of the time by electron capture from the K-shell (the K-shell binding energy of the daughter atom ^{37}Cl is

2.822 keV), otherwise mainly from the L_1-shell (270 eV). This leads the isolated daughter ^{37}Cl atom (assumed to be initially at rest) to recoil with a kinetic energy of 9.54 eV if the neutrino accompanying the decay is massless. This energy will be reduced by $m_\nu^2/2M$ if a neutrino with mass m_ν is emitted, where M is the mass of the ^{37}Ar. In the experiments reported here, the ^{37}Ar atoms were physisorbed on a cold substrate with a binding energy of less than 100 meV;[15] thus the recoil is expected to break the weak absorption bond. The K-hole created as a result of the EC reaction decays 90.3% of the time via Auger and 9.7% of the time via x-ray emission. Note that the ^{37}Cl atom with the K-hole is initially in a neutral charge state. When this ^{37}Cl atom decays by emitting Auger electrons and/or photons sequentially in a cascade, several new intermediate ion states will be produced until a stable final state is reached. The typical lifetime of an Auger decay is about 10^{-15} second, during which time the ^{37}Cl ion moves less than 0.1Å.

There are several intrinsic factors which lead to broadening in the recoil energy distribution of the Cl ions. First, the ^{37}Ar atom does not start out at rest, but has some initial thermal velocity, which at 16 K leads to a spread in the energy of the daughter ^{37}Cl of about 3% (or 0.28 eV). The Auger decay of the ^{37}Cl also gives a recoil and hence broadening in ^{37}Cl ion energy. A 2.4 keV KLL Auger electron ejected from a ^{37}Cl atom moving with 9.54 eV will lead to a broadening of 12.2% (or about 1.15 eV) due to recoil. This can be corrected if the direction of the Auger with respect to the Cl ion velocity is known. For the time-of-flight (ToF) geometry reported here, the Auger recoil slows down the Cl ions by 4.3% (or reduces the energy by 8.3%), with a residual spread of about 4%

due to the angular opening of the MCP detector. Similarly, an LMM Auger recoil will change the ^{37}Cl ion energy by 3.52% (or 0.34 eV). On the other hand, a 2.6 keV x-ray photon will cause only a 0.65% (or 0.06 eV) change in energy of the Cl ions due to recoil. There is also broadening due to instrumental effects, such as variation in the flight distance over the finite size of the detector and source, and variation in the time ions spent between the retarding screens and the detector. A Monte Carlo simulation was performed to generate ToF spectra which take all of the above effects into account. The result shows a velocity broadening of about 20% if either a KLL or an LMM Auger is detected in coincidence with the ion, and a broadening of 14% if only a KLL Auger is detected in coincidence with the ion (Fig. 4.1).

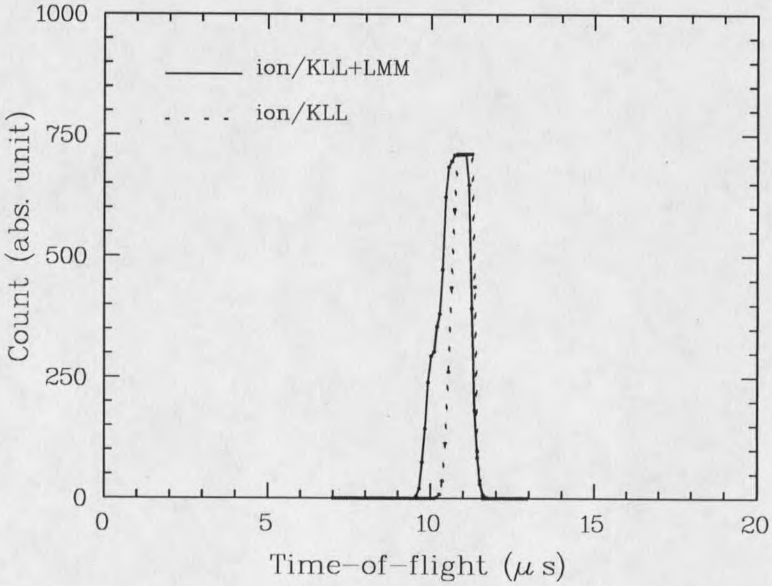

Figure 4.1 The Monte Carlo simulations of the ^{37}Cl ion recoil velocity distributions. Solid line: ^{37}Cl ions in coincidence with either KLL or LMM Auger electrons. Dash line: ^{37}Cl ions in coincidence with KLL Auger electrons only.

The above discussions and simulations dealt with only the isolated ^{37}Ar atom case. Comparing with these estimates of what to expect for an isolated ^{37}Ar atom, the real case, the results of actual measurements are presented below.

Figure 2(a) shows the ToF spectrum of the recoiled ^{37}Cl ions, taken in coincidence with Auger electrons having kinetic energies above 50 eV (-50 V retarding voltage on MCP2 screen), *i.e.,* in coincidence with either an LMM Auger electron (E ≈180 eV) or a KLL Auger electron (E ≈ 2.4-2.6 keV). The experiment was conducted by using the first experimental setups as shown in Fig. 3.13. The sample was dosed to 1 ML of the $^{36/37}$Ar mixture. A +0.5 V bias was also supplied to the MCP1 detecting positive ions. The spectrum represents a total counting time of 172 hours.

The ToF spectrum shown in Fig. 2(a) was converted to an energy distribution spectrum using the measured distance of travel (7.8 cm) between the source and detector. Figure 2(b) shows the resulting kinetic energy distribution of the ^{37}Cl ions extracted from the ToF spectrum in Fig. 2(a). The absolute velocity scale was also verified by measuring the shift in the centroid of the ToF spectrum as the ion detector was moved by a known distance. The spectrum does not distinguish the charge state of the ions.

The energies (Fig. 2(b)) of the ions range from 5 eV to 13 eV with a maximum at around 9 eV. An important point to note here is that the ToF spectrum is taken in coincidence with ^{37}Cl KLL or LMM Augers, hence it is guaranteed that the ions are

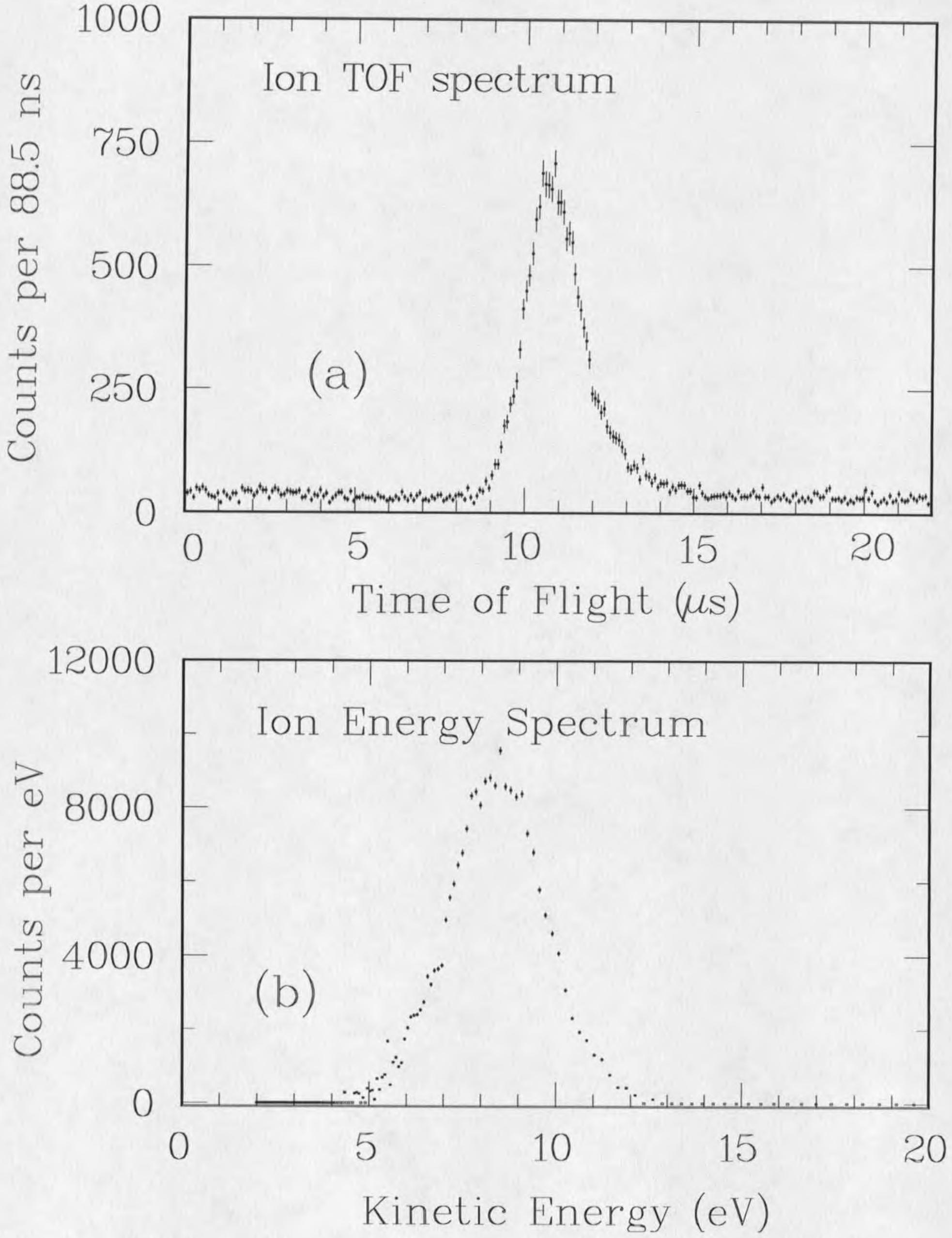

Figure 4.2 (a) Time-of-flight spectrum of the desorbing ^{37}Cl ions taken from the coincidence between ^{37}Cl ions and ^{37}Cl Auger electrons. (b) Accidentals-subtracted energy distribution of the desorbing ^{37}Cl ions, obtained from (a) using the measured time and distance of flight.

ejected as a result of neutrino emission. Compared with the estimates of an isolated atom, there are two features which were not anticipated: (1) The high energy tail of the spectrum (>9.4 eV) is too long to be accounted for by neutrino recoil or by the uncertainties in the

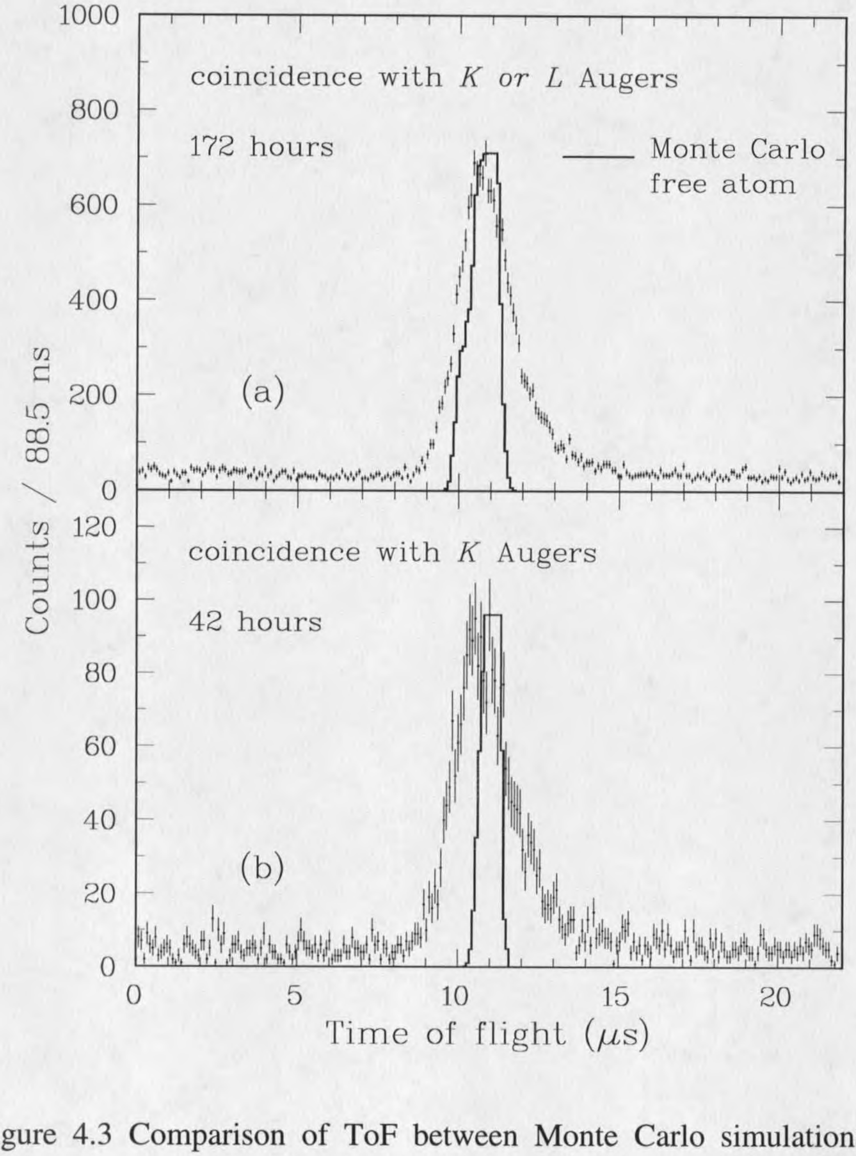

Figure 4.3 Comparison of ToF between Monte Carlo simulations and the results of coincidences: (a) ions and KLL or LMM Augers (b) ions and KLL Augers.

energy measurement (better than 4%), and (2) the energy spread (FWHM ≈ 3eV) of the ^{37}Cl ions is larger than the 20% estimate for the isolated atom case. The ToF spectrum in coincidence with KLL Augers only was also measured. Figure 3(b) shows the ToF spectrum of the desorbing ^{37}Cl ions, taken in coincidence with Auger electrons having kinetic energies above 250 eV (-250 V retarding voltage on MCP2 screen), *i.e.,* in coincidence with KLL Augers electrons (E ≈ 2.4-2.6 keV) only. This measurement used the same system as the one in Fig. 4.2(a) except the counting time was 42 hours. The FWHM of this spectrum was about 30%, whereas the expected spread was estimated to be 14% (superimposed in Fig. 4.3). Therefore there had to be other factors which would also contribute to the broadening of the recoil energy spectrum beside the intrinsic factors. These "surface interaction factors" will be discussed in later sections.

Charge-State Distribution of ^{37}Cl Ions

Immediately after the EC process, the ^{37}Cl atom is left with a K-hole or an L-hole and in a neutral charge state. This is a highly excited state which decays within 10^{-15} s by emitting Auger electrons and/or photons sequentially in a cascade. The ^{37}Cl atoms then become positively charged ions with different charge states. This charge-state distribution is decided by both the different relaxation channels of the initial K-hole or L-hole and by charge exchanges of the ^{37}Cl ions with their neighbors. Like the case of the recoil energy distribution study, the charge-state distribution of the isolated ^{37}Ar atom will be examined first in the next paragraph.

The charge-state distribution of the isolated Ar (gas phase) ion with an initial 1s hole has been discussed in Chapter 2. The theoretical and experimental results are listed in Table 2.5. Compared to Ar, each charge state of ^{37}Cl ions should have one charge less than the corresponding charge state of Ar ions resulting from the same Auger cascade. The charge-state distribution of ^{37}Cl ions in the gas phase has been measured by Kofoed-Hansen[23] and by Snell and Pleasonton[22]. The two experiments were in rough agreement, except for the charge 1 state, where Snell and Pleasonton got a much smaller fraction. By using the decay probabilities given by Chen, Crasemann and Mark[76] and taking into account that 90% of the ^{37}Cl start as neutral atoms with a 1s hole and 10 % with a 2s hole, a theoretical estimate was made by Monte Carlo simulations. The result for the charge 1 state is 9.1%, which is much closer to Snell and Pleasonton's value than to Kofed-Hansen's. For the other charge states the results are also in reasonable agreement with Snell and Pleasonton's data. The experiments cited above were not sensitive to neutral recoils, which can be estimated to constitute < 1% of the decays. The experimental and simulation results are listed in Table 4.1

Table 4.1 Experimental and Simulation Results on ^{37}Cl Ion Charge State Distribution.

Charge	+1	+2	+3	+4	+5	+6	+7
Exp.1(%)[23]	26±3	13±4	38±4	18±2	4±1	1±1	
Exp.2(%)[22]	6.2±.1	15.7±.4	39.2±.5	26.7±.4	10.0±.2	1.8±.1	.4±.1
Monte Carlo	9.1	18.8	48.7	17.7	5.1		

The charge-state distribution of ^{37}Cl ions which interact with their neighbors is now examined in this section. First, it is necessary to explain how to measure the charge-state distribution with a MCP based retarding field energy (RFE) analyzer. The RFE analyzer is an integrating spectroscopy and is sensitive to the charge states of the ions. The counts, $C(V)$ of ^{37}Cl ions at screen voltage, V of the RFE analyzer are related to the kinetic energy, E of the $^{37}\mathrm{Cl}^{+ne}$ ions (where n=1,2,3,...) through

$$C(V) = \sum_{n} \int_{E=neV}^{\infty} \frac{dC(n,V)}{dE} dE \tag{4.1}$$

where $C(n,V)$ is the contribution of the n-fold charged ions to the counts at screen voltage V and $\sum_{n} dC(n,V)/dE$ is the energy distribution of the ^{37}Cl ions as shown in Fig. 4.2(b). Figure 4.4 shows the effects of charge state and energy distributions to a RFE spectrum.

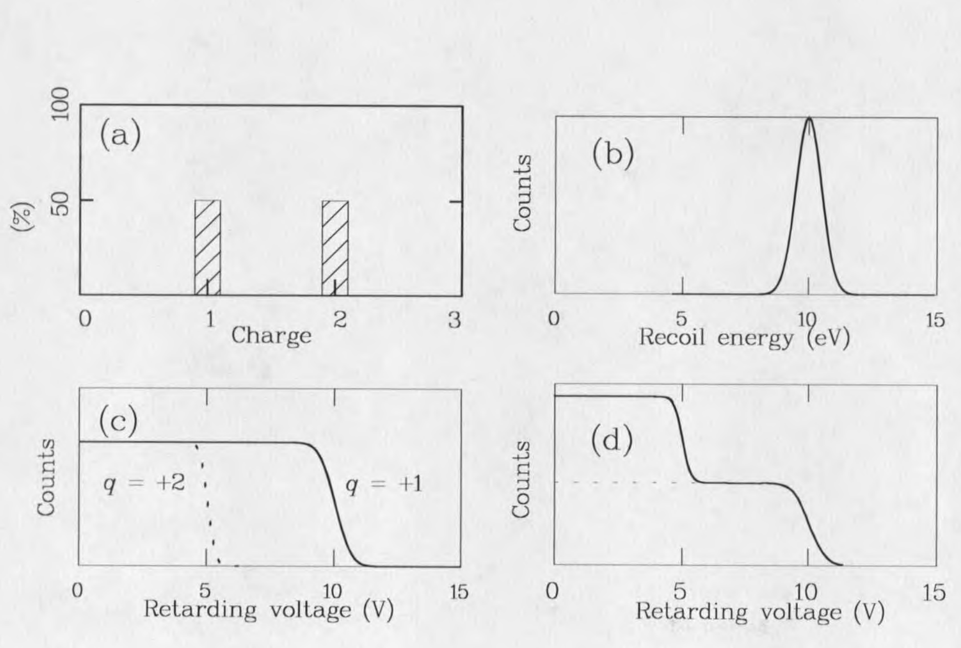

Figure 4.4 The distribution of (a) charge states and (b) ion energy. (c) The RFE spectra of q=+1 ions(solid line) and q=+2 ions(dash line). (d) The RFE spectrum of all ions.

A spectrum with charge state and energy distributions as shown in Fig. 4.4(a) and Fig. 4.4(b) would yield a RFE spectrum as shown in Fig. 4.4(d). Therefore the RFE spectrum is a convolution of energy and charge state distributions. If the energy distribution could be acquired by other means, the charge states distribution could be in principle obtained from the RFE spectrum.

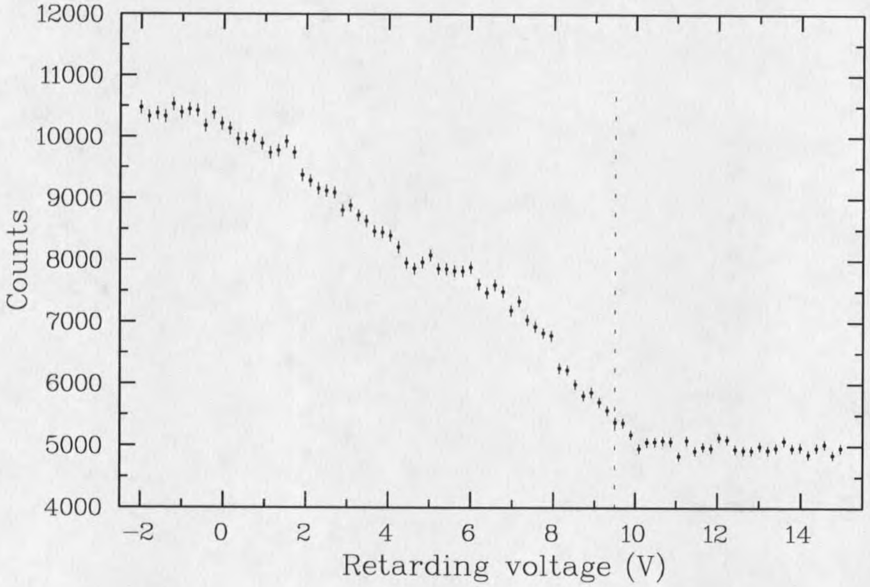

Figure 4.5 Retarding field energy (RFE) spectrum of the desorbing ^{37}Cl ions from 1 L $^{36/37}$Ar coverage. The vertical dashed line marks the position of the recoil energy of ^{37}Cl ions in the gas phase (9.54 eV)

Figure 4.5 shows the retarding field energy (RFE) spectra of the desorbing ^{37}Cl ions entering the MCP-RFE detector. The positive voltage applied to the middle screen (Fig. 3.13) provided the retardation. Each screen is 90% transparent, with a 100 μm mesh size. The dosage was 1L exposure of $^{36/37}$Ar mixture with ~50 ppm ^{37}Ar concentration on the Au/Si(111) substrate. The vertical dashed line in Fig. 4.5 marks the position of the recoil energy of ^{37}Cl ions in the gas phase (9.54 eV). There are several interesting observations that can be made from this spectrum.

The first one is the charge-state distribution of the desorbing ^{37}Cl ions. Figure 4.2(b) suggests that more than 95 % of the ion counts fall between 6 eV and 12 eV kinetic energy. Therefore, it is safe to assume that 6 eV and 12 eV are the lower and upper kinetic energy limits, respectively, for all ^{37}Cl ions desorbing from a monolayer of $^{36/37}$Ar mixture.

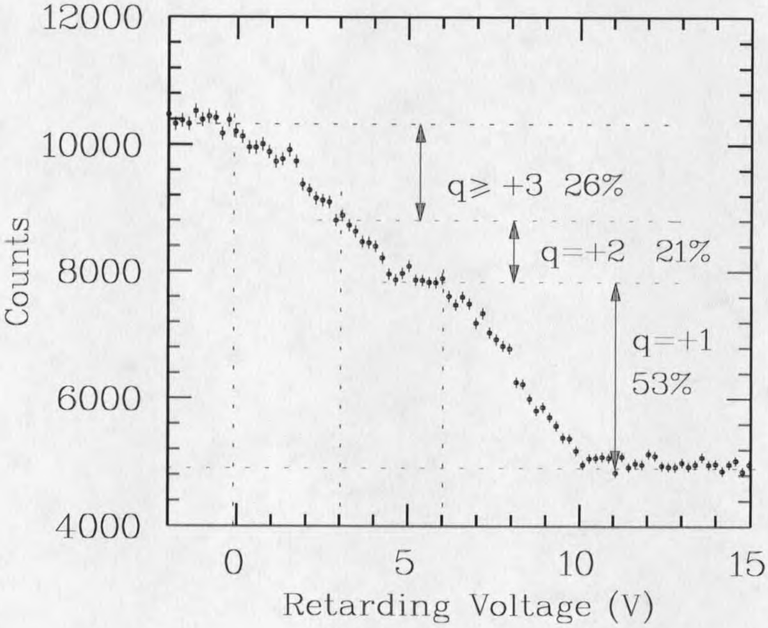

Figure 4.6 Charge state distribution obtained from the ^{37}Cl ion RFE spectrum.

These limits will be used to quantify the charge state distribution of ^{37}Cl ions desorbing from the surface. These kinetic energy limits imply that all ion counts above V = 6 V in Fig. 4.6 are due to $^{37}Cl^{+1e}$ ions. Further, the increase in the counts between 3 and 6 eV is due to $^{37}Cl^{+2e}$ ions, and the increase in counts between 0 and 3 eV is due to $^{37}Cl^{+ne}$ ions, with $n \geq 3$. The analysis of Fig. 4.6 yields immediately that ~ 53% of the total ions have charge +e, ~ 21 % have charge +2e and ~ 26 % have charge +ne, where $n \geq 3$ (Fig. 4.6). Since the MCPs cannot detect the neutrals, the percentage of the neutral ^{37}Cl atoms desorbing can not be measured directly. The indirect measurements suggesting an upper limit of 90% for neutralization will be discussed later.

The charge state distribution obtained from the RFE spectrum is substantially different from that expected for isolated atom decay (Fig. 4.7(a)). The comparison between the simulated RFE spectrum of the isolated ^{37}Ar and the real RFE spectrum is shown in Fig. 4.7(b). This discrepancy will be explained in terms of charge exchange and subsequent Coulomb repulsion in the discussion section.

The second point that needs to be addressed here is the difference between the highest kinetic energy of the $^{37}Cl^{+e}$ ions measured by RFE and that found by ToF. The maximum uncertainty in the energy measurements is less than 4 %, but yet the threshold of RFE starts at around 10 eV while the highest energy suggested by ToF is around 13 eV (Fig. 4.8). One possibility is that the energy distribution depends on the charge states of

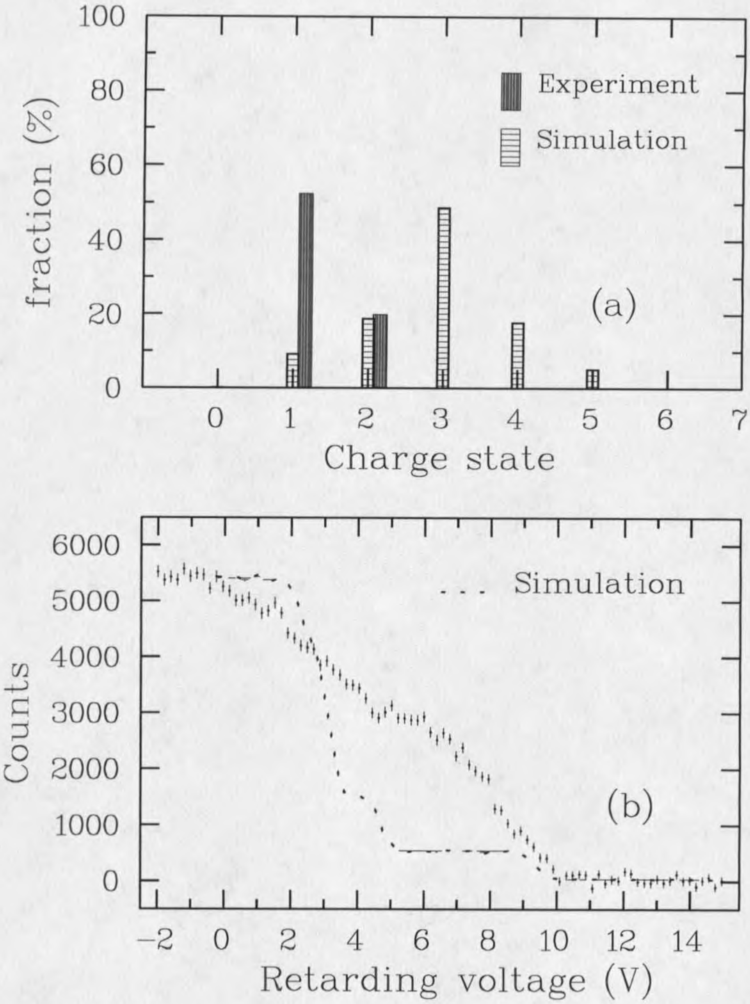

Figure 4.7 Comparison between the simulation of isolated Ar and the experimental results in (a) charge states distribution, and (b) the RFE spectra.

the ions, *i.e.,* the highly charged ions would have higher energy and these ions would not show up in the high voltage end of the RFE spectra because of the multiple retarding nqV. This assumption was tested by comparing the width of the ToF distribution with the retarding potential set to 0.5 V (which would allow all Cl ions to enter the detector) with the width of the distribution obtained by setting the retarding potential to 6.0 V (which would allow only singly charged Cl ions to enter the detector). Both distributions were obtained in coincidence with KLL Auger electrons. There was evidence of about 10 - 15 % narrowing but the statistics were poor because the source had decayed considerably by the time this measurement was conducted.

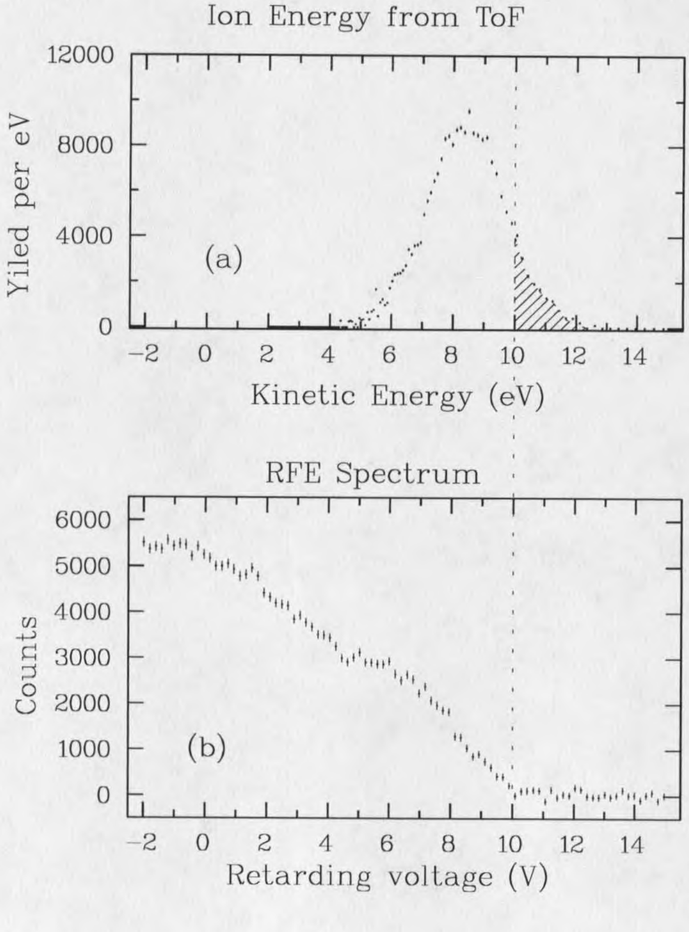

Figure 4.8 The maximum kinetic energy, E_k obtained by (a) ToF spectrum and (b) RFE spectrum. The shadowed region could be the contribution of higher charged ions.

Results on Multiple and Mixed Layers

The discrepancy between the expected charge-state distribution and the RFE experimental results and the higher maximum kinetic energy indicate that the ^{37}Cl ions have interacted and exchanged charges with their neighbors during the desorption process. In order to understand these interactions, several experiments were carefully designed. These experiments include studies of ^{37}Cl ion desorption processes from multiple layers of $^{36/37}$Ar gases and from mixed layers of $^{36/37}$Ar and ^{40}Ar gases.

Figure 4.9 shows the RFE spectra of ^{37}Cl ions from different coverage (1L, 2L, 4L and 7.4L) of $^{36/37}$Ar gases on the cold Au/Si(111) substrate. The sticking coefficient of Ar is about 1 at 16 K for up to 10 ML thickness.[13] This is confirmed by observing the linear increase of the KLL Auger electron counts (at ~ 2.4 keV energy) as a function of exposure, and also by comparing the count rate with that expected from the initial total decay rate of 2 x 10^4/s per monolayer of the $^{36/37}$Ar mixture (Chapter 3). Here a negligible loss of the KLL Auger electrons is assumed as they penetrate through a few Ar layers. Reproducibility of Ar coverage is the biggest unknown in the measurements. As the thickness of the Ar film increases, both the charge state and the energy distribution of the ^{37}Cl ions change. This is shown in Fig. 4.9(b) - Fig. 4.5(d), where the highest kinetic energy of the ^{37}Cl ions, E_k(max) increased to above 15 eV and the profile of the RFE spectra changed considerably over a range of ~7 L of $^{36/37}$Ar exposure.

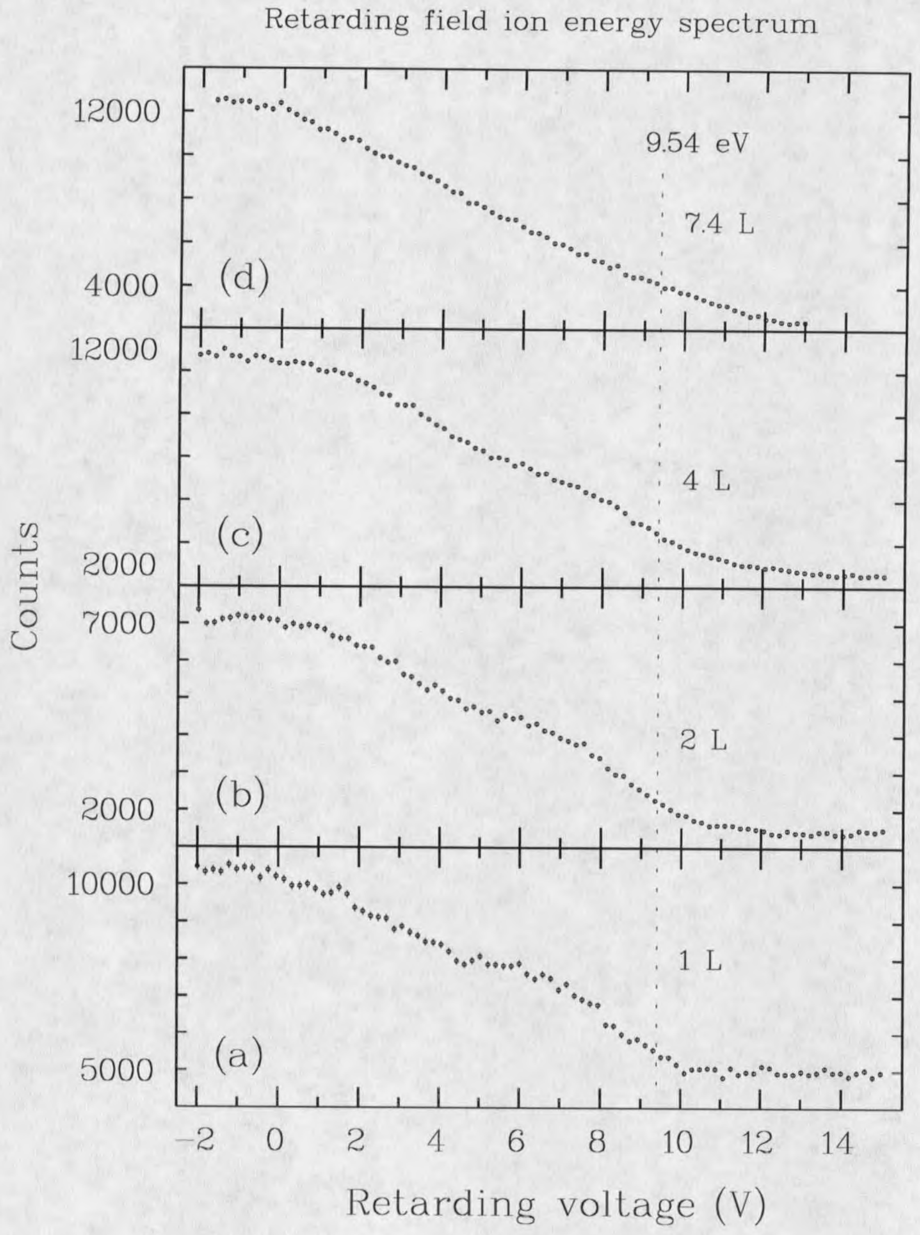

Figure 4.9 Retarding field energy (RFE) spectra of the desorbing ^{37}Cl ions at different coverage (1 L to 7.4 L). Note that as thickness increases there is an increase in E_k(max), and a change in the profile of the RFE spectra.

Figure 4.10(a) shows two superimposed RFE spectra from a monolayer $^{36/37}$Ar film. In one case (full line), the active film was physisorbed on the top of a 3L ^{40}Ar film and in the other case (dashed line) the active $^{36/37}$Ar film was deposited first on the Au substrate and followed by 3L of ^{40}Ar film. The curves are spline fits to the data points

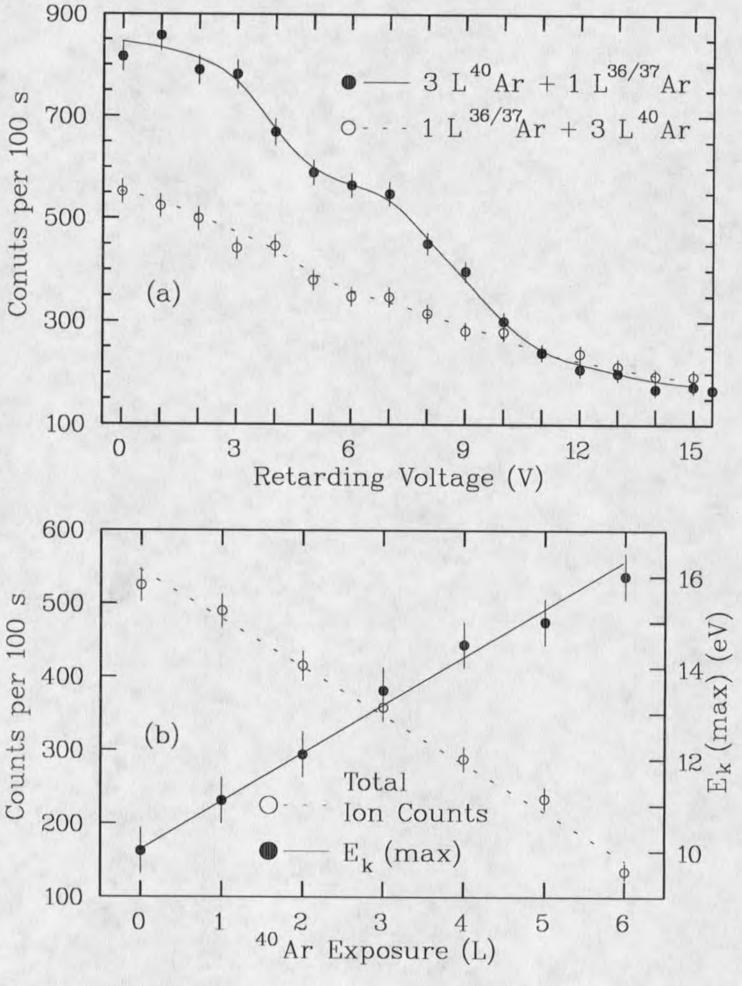

Figure 4.10 (a)Two superimposed RFE spectra from 1L $^{36/37}$Ar layer. Dashed line: 1L $^{36/37}$Ar at the bottom of 3L passive ^{40}Ar film. Full line: 1L $^{36/37}$Ar on the top of 3L ^{40}Ar film. (b) Dashed line: total ion intensity from a 1 L $^{36/37}$Ar as a function of ^{40}Ar coverage. Full line: E$_k$(max) from a 1 L $^{36/37}$Ar file as a function of the ^{40}Ar coverage.

(circles). Notice that the maximum kinetic energy, E_k(max), of the ^{37}Cl ions is about 13.5 eV in both cases but that the profiles and the intensities are very different. The profile of the top curve is similar to that of Fig. 4.9(a), while the profile of the bottom curve is similar to that of Fig. 4.9(d). The ^{40}Ar between the active ^{37}Ar and the substrate (top curve) served as a buffer layer to prevent charge exchange between the ^{37}Cl ions and the substrate. The fact that the charge state distribution did not change appreciably when the active layer was separated from the Au substrate by an additional three layers of ^{40}Ar means that the Au substrate is unlikely to be the significant source of charge exchange for the desorbing ^{37}Cl ions.

The variation in total ion yield and E_k(max) of a single layer of active $^{36/37}$Ar is shown in Fig. 4.10(b) as functions of passive ^{40}Ar physisorption exposure over the active layer. The total ^{37}Cl ion intensity decreases linearly at a rate of ~12 % per ^{40}Ar layer, and E_k(max) increases linearly at a rate of ~10 % per ^{40}Ar layer within 6 L of ^{40}Ar deposit. There is about a 5% uncertainty in determining E(max) from the RFE spectra, because of low counts at the thresholds.

The broadening of the energy distribution spectra (EDS) determined by ToF spectroscopy is shown in Fig. 4.11. The two normalized EDS correspond to 1L and 5L $^{36/37}$Ar mixture physisorbed on the Au/Si(111) substrate. Note that the 5L spectrum ranges from 5 to 16 eV while the 1L spectrum ranges from 5 to 13 eV. The EDS are rather symmetric in shape and the majority of the broadening takes place on the high-energy side of the EDS. There are some low kinetic energy ions below 5 eV but their contribution is rather small. The broadening in energy is explained in terms of charge exchange and Coulomb repulsion in the discussion section.

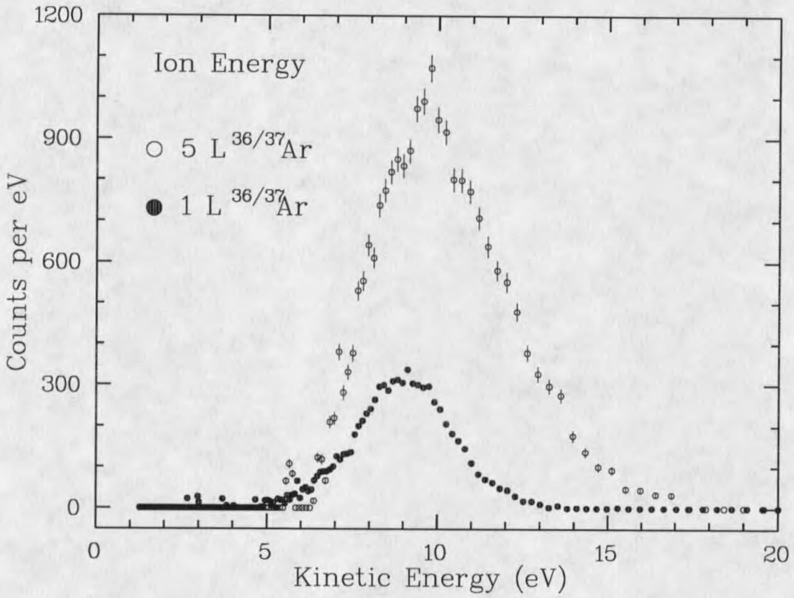

Figure 4.11 Energy distributions from a 1L $^{36/37}$Ar film (full circles) and 5L $^{36/37}$Ar film (empty circles). The counts are normalized. Notice the increase in E_k(max) and counts.

Desorption Probability of ^{37}Cl ions

The probability β that a ^{37}Cl ion is desorbed as a result of the neutrino emission accompanying the decay of its parent ^{37}Ar will be examined in this section. This probability can be determined reasonably well, as β can be measured independently by two methods: (1) the direct measurement using RFE spectroscopy, and (2) the indirect measurement using coincidence techniques. They produced the same result as expected.

Direct measurement of the probability β was performed by measuring first the number of KLL Auger electrons emitted from a 1 L $^{36/37}$Ar mixture. A retarding voltage of -400 V (selecting only KLL electron) was applied to MCP1 detector which was operated in electron detection mode for this measurement. Background counts (typically 1-2 cps) were carefully measured to find the net KLL Auger counts. This was followed by direct ^{37}Cl ion counts measurement in the same MCP detector biased now for positive ion detection. With a screen bias of +0.5 V, the MCP detector would detect all positive ions plus x-ray photons, if any. The background counts varied around 3 cps for the ion detecting mode and no x-rays were observed. The MCPs have a detection efficiency of 2±1 % for x rays, 85±10% for ^{37}Cl ions at 2.7 keV, and 85±2 % for electrons at 2.5 keV.[110-111.123] Since only 9 % of the total decays were accompanied by K x rays, only about 0.2 % of the total electron counts were due to x rays, and these could be ignored. Taking into account that there are 0.81 KLL Augers for every ^{37}Cl EC decay (90 % of capture occurs from the K shell and 90 % of the K holes decay by Auger emission), the KLL Auger electron and the ^{37}Cl ions counts for a total N_o EC decay events should be

$$N_{KLL} = N_0\, P_k\, (1-w)\, f_{K>400}\, (\Delta\Omega/4\pi)\, T_K\, \varepsilon_K\, \eta_K\, f_{live} \tag{4.2}$$

$$N_{ION} = N_0\, P_{ION}\, f_{ION>0.5}\, (\Delta\Omega/4\pi)\, T_{ION}\, \varepsilon_{ION}\, \eta_{ION}\, f_{live} \tag{4.3}$$

where $P_K = 0.9$ is the K-capture probability, $w = 0.1$ is the radiative transition probability for a K hole, $f_{K>400} = f_{ION>0.5} \approx 1$ are the portion of a KLL Auger electron whose energy is greater than 400 eV and an ^{37}Cl ion whose energy is greater than 0.5 eV when leaving the surface (scattering effect), $(\Delta\Omega/4\pi)$ is the solid angle of the MCP detector, $T_K = T_{ION} = 0.72$ are the transmissions of the three screens in front of the MCPs for KLL Auger electrons and ions, $\varepsilon_K \approx \varepsilon_{ION}$ are the efficiencies of the MCP and the electronics system for 2.5 keV KLL Auger electrons and 2.7 keV ions (accelerated), $\eta_K = \eta_{ION}$ are the chances of escape for KLL Auger electrons and ions from anything which might cover them during the measurement and f_{live} is the computer efficiency (live time/dead time). Some of the values given above may not be exact and there might be some other factors which will affect the yields, but most of these factors will cancel each other when calculating the desorption probability P_{ION} by dividing Eq. (4.2) by Eq. (4.3)

$$P_{ION} = 0.81\, N_{ION} / N_{KLL} \tag{4.4}$$

From Eq. (4.4) the desorption probability of ^{37}Cl ions is calculated as $P_{ION} = 9.4 \pm 1.2$ %. This result suggests that, at most, 90.6 % of the Cl atoms are recaptured or desorbed in the neutral charge state. The largest uncertainty (12 %) in the measurement is due to uncertainty in the detection efficiency of the ^{37}Cl ions.

The second method of measurement makes use of the coincidence techniques. The basic idea is to compare: (1) the number of coincidences between the ^{37}Cl ions and the KLL Auger electrons, (*i-e*), and (2) the coincidence between the LMM and KLL Auger electrons (*e-e*). Typical (*i-e*) and (*e-e*) spectra are shown in Fig. 4.2 (a) and Fig. 4.12, respectively. The FWHM of the peak in Fig. 4.12 is ~ 2 ns. Most of the broadening of the peak comes from the energy spread of the LMM Auger electrons ranging from 100 eV to 200 eV (~ 4 ns spread in 8 cm). The absolute time resolution of the system is better than 1 ns. The detailed analysis of Fig. 4.12 will be in next section. Here, only the coincidence counts of the (*i-e*), N_{KION} and (*e-e*), N_{KL} are needed.

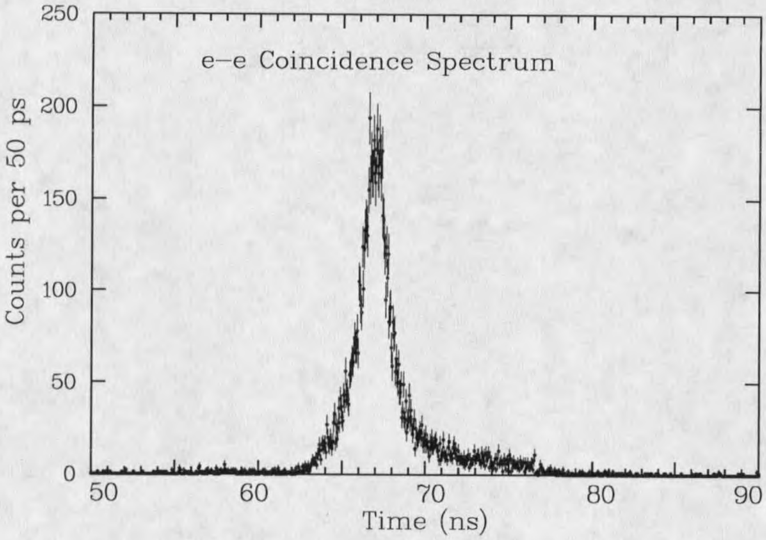

Figure 4.12 KLL and LMM *e-e* coincidence and ToF spectrum. Most of the broadening of the peak is due to a spread in the energy of LMM electrons (100-200 eV).

$$N_{KL} = N_0\, P_k\, (1-w)\, [\, 2 f_{KLL} + f_{KLM}\,]\, f_{K>400}\, f_{L>100}\, (\Delta\Omega/4\pi)^2\, T_K\, T_L\, \varepsilon_K\, \varepsilon_L\, \eta_K\, \eta_L\, f_{live} \qquad (4.5)$$

$$N_{KION} = N_0\, P_k\, (1-w)\, P_{ION}\, f_{ION>0.5}\, (\Delta\Omega/4\pi)^2\, T_K\, T_{ION}\, \varepsilon_K\, \varepsilon_{ION}\, \eta_K\, \eta_{ION}\, f_{live} \qquad (4.6)$$

where $2 f_{KLL} + f_{KLM} = 1.84$ is the number of LMM electrons created per KLL Auger decay and $f_{KLL} = 0.85$ and $f_{KLM} = 0.15$ are chances of a K hole decay through KLL and KLM

Auger, respectively. Other parameters are self-explanatory with the subscript K and L standing for KLL and LMM Auger. The desorption probability can be expressed as

$$P_{ION} = 1.84\, N_{KION} / N_{KL} \tag{4.7}$$

The resulting desorption probability of ^{37}Cl ions is found to be, P_{ION} = 9.6 ±1.2 %, in excellent agreement with the result of the first method.

Discussion of the Desorption Results

The discussion of the desorption results will be centered around two related topics: the local environment surrounding an ^{37}Ar atom, and the interaction of the ^{37}Cl ion with its surroundings and possible mechanisms for energy broadening.

In order to form a solid Ar film on the substrate, the sample had to be cooled down to 16 K in 3 hours. The entire sample surface facing the MCPs was uniformly flat with no physical defects. It is quite likely that there was at least one layer of residual gas physisorbed on the Au surface during the time the sample was cooled down, although it could not be detected by Auger spectroscopy. The $^{36/37}$Ar film was most likely physisorbed on top of this layer. For one (or less) monolayer of $^{36/37}$Ar film, a typical ^{37}Ar will be surrounded by ^{36}Ar atoms on the surface and residual gas molecules underneath (Fig 4.13(a)). Typical residual gases in this UHV system were H_2, CH_n, H_2O, CO, CO_2, and $^{36/37}$Ar mixture. An experiment for 1 L exposure was typically run for 8 hours, with ToF spectra saved every two hours automatically before desorbing the old layer and adsorbing a fresh layer of $^{36./37}$Ar. Time-dependent analysis of ToF and RFE spectra showed no noticeable differences in the count rates or the shapes of the spectra during the 8-hour period. The residual gases (if any) on top of the $^{36/37}$Ar film introduced no observable effect. As mentioned earlier, layers of ^{40}Ar physisorbed over and/or under an active layer of $^{36/37}$Ar film caused the same amount of increase in E_k(max) (Fig. 4.10) from 10 to 13.5 eV. On the other hand the RFE spectra vs. V resembled Fig. 4.2(a) if the active layer was on top of ^{40}Ar layers, and looked like Fig. 4.9(d) if the active layer was at the bottom of the ^{40}Ar layers. Fig. 4.10(b) shows a linear increase in E_k(max) as ^{40}Ar layers pile up on top of the $^{36/37}$Ar active layer. This behavior is puzzling, since it suggests that not only the near-neighbor atoms but also atoms far from the active center interact with the ^{37}Cl ions during desorption. A second puzzling behavior is the large penetration

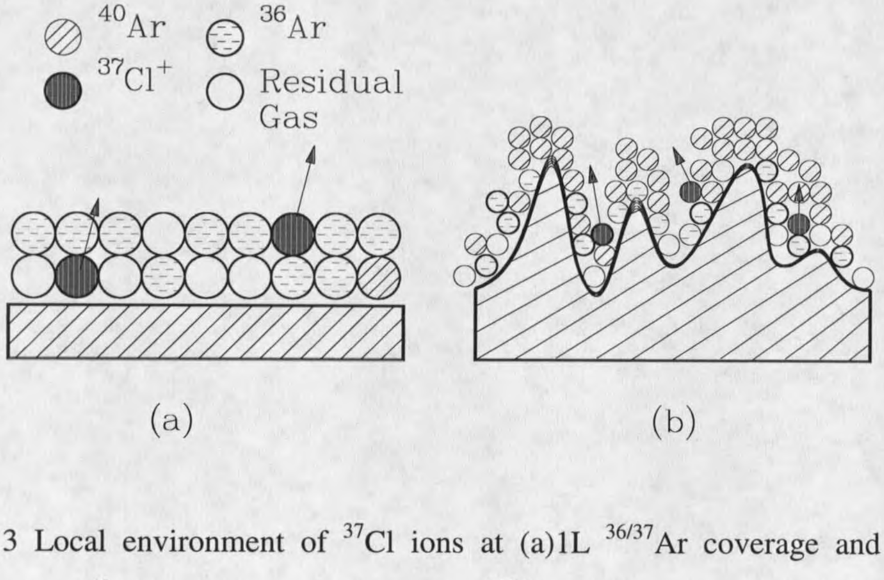

Figure 4.13 Local environment of ^{37}Cl ions at (a)1L $^{36/37}$Ar coverage and (b) more realistic case for ^{40}Ar on the top of 1L active $^{36/37}$Ar mixtures—the morphology of the films is a porous structure.

depth of the ^{37}Cl ions, as indicated in Fig. 4.10(b). It is possible that the morphology of the films is not close-packed but rather a *porous* structure, which would explain the behavior shown in Fig. 4.10(b). The Au substrate, which forms the base for the Ar films, is not an atomically flat surface, and could thus cause a porous film structure (Fig. 4.13(b)). This would increase the effective surface area and would explain the large penetration depth and the long-range interaction of ^{37}Cl ions during desorption.

As mentioned earlier, the EC decay of ^{37}Ar and the subsequent Auger cascade leave behind a positively charged ^{37}Cl ion. The majority of the ^{37}Cl ions are initially in an n= 3 charge state (Table 4.1), which makes them highly reactive and ready to accept electrons from the sample environment during their motion, since the electronic transitions are very fast (typical lifetime of 10^{-15} s) and can easily occur before the ion leaves its initial environment (typical speed of 1 cm / μs). Figure 4.6 suggests that 53 % of the total ions are in the n = 1 state, 21 % in n = 2, 15% in n = 3 and 11% in n ≥ 4 as opposed to about <1 % in n = 0, 6 % in n = 1, 16% in n = 2, 39% in n = 3, and 38% in n ≥ 4, in the gas phase.[22,23] Essentially all the recoiling ^{37}Cl should be positively charged, but only 10% of them were being detected. The question one then asks is what happened to the other 90 %? The fact that 53 % of the observed ions have a charge of +1, whereas only 6 % are predicted to have charge +1, could have two explanations: (1) Most of the n = 2 and higher charge states do not desorb, thus increasing the apparent fraction of n =1 desorbed ions, and/or (2) most of the ions are neutralized by charge transfer before desorbing. The second argument is clearly more plausible as the cause of the high fraction of +1 ions. One piece of evidence for this is that coincidences were observed between charge +1 ions and KLL Augers. In the gas phase the n = 1 ions result only from K holes which decay by X- ray emission[22] and should not be in coincidence with the KLL Auger electrons, while the overwhelming majority of Auger decay of K-holes yield ions of charge 2 or higher. Therefore, the observation of charge 1 ions in coincidence with KLL Augers suggests that the ions became singly charged by picking up electrons *after* the Auger decay. This shows that the final charge state is a strong function of the local environment of the ^{37}Cl ions.

Whether a ^{37}Cl ion can transfer charge between itself and the neighboring atoms (or substrate) is determined by the ionization potentials of the interacting species. The ionization potentials of $^{37}Cl^{+ne}$ ions are about 13, 23, 40, 54, and 68 eV for n = 0, 1, 2, 3 and 4, respectively. The ionization potentials of the surrounding species are 16 eV for Ar, 4.5 eV for the Au substrate, between 10 and 13 eV for CH_n ($n \leq 4$), and between 13 and 15 eV for CO, CO_2, H_2O, and H_2. According to the discussion in chapter 2, the available energy has to satisfy Eq. (2.18), $E > I - A + T$, for singly charged ions to transfer charge. These numbers indicate that energetically a single charged $^{37}Cl^{+e}$ ion can easily receive an electron from the Au substrate and be neutralized, but that it cannot receive an electron from a nearby Ar atom. The neutralization of a singly charged $^{37}Cl^{+1}$ ion (either comes directly from the 10% x-ray relaxation or from a higher charge ion losing its charge) will be discussed in next paragraph.

In general, both resonant and direct Auger mechanisms may contribute to the neutralization. Since the work function of the surface is about 5 eV, a 13 eV deep $^{37}\mathrm{Cl}^{+1e}$ vacancy is enough for the direct Auger transition to occur. The direct Auger transition is the major channel for the neutralization where another electron is ejected from the substrate when the $^{37}\mathrm{Cl}^{+1e}$ is neutralized. Hagstrum[26] has deduced that essentially all neutralization occurs by this mechanism for ions with energies less than 10 eV. The survival rate of singly charged ions approaching a metal surface has been studied by theoretical and experimental groups.[26,27] In some cases, the metal is modeled as "jellium", *i.e.,* as an electron gas embedded in a constant positive background. A good approximation to the probability density for electron transfer from the metal surface to an ion on an incident trajectory is given phenomenologically by Hagstrum and Snowdon *et. al.*[26,27] as

$$P_t(S,|v|) = \left(\frac{A}{|v|}\right)\exp\left[-\left(\frac{A}{a|v|}\right)e^{-aS} - aS\right]\theta(S - S_0) \tag{4.8}$$

where S is the distance of the ion from the surface, v is the velocity in direction perpendicular to the surface, $\theta(x)$ is the step function and S_0,, a and A are constants determined by fitting experimental data. Since only the absolute value of v enters the equation, this relation should be applicable to the case of outgoing ions, as in this experiment. For this application, it is appropriate to set $S_0 = S_\tau$ the mean distance beyond which the ion will not be neutralized.

$$S_\tau(v) = v\tau + r_{Ar} \tag{4.9}$$

where τ is the mean life time of the ^{37}Cl excited state and r_{Ar} is radius of ^{37}Ar atom prior to decay. The velocity of a 9.54 eV ^{37}Cl ion is 0.071 Å/fs, and the mean life time is about 9 fs, which is the sum of the times filling holes in K-shell (~1fs) and the L-shells (~8fs) sequentially. Taking the radius of an Ar atom on the surface to be 1.86 Å,[24] one obtains S_τ = 2.5 Å. By using the values suggested by Hagstrum for the parameter a = 2.29 Å^{-1} and A =210 fs^{-1}, the ^{37}Cl ion charge transfer probability density P_t vs. S is calculated as shown in Fig. 4.14(a). The probability of survival of Cl$^+$ ion at distance S is then

$$P_S(S,|v|) = 1 - P_n(S,|v|) = 1 - \int_0^S P_t(S',|v|)dS' \tag{4.10}$$

which is shown in Fig. 4.14(b). From Fig. 4.14 (b) one can see the survival probability of Cl$^+$ ions beyond 5 Å is predicted to be very small. This explains the experimental result that up to 90% desorbed species were neutral. After neutralization, an Antoniewicz mechanism as illustrated in Fig. 2.3 might add additional energy to these desorbing neutrals on the top of the 9.54 eV recoil energy.

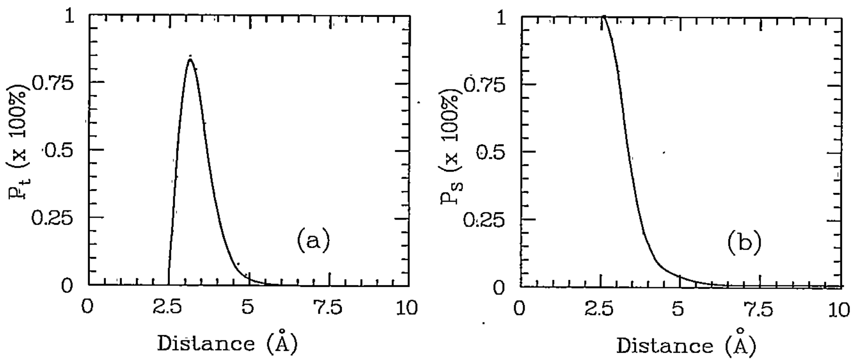

Figure 4.14 (a) The Cl$^+$ ion charge exchange probability density vs. distance. (b) The Cl$^+$ ion survival probability vs. distance.

One way to prevent the neutralization is to put several layers of stable Ar (*e.g.*, ^{40}Ar) between the substrate and the ^{37}Ar. As discussed above, a $^{37}Cl^{+1}$ ion cannot transfer charge from an Ar atom nearby, so therefore neutralization will not occur this way. The effect of such a "buffer zone" has been observed by Dujardin, *et. al.*[68,69] in their PSD experiment of Ar on Pt. They report the yield of Ar^{+} ions increases rapidly with the addition of each monolayer of Ar between the second and fifth monolayer, but reaches saturation for thicker layers. In fact the effect of the extra layers in between can be expressed as

$$S_{\tau}(v) = v\tau + r_{Ar} + M\, r_{Ar'} \tag{4.11}$$

where M is number of stable monolayers and $r_{Ar'}$ is the effective thickness of one monolayer of Ar (2.63 Å, assuming a *fcc* structure of Ar)[16]. Using the numerical value and simple relationships given in Eq. (4.11), the survival probability from the substrate charge transfer neutralization, P_S is near 1 for $M \geq 3$.

The charge transfer of a multiple charged $^{37}Cl^{+ne}$ ($n \geq 2$) ion can occur through different channels. Beside being neutralized by the conductive substrate, it can also receive an electron from any species surrounding it and reduce its charge state by one charge. This charge transfer is mainly due to the resonant tunneling mechanism. Similar to the "Coulomb explosion" model for covalent systems discussed in Chapter 2, the multiple vacancies left in the final state of the Auger cascade in the ^{37}Cl ions can be filled by the electrons from neighboring atoms. The energy required for a $^{37}Cl^{2+}$ ion to transfer a charge with a neighboring Ar atom is $E > (V_{II} - V_{I})_{Cl} - (V_{I})_{Ar} - T$, where V_I and V_{II} are the first and second ionization potential, and *T* is the kinetic energy gained in the process (Eq. (2.19)). The data shown before indicate that this process can happen for $n \geq 2$ ions. For example, a $^{37}\mathrm{Cl}^{+2}$ ion can release 23 eV energy when it receives an electron to become $^{37}\mathrm{Cl}^{+1}$, while a neighboring Ar atom only needs 16 eV energy to supply the electron. For this $^{37}\mathrm{Cl}^{+2}$ ion, after the initial charge transfer, further charge exchange is strongly inhibited because the $^{37}\mathrm{Cl}^{+1}$ ion cannot exchange charge with neighboring Ar atoms. This gives an extra long life time for the two adjacent positive ions. Part of the 7 eV excess energy released in this charge exchange will become kinetic energy of the interacting species and the rest will most likely remain as internal energy (*e.g.*, excited states) (Fig. 4.15). For an $^{37}\mathrm{Cl}^{+3e}$ ion, charge exchange would release even more kinetic energy. This effect would lead different charge states to have different energy distributions.

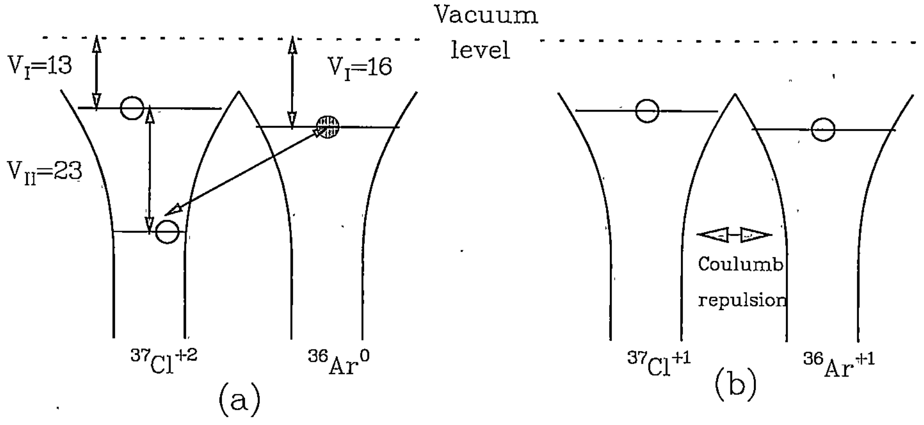

Figure 4.15 (a) The charge exchange of a $^{37}\mathrm{Cl}^{2+}$ with the neighboring Ar atom. (b) The Coulomb repulsion between the two holes resulting from the charge exchange

As explained earlier in this chapter, the *expected* recoil energy of the ^{37}Cl ions is 9.54 eV with a broadening of 20 % (2 eV), due primarily to the recoil induced by Auger electrons. The measured ion energy distribution for the 1 ML active layer on Au is a Gaussian with a maximum at 9 eV and a FWHM $\leq$ 3 eV. The maximum possible uncertainty in the energy distribution measurement is less than 4 %. Hence while the energy centroid is close to the expected position, the energy broadening is at least 50 % larger than expected. This means that charge exchange and the subsequent Coulomb repulsion shape the energy distribution. In the case of the 1 ML active layer it is expected that the kinetic energy of the ^{37}Cl^{+ne} ($n \geq 2$) ions is greater than that of the ^{37}Cl^{+e} ions as shown in Fig. 4.8. The reason for this is that most of the ^{37}Cl ions have already exchanged charges with the residual gas layer or with the Au substrate. Since the ^{37}Cl ions are on top of the residual gas layer, the charge exchange and the subsequent Coulomb repulsion give more energy to multiple charges than to single ones. In the case of multiple layers the situation is different: most of the active atoms have passive layers above them. In this case it is possible that a ^{37}Cl^{+ne} ions could transfer most of its kinetic energy and part of its charge to an Ar atom. The resulting Coulomb explosion would give additional kinetic energy to the Ar^{+e} ion, which would then have a chance to be detected in coincidence with an Auger electron from the ^{37}Cl atom. A single-charged Ar detected in this way would have more or less the same energy as the multiply-charged ^{37}Cl ions. The detector cannot differentiate between a ^{37}Cl and an Ar ion entering the detector. This idea will be tested in the future using Xe overlayers on an active $^{36/37}$Ar layer. The mass difference is large enough to differentiate whether a ^{37}Cl or a Xe ion is entering the detector.

Auger Relaxation of a ^{37}Cl Atom

The electron capture decay of ^{37}Ar leaves the ^{37}Cl atom with a K-shell hole 90% of the time and an L_1-shell hole 10% of the time.[8] These highly excited initial states of the ^{37}Cl atom will decay through radiative (x-ray emission) or non-radiative (Auger) transitions. The K-hole created as the result of EC process will decay 90.3% of the time via Auger and 9.7% of the time via x-ray emission.[8] As discussed in Chapter 1, the EC decay creates an excited ^{37}Cl atom whose initial state is unusual in three ways. First, there is a single hole created in the K-shell while the rest of the shells are essentially intact, leaving the ^{37}Cl atom with the electronic configuration of Ar. Second, the initial state is neutral, unlike the ionized state obtained by electron or photon bombardment. Third, with 90% of the electron capture occurring in K-shell, this initial state is almost a pure K-hole state, while the initial states obtained from the conventional ways are predominantly L-hole states. For example, when Ar is bombarded with 5 keV electrons, the fraction of K-holes created is over two orders of magnitude less than that of L-holes. It might be possible to improve this ratio with a photon beam having variable energy, but multiple ionization associated with photo-absorption might obscure the multiple ionization associated with decaying of the K-hole. Therefore, this unique initial state brought about by the EC process allows the direct observations of some interesting relaxation processes which are amenable to many-body theoretical calculations, but essentially impossible to probe experimentally using conventional techniques. This section is devoted to a discussion of the two phenomena which have been predicted theoretically,[4,30,31] but not observed directly: the shift in energy of an normal LMM Auger line due to a multiply ionized L shell and the decay of a K-hole by double Auger emission in the ^{37}Cl atom.

^{37}Cl LLM and LMM Auger Peaks

As discussed in Chapter 2, right after the EC decay, the core levels of an ^{37}Ar atom change immediately to the core levels of a ^{37}Cl atom with the K-shell at 2822 eV, the L_1 shell at 270.2 eV, the L_2 shell at 201.6 eV, the L_3 shell at 200.2 eV, the M_1 shell at 17.5 eV, and the M_2 and M_3 shells at 6.8 eV (Table 2.2). From Eq. (2.26), the KLL Auger energies of a ^{37}Cl atom could be calculated as from 2232 eV for KL_1L_1 (6.9%) to 2377 eV for $KL_{2,3}L_{2,3}$ (55.4%) Auger. Unfortunately, these energies are out of the measuring range of the CMA used in this work which can only detect a kinetic energy up to 2000 eV. Therefore, the emphasis of study was put on the LLM and LMM Auger cascades following a KLL Auger. The LMM Auger energies were calculated as from 150 eV ($L_3M_1M_1$) to about 250 eV ($L_1M_{2,3}M_{2,3}$) with major peaks at around 170 eV. Two independent experiments were conducted to study the LMM and LLM Auger energies: the retarding field energy distribution measured by the channeltron or MCP detectors and the differential energy distribution (dN/dE) measured by the CMA.

Figure 4.16 shows the RFE spectrum of a 4 ML $^{36/37}$Ar mixtures on the Au/Si(111) substrate taken in the early stage of the experiment by using a channeltron detector with retarding screen (Fig. 3.5). The main feature here is the sudden change of slope from 150 V to 180 V retarding voltage (The *absolute* voltage values are shown in this section. For electron measurements, the retarding voltages are negative.), hence 150 eV to 180 eV kinetic energy that corresponds to Cl atom LMM Auger peaks centered around 170 eV. This result was the first indication that confirmed the adsorption of ^{37}Ar atoms on the cold substrate. The spectrum is flat after 200 V retarding voltage and would stay this way until it reaches the KLL Auger energies. A maximum of 1000 V retarding voltage has been applied in similar experiments and no surprising result was found above 200 V retarding voltage. The result of the measurement during which the sample was mechanically blocked is also shown at the lower part in Fig. 4.1. This curve shows the

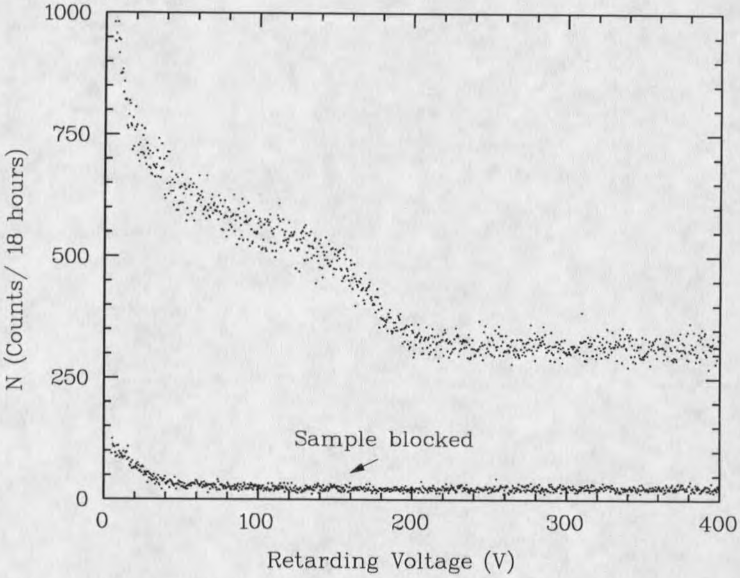

Figure 4.16. The RFE spectrum of ^{37}Cl LMM Auger. The lower curve was the result when the sample was blocked.

very low background count rate in this experiment. The poor resolution of this spectrum is due to the intrinsic limitation of the RFE detectors.

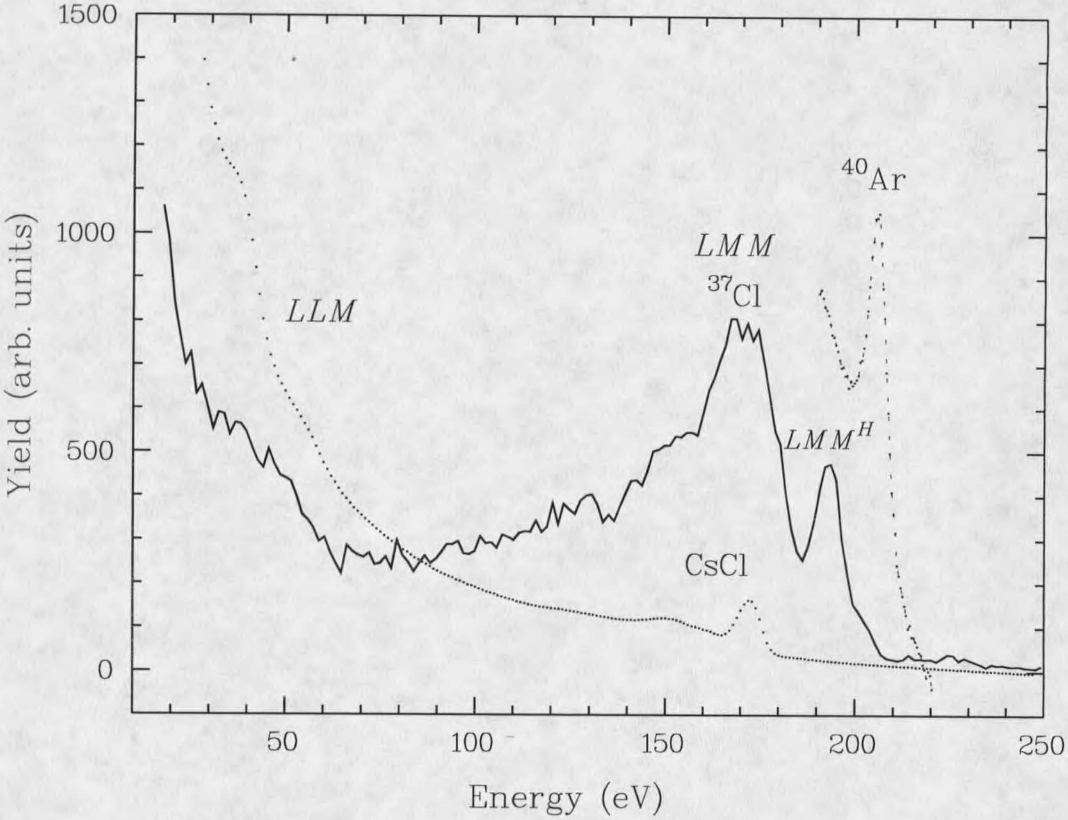

Figure 4.17 Comparison of varies Auger spectra. Full line: ^{37}Cl LMM following EC decay. Dotted lines: regular Auger from ^{40}Ar and CsCl excited by electron bombardment, with their background subtracted. LMM^{H} labels the hypersatellite peak.

Figure 4.17 shows three superimposed Auger spectra in the LLM and LMM regions of Cl and Ar. The full line is the ^{37}Cl Auger spectrum associate with ^{37}Ar EC decay. No background subtraction or signal smoothing has been carried out to present the data. The spectrum was taken with a double pass CMA. The peak labeled as LLM and LMM are those associated with known Cl Auger lines in the Auger spectrum taken from CsCl salt, also shown in Fig. 4.17. The CsCl spectrum was taken by Phi-595 scanning Auger system and was normalized and background-subtracted to fit to the scale of the ^{37}Cl Auger. For comparison, it also shows the LMM Auger peak of natural ^{40}Ar gas physisorbed on the same substrate and bombarded by a 1000-eV electron beam. It is worth noting that the ^{37}Cl spectrum was taken with only 5×10^{-5} effective monolayer, while the natural ^{40}Ar spectrum was taken with multiple layer coverage. In Fig. 4.17, one can compare the Cl Auger peaks from the ^{37}Cl and from CsCl. The LMM and LLM Auger peak energies (~170 eV and ~40 eV) and shapes from these two different sources are similar except the different backgrounds and an extra peak labeled as LMM^{H}, a *hypersatellite* peak. This extra peak became one of the subjects of this work. A higher resolved spectrum with the LMM^{H} peak is shown in Fig. 4.18. This spectrum was taken with the new radioactive ^{37}Ar source made from the ^{40}Ca(n,α)^{37}Ar nuclear reaction and the new substrate of pyrolytic graphite. The fact that LMM^{H} peak appears in both experiments with different radioactive sources and substrates indicates that it is not a solid state or surface contamination effect. The LMM^{H} peak with such a large shift (about 22 eV higher energy than the normal LMM line) has not been reported before. Notice that LMM^{H} peak does not appear in the normal Cl Auger spectra. A high resolution gas phase study on Ar LMM Auger[29] did not report such peak either. The new peak was only seen in this experiment with the ^{37}Ar sources.

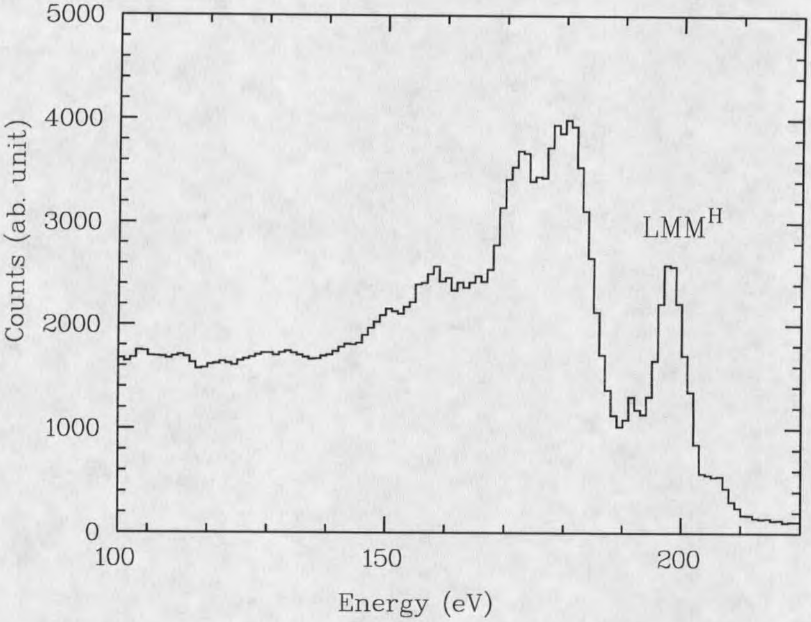

Figure 4.18 ^{37}Cl LMM Auger peaks measured from the new radioactive source and substrate.

Discussion of ^{37}Cl LMM Auger Results

The discussion of the LMM Auger results will be centered around two related topics: the peak assignments of the ^{37}Cl LMM Auger spectrum and the hypothesis explaining the extra LMM^H peak. As discussed in Chapter 2, the LMM Auger peaks of the ^{37}Cl following the EC decay would likely have energies of normal Cl Augers and structures of normal Ar Augers. Table 2.4 shows the energies of twelve major Auger lines from a highly resolved Ar LMM Auger spectrum.[29] Unfortunately, there is no Auger spectrum of Cl with such high resolution found in the reference. To get the corresponding Cl Auger peak energies, each group of the Ar Auger lines in Table 2.4 was shifted

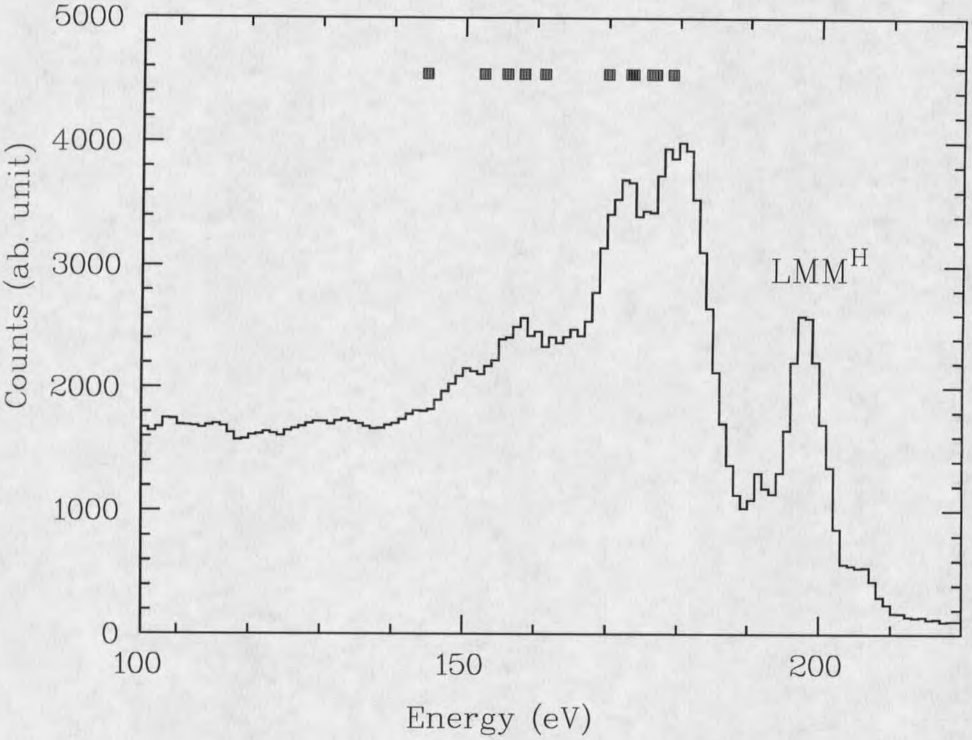

Figure 4.19 The normal Cl LMM Auger energies marked on the top of the ^{37}Cl LMM Auger spectrum. Note that no normal Auger peak is corresponding to the LMM^H peak.

according to the calculated energy differences between Ar and Cl Augers. For example, the calculated $L_2M_{2,3}M_{2,3}$ Auger energies were 212 eV and 182 eV for Cl and Ar, respectively. Therefore, the Cl $L_2M_{2,3}M_{2,3}$ Auger energy was obtained by shifting 30 eV from the corresponding Ar Auger energy. The resulting Cl LMM Auger energies are marked in Fig. 4.19 on top the ^{37}Cl LMM Auger spectrum. The Auger transitions with their final state spectral terms corresponding to these twelve Auger lines are, from higher energy to lower energy, $L_2M_{2,3}M_{2,3}(^3P_{0,1,2})$, $L_2M_{2,3}M_{2,3}(^1D_2)$, $L_3M_{2,3}M_{2,3}(^3P_{0,1,2})$, $L_3M_{2,3}M_{2,3}(^1D_2)$, $L_2M_{2,3}M_{2,3}$ $(^1S_0)$, $L_3M_{2,3}M_{2,3}(^1S_0)$, $L_2M_1M_{2,3}(^3P_{0,1})$, $L_2M_1M_{2,3}(^1P_1)$,

$L_3M_1M_{2,3}(^1P_1)$, L_2 M_1 $M_1(^1S_0)$ and L_3 M_1 $M_1(^1S_0)$. Figure 4.19 shows the good agreement between the energies of these normal Cl LMM Auger peaks and the ^{37}Cl LMM Auger spectrum except the extra LMM^H peak.

The explanation of the LMM^H peak requires a detailed understanding of this many-body relaxation process. A hypothesis is given in the following paragraphs regarding this mystery peak. The area under the LMM^H peak is about 12±3% of the total LMM Auger of ^{37}Cl. Another interesting characteristic of the LMM^H peak is the sharpness of the peak (~5 eV FWHM). As discussed earlier, normal Auger peaks are broadened by the interactions of the two holes in the final states through different coupling of the spin and orbital momentum. For normal Cl LMM Augers, the S-L splitting can be as wide as 5 eV. Transitions from different initial states in L_2 and L_3 can also have different Auger energies and further broaden the LMM Auger peak. The total FWHM of the LMM Auger peak in Fig. 4.19 is in the order of 20 eV. Therefore, the sharpness of LMM^H Auger peak might indicate that there is no hole-hole interaction in its final state.

One way to achieve a non-interactive final state is to have only one electron left in the M_{23} subshell after the LMM Auger transition. This final state must lose five of the valence electrons in the M_{23} subshell in the Auger cascades. Figure 4.20 illustrates such an Auger cascade channel. The K-hole first decays by a KL_1L_{23} Auger transition, which happens 22% of the time. The L_1 hole then decays by a Coster-Konig Auger transition

$L_1L_{2,3}M_{2,3}$, which happens about 46% of the time. The two $L_{2,3}$ holes then decay through $L_{2,3}M_{2,3}M_{2,3}$ and four more electrons are emitted. Five electrons are lost this way and the last $L_{2,3}M_{2,3}M_{2,3}$ Auger transition has a non-interactive final state. The Auger decay probability of this combination is about 8% of all the LMM Auger transitions. This is somewhat lower than the 12±3 % area under the LMM^H peak. The energy shift is also believed to be the result of the core level shifts due to the multiple ionization by this particular Auger cascade.

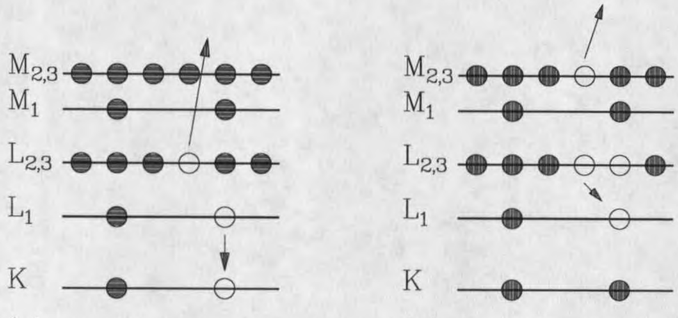

Figure 4.20 (a)-(d) Auger cascade for the hypothesis explaining the LMM^H peak.

The reason the LMM^H peak would not have been observed in the LMM Auger spectra produced by electron bombardment is that the initial states created by electron excitation are mostly L-holes. As mentioned above, the ratio of L to K shell holes created by a 5 keV electron beam bombardment is $S_L/S_K = 120$. Therefore the LMM^H peak in such experiment would be 120/12% =1000 times smaller than the normal LMM peak and would be effectively buried in the background.

Double Auger Decay of a ^{37}Cl Atom

The deep K-shell hole created by the EC process in the ^{37}Cl atom can sometimes decay through another Auger process where the energy released by filling the K-hole electron is shared by two ejecting electrons simultaneously. This is called a double Auger decay process.[4,40-42] As discussed in Chapter 2, the double Auger decay process is caused by three electron-electron correlation effects:[4] the virtual inelastic scattering effect where an outgoing normal Auger electron in an intermediate state is inelastically scattered by another electron; the cascade mechanism where the initial K-hole decays through a normal Auger transition, producing a vacancy in one of the intermediate shell and then decaying via another Auger transition; the shake-off model where the initial K-hole decays through normal Auger decay, then the atomic field caused by this Auger transition shakes off another electron. In each of these models, the probability of the double Auger decay process is the product of the probabilities of each step in the process. The energy distribution between the two outgoing electrons is expected to be highly asymmetric due to the first and third mechanism. This section is devoted to the study of the double Auger decay probability and the energy distribution between the two double Auger electrons.

^{37}Cl Double Auger Probability

In most double Auger processes, the two emitted electrons will share the energy provided by the filling of a K hole by an L electron. These two electrons would have continuous energy spectra instead of discrete Auger lines as in normal Auger spectroscopy. The probability of the double Auger process cannot be very large because it is a second-order process. Therefore, in conventional Auger spectroscopy, these two double Auger electrons would be buried in the huge background of secondary electrons, and hence essentially impossible to measure directly. A breakthrough in the study of the double Auger process has been achieved in this work by using the coincidence techniques to measure the time correlation between the two electrons emitted by the process. The two double Auger electrons are always emitted simultaneously and always share a fixed total kinetic energy, E_{MAX} = 2200 eV (E_K -3E_L). Their correlation in time and energy makes them ideal candidates for the coincidence measurements.

After an EC process, a K-shell hole will relax mostly by the Auger cascades of the KLL and LMM Auger transitions. In a normal Auger decay, a KLL Auger electron whose energy is about 2400 eV is always in coincidence with the cascading LMM Auger electrons whose energies are about 170 eV. Therefore, two MCP detectors will always register coincidence counts if one of the retarding screen voltages is set below 170 V (Fig. 4.12 and Fig. 4.21). However, if the retarding voltages at both detectors are set above the LMM Auger energy (*e.g.,* at 250 V), no electron-electron coincidence should be registered from a normal Auger process. Therefore, the recording of the coincidence events between two electrons having energy above the LMM Auger energy in this work provides the first *direct* evidence of the double Auger decay process (as discussed early, the coincidence contribution between x-ray and KLL Auger electron is essentially zero).

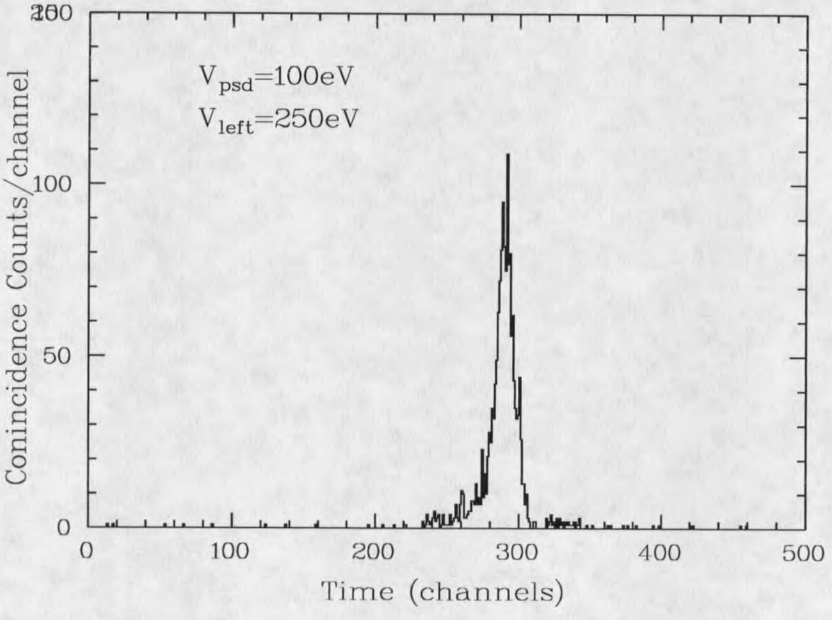

Figure 4.21 Coincidence spectrum of KLL Auger and LLM Auger electrons taken with MCP screen voltages at 250V and 100V.

Figure 4.22 shows two electrons having kinetic energy more than 250 eV in coincidence with each other. This is the first direct evidence of the double Auger decay process. The measurement was taken with 10 L radioactive ^{37}Ar source made from

^{40}Ca(n,α)^{37}Ar reaction and deposited on the graphite substrate for about 5 hours. The two MCP detectors (L and PSD) were biased for electron detection and their single counts were also recorded simultaneously. The distances from both detectors to the sample were 6 cm. The shortest time in the coincidence peak (left edge) was due to the coincidence starting by a 250 eV slow electron and stopping by a 1950 eV fast electron (2200 eV-250 eV), whereas the longest time in the coincidence peak (right edge) was due to starting by the fast electron and stopping by the slow one. The calculated time difference between the left and right edge should be 7.35 ns. This time difference corresponding to about 70 channels is in good agreement with the coincidence peak as shown in Fig. 4.22.

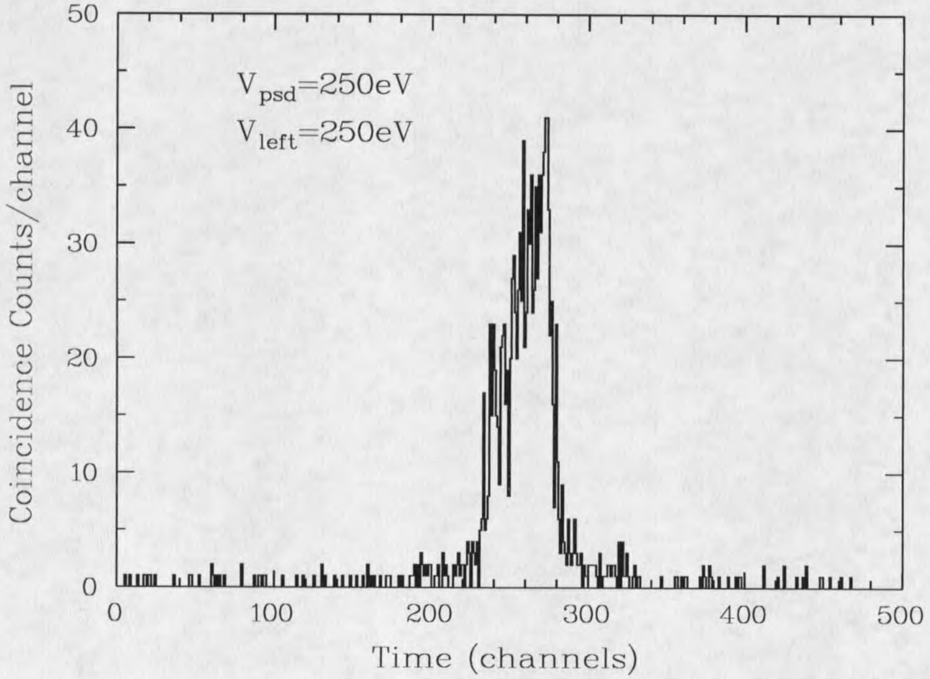

Figure 4.22 Coincidence spectrum of two electrons emitted in the double Auger process.

The probability of the double Auger decay was measured by two independent experiments both utilizing coincidence techniques. The first experiment measured the coincidence counts, N_{DA}, *i.e,* the area under the coincidence peak in Fig. 4.22, the coincidence counts, N_{KL}, *i.e.,* the area under the coincidence peak in Fig. 4.21 and their single counts of the KLL Auger electrons, $N_{K(DA)}$ and $N_{K(KL)}$ which were simultaneously recorded. The N_K and N_{KL} have been expressed in Eq. (4.2) and Eq. (4.6) and are listed here as Eq. (4.7) and Eq. (4.8)

$$N_K = N_0\, P_k\, (1-w)\, f_{K>250}\, (\Delta\Omega/4\pi)\, T_K\, \varepsilon_K\, \eta_K\, f_{live} \tag{4.7}$$

$$N_{KL} = N_0\, P_k\, (1-w)\, [\, 2 f_{KLL} + f_{KLM}\,]\, f_{K>250}\, f_{L>100}\, (\Delta\Omega/4\pi)^2\, T_K\, T_L\, \varepsilon_K\, \varepsilon_L\, \eta_K\, \eta_L\, f_{live} \tag{4.8}$$

where all the parameters has been explained following Eq. (4.5). The N_{DA} have the form

$$N_{DA} = N_0\, P_k\, (1-w)\, P_{DA}\, f_{E1>250} f_{E2>250}\, (\Delta\Omega/4\pi)^2\, T_{E1}\, T_{E2}\, \varepsilon_{E1}\, \varepsilon_{E2}\, \eta_{E1}\, \eta_{E2}\, f_{live} \tag{4.9}$$

where E_1 and E_2 stand for the energies of the two double Auger electrons ($E_1 < E_2$). The factors $f_{E1>250} f_{E2>250} < 1$ are the portion of double Auger decays with both double Auger electrons having more than 250 eV kinetic energy. This factor takes into account the effects of intrinsic energy distribution and the slowing down of electrons on the way out by inelastic scattering. The energy-dependent electronics system efficiency ε and escape probability η are taken here with their average values because E_1 and E_2 are not fixed energies any more, unlike the case in KLL and LMM Auger. From Eq. (4.7) and Eq. (4.8) one can get

$$N_{KLL} / N_{K(KL)} = (2 f_{KLL} + f_{KLM}) f_{L>100} (\Delta\Omega/4\pi)\, T_L\, \varepsilon_L\, \eta_L \tag{4.10}$$

From Eq. (4.8) and Eq. (4.9) one can get

$$N_{DA} / N_{K(DA)} = P_{DA} \, (f_{E1>250} f_{E2>250} / f_{K>250}) \, (\Delta\Omega/4\pi) \, T_{E1} \, \varepsilon_{E1} \, \eta_{E1} \tag{4.11}$$

where the parameters associated with higher energy electrons are assumed to be equal, *i.e.*, $T_{E2} \sim T_K$, $\varepsilon_{E2} \sim \varepsilon_K$ and $\eta_{E2} \sim \eta_K$.. Dividing Eq.(4.11) by Eq. (4.10), one can get

$$R \equiv \frac{\left(N_{DA} \Big/ N_{K(DA)} \right)}{\left(N_{KL} \Big/ N_{K(KL)} \right)} = P_{DA} \left(\frac{f_{E1>250} f_{E2>250}}{f_{L>100} f_{K>250}} \right) \left(\frac{\varepsilon_{E1} \eta_{E1}}{\varepsilon_L \eta_L} \right) (2 f_{KLL} + f_{LMM}) \tag{4.12}$$

where $2f_{KLL} + f_{LMM} = 1.84$ is the average number of LMM Auger electrons following a K-hole that has decayed by KLL or KLM Auger transitions. In general, the electronics response factor ε and the escape probability η are larger if electron energy is higher. For this measurement, $E_1 \geq 250$ eV $> E_L$, and therefore $\varepsilon_{E1} \geq \varepsilon_L$ and $\eta_{E1} \geq \eta_L$. However, each pair of these parameters are not far away from each other. It is also known that $f_{L>100} f_{K>250} < 1$ and $f_{K>250} \approx 1$. Now defining the probability, P'_{DA} as the probability of the measured portion of double Auger decay ($E_1 \geq 250$ eV and $E_2 \geq 250$):

$$P'_{DA} = (f_{E1>250} f_{E2>250}) \, P_{DA} \, . \tag{4.13}$$

Then the upper limit of P'_{DA} can be calculated as

$$P'_{DA} \leq R/1.84 \tag{4.14}$$

The data used to calculate P'_{DA} were obtained from N_{DA} ,$N_{K(DA)}$, N_{KL}, and $N_{K(KL)}$. They were measured as close together in time as possible to ensure that similar radioactive source and electronics conditions were maintained invariant during the experiment. Substituting the data from Fig. 4.21 and Fig. 4.22, one can calculate the upper limit of the double Auger decay probability to be 16.1±0.6%. Two other measurements with similar conditions yield upper limits results as 15.4±0.7% and 11.9±0.6%. The weighted average result for the upper limit of double Auger decay probability is 14.9±0.4%

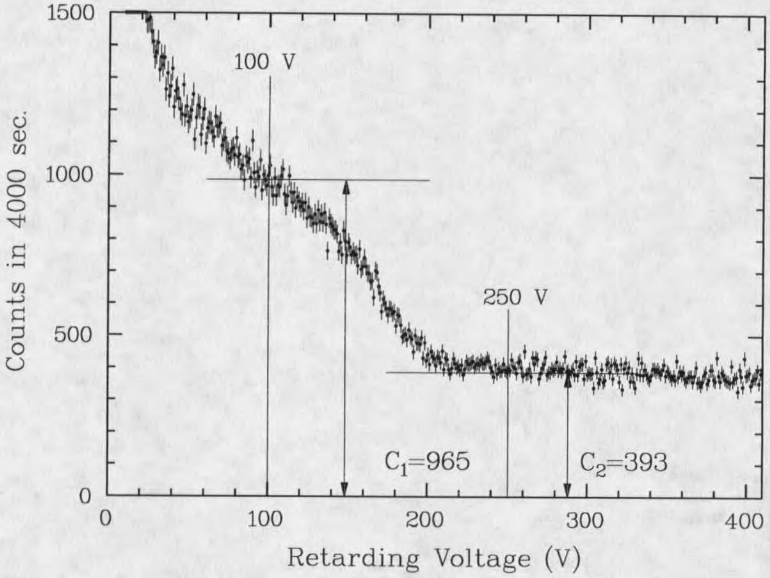

Fig. 4.23 RFE spectrum of ^{37}Cl LMM Auger. The counts C_2 were from KLL Augers while counts C_1 were the contribution from both KLL and LMM Augers.

The lower limit of the double Auger decay probability can be obtained by combining the discussion above with the retarding field energy (RFE) spectrum of the ^{37}Cl LMM Auger. Figure 4.23 shows a RFE spectrum taken with the same MCP detector under the same experimental conditions as the coincidence measurement. The counts C_2 at 250 V retarding voltage were from KLL Auger electrons while the counts C_1 at 100 V were the contribution from both KLL and LMM Auger electrons. They have the forms

$$C_1 = N_0\, P_k\, (1-w)\, (\Delta\Omega/4\pi)\, T\, f_{live}\, [\, f_{K>100}\, \varepsilon_K\, \eta_K + (2f_{KLL} + f_{KLM})\, f_{L>100} \varepsilon_L\, \eta_L] \quad (4.15)$$

$$C_2 = N_0 P_k (1-w) (\Delta\Omega/4\pi) T f_{live} f_{K>250}\, \varepsilon_K\, \eta_K \qquad (4.16)$$

Their ratio, $R' = C_1 / C_2$ will be

$$R' = f_{K>100}/f_{K>250} + (2f_{KLL} + f_{KLM})\, (f_{L>100}\varepsilon_L\, \eta_L / f_{K>250}\, \varepsilon_K\, \eta_K) \qquad (4.17)$$

where $f_{K>100} \approx f_{K>250}$ and $2f_{KLL} + f_{KLM} = 1.84$. From Fig. 4.23, the counts $C_1 = 965$ and $C_2 = 393$, therefore

$$R' = 1 + 1.84\, (f_{L>100}\varepsilon_L\, \eta_L / f_{K>250}\, \varepsilon_K\, \eta_K) = 2.46 \qquad (4.18)$$

This gives

$$(f_{L>100}\varepsilon_L\, \eta_L / f_{K>250}\, \varepsilon_K\, \eta_K) = 0.8 \qquad (4.19)$$

From Eq.(4.19) one can get

$$1.25 = (f_{K>250}\, \varepsilon_K\, \eta_K / f_{L>100}\varepsilon_L\, \eta_L) > (1/f_{K>100})\, (\varepsilon_{E1}\, \eta_{E2} / f_{L>100}\varepsilon_L\, \eta_L) \qquad (4.20)$$

Comparing Eq. (4.20) and Eq. (4.12), one can then get

$$P'_{DA} = (f_{E1>250} f_{E2>250})\, P_{DA} = \frac{R/1.84}{\left(\dfrac{1}{f_{L>100}}\right)\left(\dfrac{\varepsilon_{E_1}\eta_{E_1}}{\varepsilon_L \eta_L}\right)} > \frac{R}{1.84} 0.8 \qquad (4.21)$$

This gives

$$0.8\, R/1.84 \le P'_{DA} \le R/1.84 \qquad (4.22)$$

Substitute the results as when calculating the upper limit, one can calculate the lower limit of the double Auger decay probability to be 11.9±0.3%.

The second experiment designed to measure the double Auger probability used a indirect approach. As shown in Fig. 4.21, if one of the MCP screen voltages is higher than 250 V and the other is lower than 170 V, a coincidence peak from KLL and LMM

Auger electrons can be registered. If the high and low retarding screen voltages are switched, the coincidence peak would be centered at a different channel (time). Now imagine reducing both screen voltages below 170 V then one would expect to see three coincidence peaks appearing on the spectrum: the KLL starting and LMM stopping coincidence peak on the right (late time); the LMM starting and KLL stopping coincidence peak on the left (early time) and the LMM starting and LMM stopping coincidence in the middle. If the double Auger process happens, the triple vacancies left in the L-shell by this process would largely enhance the LMM Auger transitions, and thus increase the middle peak. Therefore, the size of the middle peak compared to the left or right peak size could yield some information about the double Auger decay probability.

Figure 4.24 shows coincidence spectra taken with different MCP detector screen voltages. The upper one (Fig. 4.24(a)) was taken with the starting (MCP detector) screen voltage set at 250 V and the stopping screen voltage set at 100 V, with the coincidence peak centered to the right (late time). The lower one (Fig. 4.24(c)) was taken with the starting screen voltage set at 100 V and the stopping screen voltage set at 250 V, with the coincidence peak centered to the left (early time). The middle one (Fig. 4.24(b)) was taken with the starting and stopping screen voltages both set at 100 V, and the coincidence peak is centered at the middle. Part of the tails of Fig. 4.24(a) and Fig. 4.24(c) were extended to the middle range below the center peak. The background of the center peak in Fig 4.24(b) was calculated by scaling these tails. The contribution of the right peak to the center background was calculated by taking the area ratio between the right peak and its tail in the center region in Fig 4.24(a) and multiply the inverse of this ratio to the right peak area in Fig 4.24(b). The contribution of the left peak to the central background was obtained in the same way. The background was then subtracted from the center peak in Fig. 4.24(b) to get the net area of the peak. The resulting net areas of the left peak, A_{L-K} and the center peak, A_{L-L} in Fig 4.24(b) are 1653 and 993, respectively.

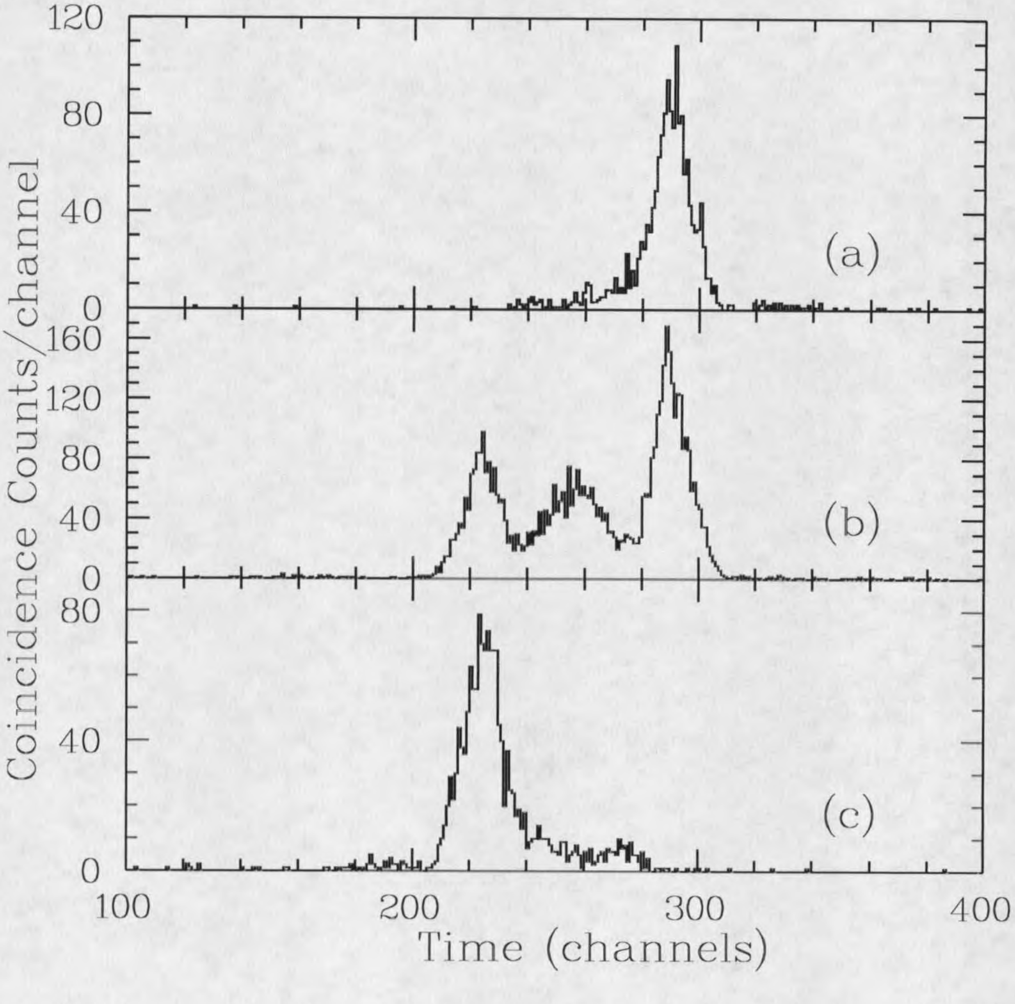

Figure 4.24 Coincidence spectra with different MCP detector screen voltages. (a)KLL(start) /LMM(stop), (b)LMM/LMM and (c) LMM/KLL.

This gives the ratio $R_{EXP} = (A_{L\text{-}K}/A_{L\text{-}L}) = 1.66$ which contains the contribution from double Auger process. On the other hand, each Auger electron emitted by filling a K-hole (KLL or KLM) will be followed by $2f_{KLL} + f_{KLM} = 1.84$ LMM electrons and each LMM electron can only find 1.84 -1 = 0.84 LMM electrons to be in coincidence with. If a double Auger decay happens, the filling of the three extra L vacancies left by the double Auger process will create three more LMM Auger electrons. The slower of the double Auger electrons will also contribute the same as an LMM Auger electron. These four electrons would have six different combinations of coincidence to contribute to the center peak but only four ways to contribute to the left peak. Assuming the double Auger decay probability to be P_{DA},, the contribution of the double Auger process to the center peak would be 6xP_{DA}, whereas the contribution to the left peak would be 4xP_{DA}. Therefore the double Auger decay probability can be calculated as

$$R_{EXP}=\frac{1.84+4P_{DA}}{0.84+6P_{DA}}=1.66 \tag{4.23}$$

This gives a result $P_{DA} = 8\pm3\%$ which is somewhat lower but still comparable to the results from the other independent experiments which set the double Auger decay probability to be between 12% to 15%.

^{37}Cl Double Auger Energy Distribution

The energy distribution between the two emitted electrons is expected to be highly asymmetric because of the virtual inelastic scattering and shake-off mechanisms in the double Auger process.[4] However, the energy has to be conserved during the process. This means the total kinetic energy, E_{TOT} of the two emitted electrons must be equal to the energy released by the initial transition from L-shell to the K-hole

$$E_{TOT} = (E_K - E_L) - 2E_L \tag{4.24}$$

The last term in Eq. (4.24) is the energy required for two L shell electrons to escape above the vacuum level. Substituting the energy level values from Table 2.1, one can get the

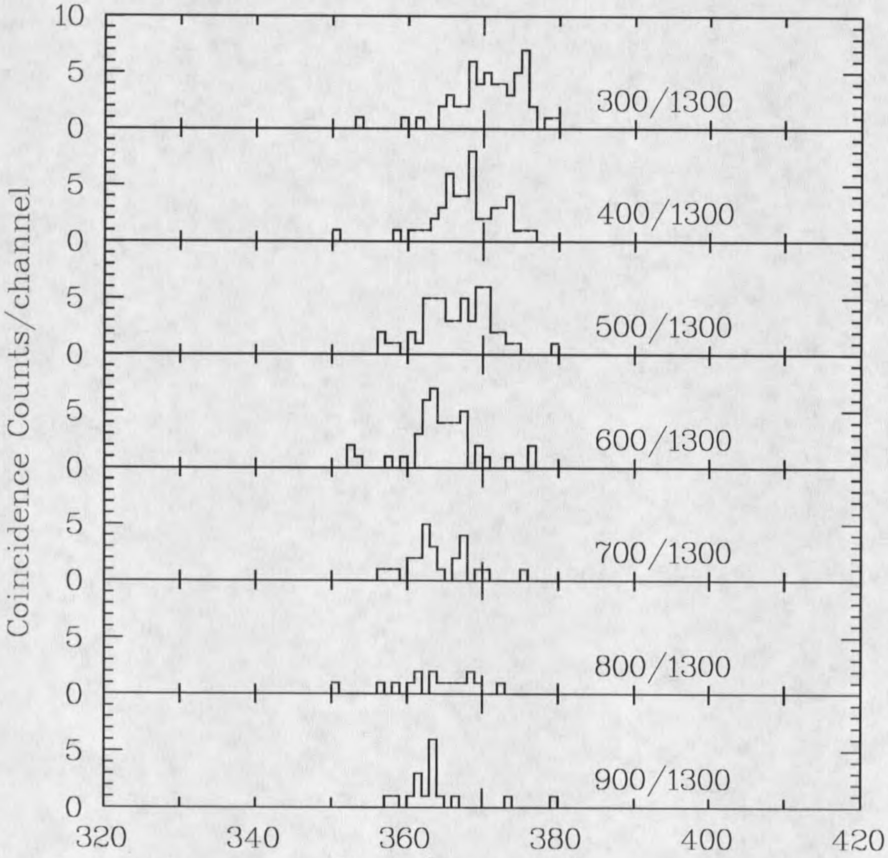

Figure 4.25 Coincidence spectra with different MCP screen voltages as indicated by the numbers to the left of the peaks.

total kinetic energy of the two emitted electrons, $E_{TOT} \approx 2200$ eV if most transitions involve the $L_{2,3}$ level. Due to this energy correlation, the kinetic energies of the two emitted electrons are no longer independent, *e.g.,* limiting one of them to be greater than 250 eV would also restrict the other one to be less than 1950 eV. Therefore, the electronics would register coincidence contributions from double Auger pairs with different combination sharing the total 2200 eV energy if different retarding screen voltages are applied in the coincidence measurements. This provides a possible way to map the energy dependence of the double Auger probability by scanning the retarding screen voltage.

In the actual experiment, the kinetic energy of one of the electrons was kept above 1300 eV by the retarding voltage of the MCP detector and the other one was changed from 200 eV to 1300 eV in 100 eV step. This way the faster one of the two double Auger electrons would always enter the high biased detector, thus simplifying the measured coincidence spectra. The experiments were conducted by using 6L of $^{36/37}$Ar source on the Au/Si(111) and 10L ^{37}Ar source from ^{40}Ca(n,α)^{37}Ar reaction on the graphite substrate. Figure 4.25 shows the coincidence spectra with different MCP screen voltages taken for 20 hours each with 6L $^{36/37}$Ar source on the Au substrate. The single counts on both MCP detectors were recorded simultaneously to provide the normalization reference.

Figure 4.26 shows the measured energy dependence of the probability distribution for one of the two electrons emitted in the double Auger process. This is the first time such measurement has been performed. The probability was measured by simply following the areas under the coincidence peaks like the ones in Fig. 4.25 as a function of the kinetic energy of one of the two electrons, as determined by the MCP screen voltages. Each area was normalized by its single counts The kinetic energy of the other electron was kept above 1300 eV by placing a retarding screen voltage of 1300 V. Note that the spectrum in Fig 4.26 is an *integrated* spectrum. For example, all the double Auger electron pairs with one of the pair having kinetic energy from 400 eV to 1000 eV and the

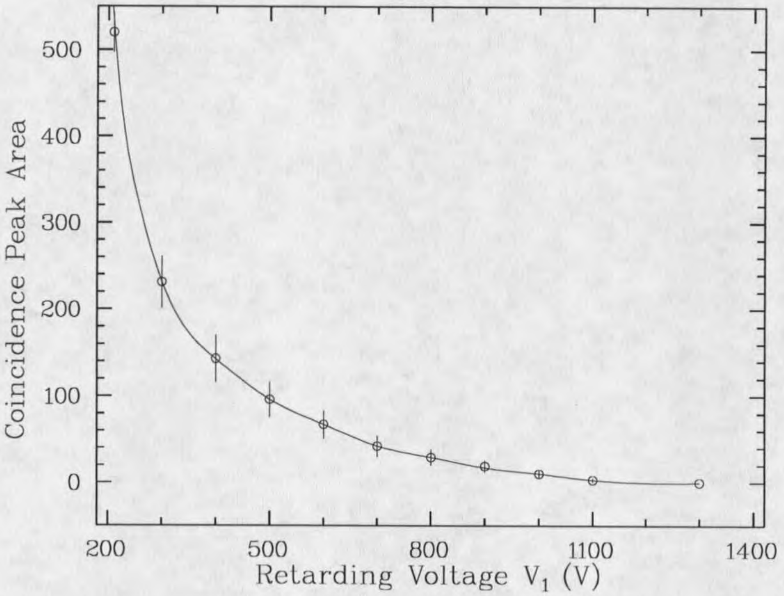

Figure 4.26 Double Auger probability as the function of one of the electron energies.

other one from 1200 eV to 1800 eV will contribute to the double Auger coincidence yield at the 400 V point in the x-axis The energy distribution, dN/dE is obtained by taking a derivative of the curve in Fig. 4.26 with respect to the retarding voltage, V. Figure 4.27 shows the resulting ^{37}Cl double Auger decay energy distribution superimposed with the theoretical results of the energy distribution of the atomic Ne double Auger decay.[4] Notice that there is qualitative agreement between the experimental result in this work and the theoretical predictions (the 2 Ry to 25 Ry part of the Ne spectrum is shown for comparison). The preferred energy distribution of the double Auger emission is for one of the electrons to take most of the energy with the second one receiving the small remaining balance. This is due to the first and third double Auger mechanisms discussed above.

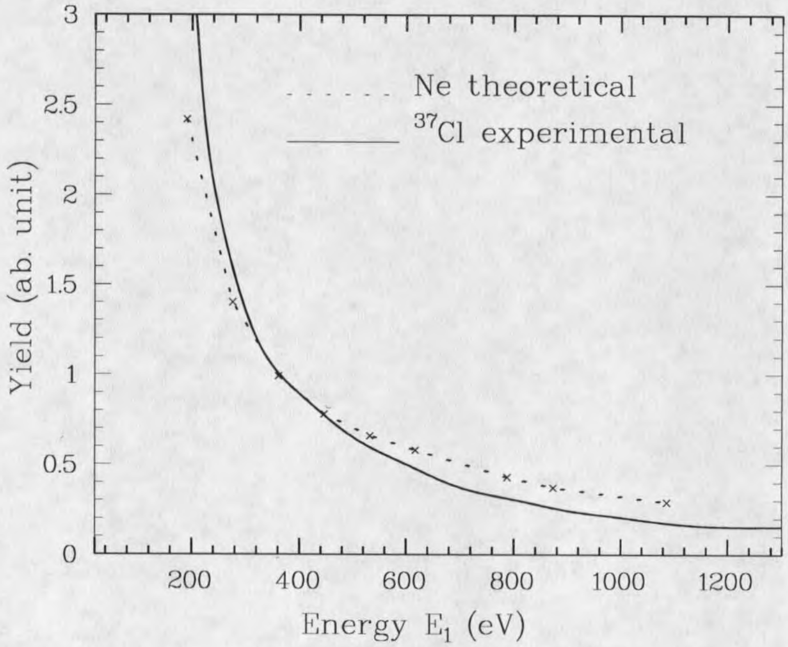

Figure 4.27 double Auger energy distributions by this experiment (solid line) and theoretical calculation for a Ne atom with 5 Ry to 25 Ry kinetic energies.

In the experiment with the new ^{40}Ca(n,α)^{37}Ar source on the graphite substrate, the *absolute* double Auger decay probabilities vs. retarding voltages were measured. One of the retarding voltage was set at 1100 V and the other was scanned from 250 V to 1100 V. Figure 4.28 shows the measured absolute double Auger probabilities. Each data point, (*X,Y*) in Fig. 4.28 stands for the contribution to the integrated double Auger probability (Y) from the double Auger electron pairs with one of them having kinetic energy from X eV to 1100 eV and the other 1100 eV to (2200 - X) eV. The coincidence counts at different retarding voltages were converted to the double Auger probabilities (%) by using the same calculations as in last section. It shows the double Auger probability for 250 V/1100 V screen voltages is 6±0.3 % and thus the 250 V/250 V screen voltages should be 12±0.6%, which is in good agreement with the value achieved before.

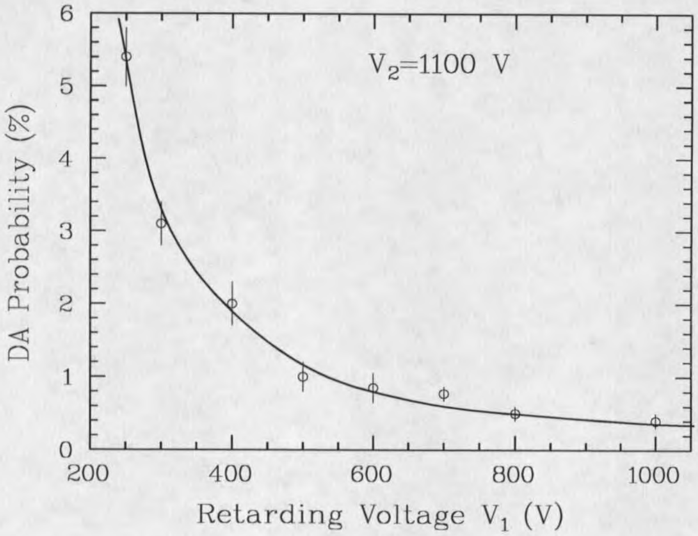

Figure 4.28 double Auger probability as the function of electron energy of one of the two emitted electrons. One of the screen voltage was always set at 1100V.

Discussion of ^{37}Cl Double Auger Decay Results

To back up the claim that this work observed directly for the first time the double Auger decay process, it is appropriate to have several different experiments to confirm the observation independently. In this section, another positive evidence of the double Auger decay process will be discussed. Other topics discussed here include the factors which will affect the measurement of the probability and energy distribution of the double Auger decay, especially the scattering effects of the multiple layers of gases to the outgoing double Auger electrons.

The first direct double Auger evidence provided in this work is the recording of true coincidence counts between two electrons above LMM Auger energy of Cl atom. These coincidence counts were attributed to the emission of two double Auger electron sharing the total energy released by filling the initial K-hole by an L-electron. The excess coincidence counts between LMM and LMM Auger electrons in Fig. 4.24(b) provided more evidence of the double Auger decay process. If the double Auger decay process exists, the filling of the K-shell by an L-electron and the emission of two electrons from L-shell in the double Auger process would have left three L-shell vacancies simultaneously. This intermediate configuration could not be achieved by any other transition except the double Auger decay process. The decay of this particular intermediate state would result in the emission of *three* LMM electrons simultaneously.

Therefore, the third direct evidence of the double Auger decay would be the recording of the triple coincidence of these LMM Auger electrons in a new experiment.

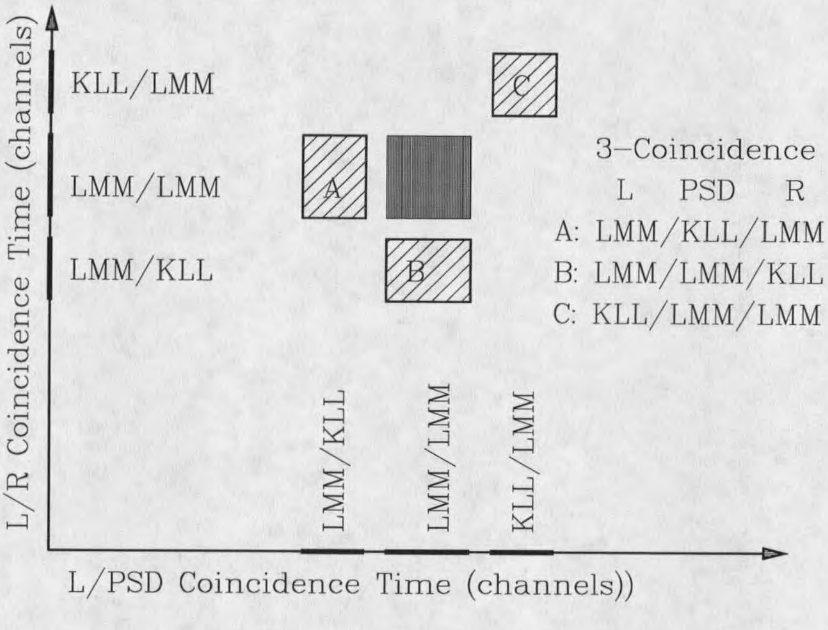

Figure 4.29 Schematic diagram of a triple coincidence spectrum. The solid region is where a LMM/LMM/LMM coincidence appears.

The experimental logic diagram has been shown in Fig. 3.16. A multiple layer of active $^{40}Ca(n,\alpha)^{37}Ar$ source was deposited on the cold graphite substrate. Three MCP detectors were biased with retarding screen voltages all set at 100 V. The coincidence between left (L) and middle (PSD) detectors and the coincidence between L and right (R) detectors were recorded simultaneously on the magnetic tape. The triple coincidence results would be then extracted by replaying the magnetic tape and plotting the data on a two dimensional diagram with the coincidence L and PSD as x-axis and L and R as y-axis. The experimental results are shown schematically in Fig. 4.29. Most of the coincidence counts were the double coincidences (L/PSD or L/R) which stay on the x or y axis. It means that when a double coincidence was registered, there was no coincidence between one of the two registered MCP signals from this double Auger with the third MCP signal. A point off the axis, however, represents three MCP signals arriving within a very short time interval, *i.e.*, a triple coincidence. Most of the triple coincidence counts were expected to be KLL/LMM/LMM coincidences come from a regular KLL and LMM Auger cascade. These coincidence counts are shown in the shadowed regions in Fig. 4.28. The fact that there are six counts in the middle (solid) region which are above the accidental background (near zero) provides an evidence of a triple LMM/LMM/LMM coincidence, and hence the third direct evidence of the double Auger decay process.

The techniques employed in this work to measure the double Auger probability were not as universal as one would like. Because the double Auger decay process depends strongly on the energy partitioning between the two double Auger electrons and on their relative angle, it is difficult to obtain the probability of this process relative to the normal Auger process from a measurement conducted over a limited energy range and at one relative angle. The preferred energy configuration of a double Auger emission is for one of the electrons to take most of the energy with the second one receiving the small remaining balance. The energy selected by the retarding voltage in this measurement could not be lower than 200 eV, otherwise the KLL and LMM Augers would contribute the coincidence counts. Therefore, those double Auger electron pairs with one of them having energy less than 200 eV and the other greater than 2000 eV would not be measured by this measurement. This would affect the upper limit of the double Auger decay measured in this experiment. The angular correlation between the two electrons is predicted to be peaked in the forward direction for the preferred configuration and in the backward direction when energies are close to each other. In the present experimental setup, the MCP detectors were 45° from each other which is at the middle range of the curve of probability vs. angular separation predicted by theory.[4] The position sensitive detector (PSD) in this experimental setup did not have the necessary range of angle yet to measure the angular distribution of the double Auger process. Such a measurement is definitely needed in order to calibrate the double Auger decay probability result. Further experiments will apply a moveable detector or a PSD detector whose angular separation is large enough to sense the angular effect.

The last point to discuss in this section is the effects of the scattering of the double Auger electrons escaping the substrates. This attenuation effect was clearly visible in Fig. 4.24(b) where the left coincidence peak was smaller than the right coincidence peak. The left peak was caused by a fast (KLL) electron to stop at the middle (0°) PSD detector and a slow electron (LMM) to start at the 45° left detector. Since the attenuation effect was much more severe for a slow electron than for a fast electron, the actual effect was determined by how many layers of adsorbed gases the slow electrons have to penetrate before leaving the surface. In the left coincidence peak, the slow electrons had to reach the 45° left detector, and hence had to penetrate ~1.5 times as many layers of gases, whereas in the right peak the slow electron only needed to reach the 0° middle detector. The ratio of these two peaks can serve as a good reference of the attenuation effects denoted as η in the probability calculation equations (*e.g.*, Eq. 4.14).

Besides the attenuation, another influence of the scattering effect is the slowing down of an outgoing double Auger electron. This would alter the measured spectra of the double Auger energy distribution. To study this effect, it is helpful to revisit the coincidence peak in Fig. 4.22 which was taken with both MCP screen voltages set at 250V. As discussed above, this coincidence peak contained the contributions from double Auger electron pairs having kinetic energies from 250 eV to 1950 eV for one electron and 1950 eV to 250 eV for the other electron. Each energy combination will be registered at a different channel (time) in the coincidence spectrum. Therefore, the whole energy distribution information could be extracted from the Fig. 4.22 alone if the time resolution was adequate. Unfortunately, this is not the case because the time separation corresponding to a fixed energy difference changes when energy changes. It is much easier to tell two electrons with 100 eV and 200 eV kinetic energy than two with 2100 eV and 2200 eV. The time resolution was not good enough for fast electrons.

A simple Monte Carlo simulation was conducted to study the effects of the scattering (Fig. 4.30). The double Auger electron pairs in coincidence were generated according the energy distribution predicted by the theoretical work on Ne atom.[4] The kinetic energy was scaled from 5 - 25 Ry to 200 - 1100 eV. The probability of generating

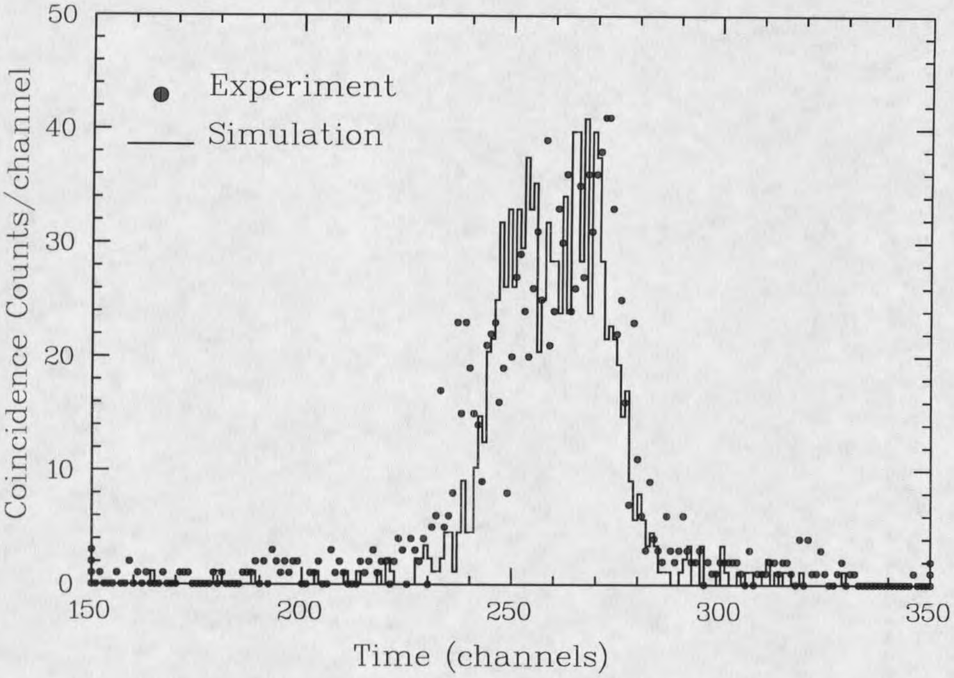

Figure 4.30 Comparison between the experiment result and simulations on double Auger coincidence spectrum.

a double Auger electron with energy E was proportional to the corresponding double Auger yield, $\gamma(E)$ as shown in Fig. 2.10. Each electron generated was allowed to keep its original energy 80% of the time and the remaining 20% of the time to have a flat energy distribution (due to scattering) from this energy to the minimum detectable energy determined by the screen voltage. The other member of the double Auger electron pair is generated in the same way with a kinetic energy 2200 eV -E (E_{tot} = 2200 eV). Furthermore, generating a random point on the source region of the substrate for the pair of double Auger electrons and allowing them to reach at random points on the two MCP detectors, the time-of-flight would then be calculated from the known energies and calculated distances. A total number of one thousand events were generated to compare with the thousand or so coincidence counts in Fig. 4.22. Good agreement was achieved by this simple simulation as shown in Fig. 4.30. Comparing Fig. 4.30 and Fig. 2.10, the scattering of the low energy electrons has totally distorted the energy distribution. To reduce this effect, higher concentrated radioactive ^{37}Ar sources are required in the future experiment to reach the same amount of activity with less coverage.

CHAPTER 5

CONCLUSIONS

Conclusions

The emphasis of this thesis report is on the results obtained in the fields of surface science and atomic physics rather than the study in the possible mass limit of neutrinos. The nuclear reaction of ^{37}Ar electron capture decay and the following relaxation of the core holes created by the electron capture process have provided exciting opportunities to study some novel physics phenomena which previously have been amenable only to theoretical calculations but impossible to probe experimentally. The study on the desorption of ^{37}Cl ions due to recoil induced by neutrino emission and the study on ^{37}Cl atom Auger relaxation yielded several surprising results in this research work.

Using coincidence techniques, the desorption of ^{37}Cl ions from cold substrates due to recoil induced by neutrino emission in the ^{37}Ar electron capture decay was observed for the first time in this experiment. The kinetic energy distribution of the desorbing ^{37}Cl ions was accurately measured. The resulting energy distribution of ^{37}Cl ions ranges from 5 eV to 13 eV with a maximum at around 9 eV. The spread of this energy distribution (FWHM) is about 3 eV. The center of this energy distribution is close to the 9.54 eV calculated value while the spread of energy is much larger than the value for isolated ^{37}Ar atoms. The charge state distribution of the desorbing ^{37}Cl ions was also measured by using retarding field energy analyzers in addition to the coincidence measurements. The resulting charge state distribution is: 53% of the total ions have charge +e, 21% have charge +2e and 26% have charge +ne, where n ≥ 3. This charge distribution is, again, substantially different from that expected for isolated decay atoms. The ^{37}Cl ions desorption probability was also measured by the using of retarding fields energy analyzers and coincidence techniques. The resulting ^{37}Cl ion desorption probability is 9.6±1.2%. This gives an upper limit of neutral desorption probability of ~ 90 %. The recoil energies, the charge state distribution and the desorbing probability of the ^{37}Cl ions have been found to be greatly affected by the charge exchange and the following Coulomb repulsion between the ^{37}Cl ions and their surrounding atoms. This interaction dominates the broadening on the recoil energy spectrum, significantly alters the charge states of the desorbing ^{37}Cl ions, and is responsible for the large neutral desorption probability. Further experiments to reduce these effect will be discussed in the next section.

The Auger relaxation of the K-hole initial state created by the ^{37}Ar EC decay, especially the LMM Auger transitions, was studied by using coincidence techniques and conventional surface analysis techniques. The measured ^{37}Cl Auger peaks following the EC decay of ^{37}Ar were compared with the normal Cl Auger peaks obtained by conventional means. The ^{37}Cl LMM Auger transitions had most of the peaks with energies of the normal Cl LMM Augers and structures resembling normal Ar LMM Augers. An extra peak, the hypersatellite LMM^{H} peak with 20 eV higher energy than the normal Cl was observed for the first time in this work. It is hypothesized that it is the result of the unusual initial state created by the EC decay and a special multiple-hole final state in the Auger transitions. Further work to understand this LMM^{H} peak includes energy differentiated coincidence measurements between different Augers to identify the correlation of this strange peak.

The first direct evidence of ^{37}Cl double Auger decay process was reported in this research work. In a double Auger decay process, the filling of the initial K-hole created from the EC decay by an L-shell electron results in the emission of two Auger electrons simultaneously. Using the coincidence techniques, the probability of the double Auger decay and the energy distribution between the two double Auger electrons were measured. The experimental results in this work achieved good agreement with the theoretical predications.[4] The probability of double Auger decay measured in this work are from 12±0.3% to 15±0.4% of the normal LMM Auger process. The preferred energy distribution between the two double Auger electrons is one of them taking most of the available energy and the second one taking the small remaining balance. Further work in this respect includes the measuring of the angular correlation between the two double Auger electrons and using this correlation to adjust the total probability of the double Auger decay measured in this work.

Perspective on Neutrino Mass Limit Study

It is demonstrated in this work that the surface interactions and atomic relaxation processes greatly complicate the simple picture of the two-body problem on the recoil processes described at the beginning of Chapter 2. The broadening of the recoil energy spectrum due to these surface and atomic processes circumscribed the resulting mass limit measured by this experiment. However, this pioneering effort of combining nuclear physics and surface analysis techniques to attack one of the most fundamental problem in physics is still of great merit and, with certain optimism, promising from the results obtained in the past three years. The information reported in this thesis work may provide valuable assistant in further experiments to search for neutrino mass limits. In this section, the resulting limits on the neutrino mixture ratio on certain mass range will be reported. Finally, the perspective on how to improve these experiments will be addressed.

The information on a massive neutrino in the EC decay has been extracted from the time-of-flight spectrum of the desorbing ^{37}Cl ions. The detailed data processing procedures are presented in the Appendix A. Here only a brief description will be given. The physically relevant quantity one tries to measure here is the mixing ratio (%) between the massless neutrino and the massive neutrino in this EC reaction. To obtain this ratio, the coincidence peak in the time-of-flight spectrum in Fig. 4.3(a) is first fitted with a

Gaussian and a constant background. A flat region to the right of the peak representing slower recoil ions hence massive neutrino emission is then fitted with a Gaussian and a flat background with the centroid and width fixed. The area ratio between the fitted "second peak" and the main peak provides the information on the neutrino mixing ratio. It is found that this experiment does not have the sensitivity for neutrinos with mass below m_ν = 600 keV. For neutrino with mass $m_\nu \approx$ 600 keV, the measured upper limit of the mixing ratio is 2±0.4 %. This limit is twice as high as the results obtained by other means in this mass region (~ 1%).

To get better results on neutrino mass limit, *i.e.,* to obtain a lower mixing ratio limit and at a lower mass region, a narrower recoil peak with better statistics will be needed. This would require the reducing of the broadening effects in the energy spectrum of the desorbing ^{37}Cl ions in future experiments. In an EC decay process, the coincidence between the ^{37}Cl ions and the x-ray photons would select only the singly charged ^{37}Cl^{+1} ions with a negligible recoil due to photon and LMM Auger electron emission (3.5%). These ^{37}Cl^{+1} ions created by x-ray relaxation instead of the Auger relaxation of the initial K-hole would be less likely to exchange charges with their neighbors due to the restrictions of energy conservation. This would significantly reduce the charge exchanges and the following Coulomb repulsion interactions, and thereby reduce the dominant broadening effect. Several buffer layers of the stable ^{40}Ar will also be adsorbed before the active ^{37}Ar is dosed on the cold substrate to deduce the charge exchanges between the ^{37}Cl ions and the substrate or the residual gases per-adsorbed as the substrate being cooling down. Simulations have shown that with the broadening effects reduced, the recoil time-of-flight coincidence peak would be appropriate to extract information on the mixing ratio between the massless neutrino and the 200 keV massive neutrino to achieve a limit much better than the results obtained by other means.

REFERENCES

1. V. Barger, F. Halzen, M. Marshak and K. Olive, *Neutrino Masses and Neutrino Astrophysics* (Telemark IV, World Scientific, Ashland, Wisconsin, 1987).

2. H.V. Klapdor and B. Povh, *Neutrino Physics, Proceedings of an International Workshop Held in Heidelberg, October 20-22,1987* (Springer-Verlag, Berlin, 1988).

3. F. Boehm and P. Vogel, *Physics of Massive Neutrinos* (Cambridge University Press, London, 1992).

4. M.Ya. Amusia, I.S. Lee and V.A. Kilin, Phys. Rev. A **45**, 4576 (1992).

5. J.A. Miskel and M.L. Perlman, Phys. Rev. **94**, 1683 (1954).

6. I. Kelson, H. Dumont, B. Perraillon, D. Nir and A. Zidon, Phys. Lett. A **139**, 406 (1989); I. Kelson, J. Phys. D **20**, 1049 (1987).

7. E. Glikman, I. Kelson and N.V. Doan, J. Vac. Sci. Technol. A **9**, 2776 (1991).

8. C.M. Lederer and V.S. Shirley, *Table of Isotopes*, 7th ed., (Wiley, New York, 1978).

9. T.E. Madey and J.T. Yates, J. Vac. Sci. Technol. **8**, 525 (1971).

10. T.E. Madey and J.T. Yates, Surface Sci. **63**, 203 (1977)

11. M.L. Knotek, Rep. Prog. Phys., **77**, 1499 (1984)

12. T.E. Madey, D.E. Ramaker and R.Stockbauer, Ann. Rev. Phys. Chem. **35**, 215 (1984)

13. D.M. Yuang and A.D. Crowell, *Physical Adsorption of Gases* (Butter Worths, Washington, 1962)

14. S. Ross and J.P. Olivier, *On Physical Adsorption* (Interscience Publishers, New York, 1964)

15. J.G. Dash, *Films on Solid Surfaces* (Acadamic Press, New York, 1975).

16. O.G. Petersen, D.N. Batchelder and R.O. Simmons, Phys. Rev. **150**, 703 (1966).

17. P.J. Kuntz and J.J. Hogreve, J. Chem. Phys. **95**, 156 (1991).

18. G.A. Kimmel, Z.H. Levine and B.H. Cooper, Phys. Rev. B **43**, 9403 (1992).

19. E.E. Nikitin and D.V. Shalashilin, Soviet J. of Chem. Phys. **6** 1051 (1990).

20. M.J. Ashwin and D.P. Woodruff, Surface Sci. **244** 247 (1991)

21. L. Galdyszewski and G. Galdyszewski, Surface Sci. **247** 274 (1991).

22. A H. Snell and F. Pleasonton, Phys. Rev. **55**, 1396 (1955).

23. O. Kofoed-Hansen, Phys. Rev. **96**, 1045 (1954).

24. R.C.Weast, *HandBook of Chemistry and Physics* (CRC Press, Cleveland, 1976).

25. R. Franchy and D. Menzel, Phys. Rev. Lett. **43**, 865 (1979).

26. H.D. Hagstrum, Phys. Rev. **96**, 325 (1954).

27. R. Hentschke, P.Hertel and W. Heiland, Surface Sci. **173**, 565 (1986).

28. K.J. Snowdon, R. Hentschke, and W. Heiland, Surface Sci. **173**, 581 (1986).

29. L.O. Werme, T. Bergmark and K. Siegbahn, Physica Scripta **8**, 149 (1973)

30. G. Omar and Y. Hahn, Phys. Rev. A **43**, 4695 (1990)

31. G. Omar and Y. Hahn, Phys. Rev. A **44**, 483 (1991).

32. G. Omar and Y. Hahn, Z. Phys. D **25,** 31 (1992)

33. G. Omar and Y. Hahn, Z. Phys. D **25,** 41 (1992)

34. J.C. Levin, N.Keller and D.W. Lindle, Nuc. Ins. Met. in Phys. Res. B **56,** 124 (1991).

35. W.M. Ariyasinghe, H.T. Awuku and D. Powers, Phys. Rev. A **42**, 3819 (1990).

36. F. Xu and A. Bonanno, Surface Sci. **273,** 414 (1992).

37. J.A. de Gouw, J. van Eck, and H.G.M. Heideman, Jour. of Phys. **25**, 2007 (1992).

38. P. van der Meulen, M.O. Krouse and C.A. de Lange, Phys. Rev. A **46**, 2468 (1992).

39. J.G. McCaffrey, H. Kunz and N. Schwentner, Jour. of Chem. Phys. **96**, 155 (1992).

40. T.A. Carlson and M.O. Kraus, Phys. Rev. Lett. **14**, 390 (1965)

41. U. Becker, B.Langer and R.Wehlitz, Jour. Phys. B **22**, 749 (1989)

42. V.A. Kilin, I.S. Li and O.V. Li, Soviet Physics **36**, 146 (1991).

43. P. Moretto-Capelle and H.J. Andra, Z. Phys. D **21**, 347 (1991).

44. G.W. Rodeback and J.S. Allen, Phys. Rev. **86** 446 (1952).

45. R.A. Rubenstein and J.N. Snyder, Phys. Rev. **99**, 189 (1955).

46. W. Neumann, Phys. Rev. Lett. **42** 1514 (1979).

47. J.P.Renier, H. Genz, K.W.D. Ledingham and R.W.Fink, Phys. Rev. **166,** 935 (1968).

48. D. Menzel and R. Gomer, Jour. Chem. Phys. **41**, 3311 (1964).

49. P.A. Readhead, Can. Jour. Phys. **42**, 886 (1964).

50. M.L. Knotek and P.J. Feibelman, Phys. Rev. Lett. **40**, 946 (1978); Surf. Sci. **90**, 78 (1979).

51. P.Feulner, T.Mueller and D. Menzel, Phys. Rev. Lett. **59**, 791 (1987).

52. E.Steinacker and P.Feulner, Phys. Rev. B **40**, 11348 (1989).

53. G.Rocker, P.Feulner, L.Zhu and D.Menzel, Physica Scripta **41**, 1014 (1990)

54. R.Scheuerer, P.Feulner, L.Zhu and D.Menzel, *Desorption Induced by Electronic Transitions, DIET IV,* p 235, Edited by G.Betz and P.Varga (Springer Ser. Surface Sci. 19 Berlin, 1990).

55. D.Menzel, Appl. Phys. A **51**, 163 (1990).

56. Y.Baba, G. Dujardin and D. Menzel, Phys. Rev. Lett. **66**, 3269 (1991).

57. T. Schwabenthan, R.Scheuerer and P. Feulner, Solid State Commun. **80**, 773 (1991).

58. E.Hudel, E. Steinacker and P. Feulner, Phys. Rev. B **44**, 8972 (1991).

59. H.Schlichting and D.Menzel, Surface Sci. **272**, 27 (1992).

60. W.Wurth, G. Rocker, L.Zhu and D. Menzel, Phys. Rev. B **47**, 6697 (1993).

61. G.Ehrlich and F.G. Hudda, Jour. of Chem. Phys. **30**, 493 (1959).

62. T.Engel and R. Gomer, Jour. of Chem. Phys. **52**, 5572 (1970).

63. D.E. Sullivan, Phys. Rev. B **20**, 3991 (1979).

64. G.P. McTauge, J. Bohr and M. Nielsen, Phys. Rev. B **25**, 7765 (1982)

65. E.E. Johnson and M.Inokuti, Nucl. Instr. Meth. **206**, 289 (1982)

66. B.J. Garrison and R.E. Johnson, Surface Sci. **148**, 388 (1984).

67. R.E. walkup, P.Avouris and N.D. Lang, Phys. Rev. Lett. **63**, 1972 (1989).

68. D.Dujardin, L.Hellner and R.Azria, Phys. Rev. Lett. **64**, 1289 (1990).

69. D.Dujardin, L.Hellner and P. Cirkel, Phys. Rev. B **48**, 14529 (1993).

70. W. Bambynek, Rev. Mod. Phys. **44**, 716 (1972).

71. C.C. Chang, *Analytical Auger Electron Spectroscopy* (Plenum Press, New York, 1974).

72. T.A. Carlson, *Photoelectron and Auger Spectroscopy* (Plenum Press, New York, 1975).

73. L.E. Davis, G.E. Riach and R.E. Weber, *Handbook of Auger Electron Spectroscopy* (Physical Electronics Industries, Inc, Eden Prairie, MN,1976)

74. G.E. McGurie, *Auger Electron Spectroscopy Reference Manual* (Plenum Press, New York, 1979).

75. K.D. Sevier, *Low Energy Electron Spectroscopy* (Wiley-Interscience, New York 1972).

76. Chen, Craseman and Mark, *K- and L-Shell Radiationless Transition Probabilities*, Atomic Data and Nuclear Data Tables, **24**, 17 (1979).

77. R.R. Rye and J.E. Houston, Jour. Chem. Phys. **78**, 4321 (1983).

78. R.Platania and F. Maracci, Chem. phys. 163, 381 (1992).

79. D. Burch, L. Wilet and W.E. Meyerhof, Phys. Rev. A **9**, 1007 (1974).

80. T. Darko, H.Siegbhan and P. Kelfve, Chem. Phys. Lett. **81**, 475 (1981).

81. J.C. Levin, I.A. Sellin and D.W. Lidle, Phys. Rev. Lett. **65**, 988 (1990).

82. N. Vaeck and J.E. Hansen, Jour. of Phys. B **25**, 3613 (1992).

83. N. Saito and I.H. Suzuki, Physica Scripta **45**, 253 (1992).

84. L.M. Brown, *History of Physics* (American Institute of Physics, 1985)

85. E. Fermi, Ricercha Scient. **2**, 12 (1933)

86. E. Fermi, Z. Physik. **88**, 161 (1934)

87. M. Cardona and L. Ley, *Photoemission in Solid I* (Springer-Verlag, Berlin, 1978)

88. P.R. Antoniewicz, Phys. Rev. B **21**, 3881 (1980)

89. Q.J. Zhang and R.Gomer, Surface Sci. **109**, 567 (1981).

90. Q.J. Zhang, R.Gomer and D.R. Bowman, Surface Sci. **129**, 535 (1983).

91. R.B.Kay and M.J. van der Weil, Jour. Phys. B **10**, 2521 (1977)

92. M.Cini, Solid St. Comm. **20**, 605 (1976).

93. G.A. Sawatsky, Phys. Rev. Lett. **39**, 504 (1977).

94. D.E. Ramaker, Phys. Rev. B **21**, 4608 (1980).

95. D.R. Jennison and R.R. Ray, Phys. Rev. B **25**, 1384 (1982)

96. D.E. Ramaker, C.T. White and J.S. Murday, J. Vac. Sci. Technol. **18**, 748 (1981)

97. P.J. Feibelman, Surface Sci. **102**, L51 (1981)

98. M.L. Knotek, Nature **291**, 452 (1981).

99. D.R. Jennison, J. Vac. Sci. Technol. **20**, 548 (1982).

100. C.F. Melius, R.H. Stulen and J.O. Poell, Phys. Rev. Lett. **48**, 1429 (1982).

101. M.F. Chung and L.H. Jenkins, Surface Sci. **22**, 479 (1970)

102. G Wendin, *Breakdown of the One-Electron Pictures in Photoelectron Spectra* (Springer-Verlag, Berlin, 1981)

103. T.A. Carlson and M.O. Kraus, Phys. Rev. **151**, 41 (1966)

104. D.A. Church, Phys. Rev. A **36**, 2487 (1987)

105. H.W. Haak, G.A. Swatasky and T.D. Thomas, Phys. Rev. Lett. **41**, 1825 (1978);

106. H.W. Haak, G.A. Swatasky and T.D. Thomas, Rev. Sci. Instrum. **55**, 696 (1984)

107. E. Jensen, R. Bartynski, E. Johnson and R. Garret, Phys. Rev. Lett. **41**, 1825 (1989)

108. S.Thurgate, B. Todd and A. Stelbovics, Rev. Sci. Instrum. **61**, 3733 (1990)

109. E. Jost, Jour. Phys. E **12**, 1001 (1979)

110. Galileo Electro-Optics Co., *Electron Multiplier Handbook for Mass Spectrometry Applications* (1991).

111. Kurz, *Channel Electron Multipliers* (American Laboratory, March 1979)

112. M.Lampton and C.W. Carlson, Rev. Sci. Instrum. **50**, 1093 (1979)

113. R.S. Gao and R.F. Stebbings, Rev. Sci. Instrum. **55**, 1756 (1984)

114. W.G. McMullans and M.L.W. Thewalt, Rev. Sci. Instrum. **58**, 1626 (1987)

115. S.H. Courtney and W.L. Wilson, Rev. Sci. Instrum. **62**, 2100 (1991)

116. S. Charbonneau and B.J. Kyle, Rev. Sci. Instrum. **63**, 5315 (1992)

117. C.A. Murrar and S.B. Dierker, Jour. Opt. Soc. Am. A **3**, 2151 (1986)

118. Y. Talmi and C.W. Simpson, Appl. Opt. **13**, 1401 (1980)

119. D. Rees and S.J. Kellock, Jour. Phys. E **13**, 763 (1980)

120. I. McWhirter and D. Rees, Jour. Phys. E **15**, 745 (1982)

121. W.M. Augustyniak and H.P. Pie, IEEE Trans. Nucl. Sci. NS **19**, 196 (1972)

122. K.S.Krane, *Introduction of Neuclear Physics* (John Wiley & Sons, New York, 1988)

123. C.N. Burrous, A.J. Liebber and V.T. Zaviantseff, Rev. Sci. Instrum. **38**, 1477 (1967).

124. C.W. Kim and A. A. Pevsner, *Neutrino Physics*, Contemporary Concepts in Physics Series (John Wiley & Sons, New York, 1994)

APPENDICES

APPENDIX A

INTRODUCTION TO NEUTRINO PHYSICS AND NEUTRINO MASS LIMIT STUDY

Introduction to Neutrino Physics[124]

The idea of a neutrino was derived from experiments demonstrating a continuous beta decay spectrum. Experiments by Chadwick in 1914 produced the surprising result that beta ray spectra, in contrast to alpha and gamma ray spectra, were continuous rather than discrete. The missing energy was explained by Pauli in 1930 by proposing a new particle—a neutral fermion called "neutron". In 1933 Fermi dubbed Pauli's particle "neutrino" to distinguish it from the heavy neutron found by Chadwick a year previously. In 1934, Fermi formally developed his theory of beta decay in the framework of the quantum electrodynamics (QED) of Dirac, Heisenberg and Pauli. In the next section, there will be a brief discussion on the Dirac representation of neutrino derived from the QED theory.

Description of Neutrinos

In the QED theory, a Dirac state can be visualized in terms of a top spinning as it moves along. A particle's state is right-handed or left-handed according to whether its spin is along or opposite the direction of motion, respectively. These right- and left-handness are defined as positive and negative *helicity*. The spinor solutions of the Dirac equation, $\psi(x)$, are interpreted as quantum field operators and the electromagnetic (EM) field is represented by the vector potential field $A_\mu\,(x)$. Particles such as electrons, neutrinos and quarks are also presented by fields $\psi(x)$ that carry the particle's quantum numbers and are given by the linear superposition of creation and annihilation operators. The operator $A_\mu(x)$ creates or annihilates a quantum of the electromagnetic field at a space time point x. The electron field $\psi(x)$ annihilates an electron or creates a position at x, while $\overline{\psi(x)}$ creates an electron and annihilates a positron The interaction term between an electron and a EM field can be described by a Lagrangian density as

$$\mathcal{L}(x) = -j_\mu^{(e)}(x)A^\mu(x) = -(-ie)\,\overline{\psi_e(x)}\,\gamma_\mu\,\psi_e(x)\,A^\mu(x) \qquad \text{(A1.1)}$$

where the gamma (γ) are the Dirac matrixes, $\vec{\gamma} = \begin{pmatrix} 0 & \vec{\sigma} \\ -\vec{\sigma} & 0 \end{pmatrix}, \gamma^0 = \begin{pmatrix} 0 & -1 \\ -1 & 0 \end{pmatrix}, \gamma^5 = \begin{pmatrix} 1 & 0 \\ 0 & -1 \end{pmatrix}$

and $j_\mu^{(e)} = (-ie)\,\overline{\psi_e(x)}\,\gamma_\mu\,\psi_e(x)$ is the electron current. By simply replacing $j_\mu^{(e)}$ by $j_\mu^{(N)}(x) = \overline{\psi_p(x)}\,\gamma_\mu\psi_n(x)$, the neutron-proton nucleon current and $A^\mu(x)$ by $j_\mu^{(l)}(x) = \overline{\psi_e(x)}\,\gamma_\mu\,\psi_\nu\,(x)$, the electron-neutrino current, the Lagrangian density of neutron beta decay ($n \rightarrow p + e^- + \bar{\nu}$) can be expressed as

$$\mathcal{L}(x) = \frac{-G_F}{\sqrt{2}}\overline{\psi_p}(x)\gamma_\mu\psi_n(x)\overline{\psi_e(x)}\gamma_\mu\psi_\nu(x) \qquad \text{(A1.2)}$$

where $G_F = 1.19939 \text{X}10^{-5}$ /GeV is the couple constant. Similarly, the Lagrangian density of the electron capture decay in this work ($p + e^- \rightarrow n + \nu$) will be

$$\mathcal{L}(x) = \frac{-G_F}{\sqrt{2}}\overline{\psi_n}(x)\gamma_\mu\psi_p(x)\overline{\psi_\mu(x)}\gamma_\mu\psi_e(x) \qquad \text{(A1.3)}$$

Once the Lagrangian density is determined, one can uses it to set up the Euler-Langrangian equation of motion. The solutions of this equation can be then used to describe a Dirac state.

The Lagrangian describing a free neutrino, $\nu(x)$ can be expressed as

$$\mathcal{L}(x) = \bar{\nu}(x)\,(i\gamma\cdot\partial - m)\,\nu(x) \tag{A1.4}$$

where $\partial = \partial/\partial x_\mu$ and m is the mass operator. The Euler-Lagrangian equation of motion from Eq. (A1.4) becomes

$$(i\gamma\cdot\partial - m)\,\nu(x) = 0 \tag{A1.5}$$

The solution of Eq. (A1.5) is a superposition of plane waves

$$\nu(x) = \int \frac{d\vec{p}}{(2\pi)^{3/2}} \sum_s \left[\, u(\vec{p},s)\, a(\vec{p},s)\, e^{-ip\cdot x} + v(\vec{p},s)\, b^+(\vec{p},s)\, e^{ip\cdot x} \right] \tag{A1.6}$$

Eq. (A1.6) is called the Dirac representation of neutrino, where $s = \pm 1/2$ denotes the spins and $a(\vec{p},s)$ and $b^+(\vec{p},s)$ are, respectively, the neutrino annihilation and anti-neutrino creation operators. The $u(\vec{p},s)$ and $v(\vec{p},s)$ are four-component Dirac spinors. They are the solutions of Eq. (A1.7) as

$$(i\gamma\cdot\partial - m)\, u(\vec{p},s) = 0; \qquad (i\gamma\cdot\partial - m)\, v(\vec{p},s) = 0 \tag{A1.7}$$

The $u(\vec{p},s)$ and $v(\vec{p},s)$ are given by Eq. (A1.8)

$$u(\vec{p},s) = \sqrt{\frac{E+m}{2m}} \begin{pmatrix} 1 \\ \vec{\sigma}\cdot\vec{p}/(E+m) \end{pmatrix} \chi_s, \quad v(\vec{p},s) = \sqrt{\frac{E+m}{2m}} \begin{pmatrix} \vec{\sigma}\cdot p/(\vec{E}+m) \\ 1 \end{pmatrix} \bar{\chi}_s \tag{A1.8}$$

where χ_s is the spin matrix given by

$$\chi_s = \begin{cases} \begin{pmatrix} 1 \\ 0 \end{pmatrix} & for \quad s = +1/2 \\ \begin{pmatrix} 0 \\ 1 \end{pmatrix} & for \quad s = -1/2 \end{cases} \qquad \overline{\chi}_s = \begin{cases} -\begin{pmatrix} 0 \\ 1 \end{pmatrix} & for \quad s = +1/2 \\ \begin{pmatrix} 1 \\ 0 \end{pmatrix} & for \quad s = -1/2 \end{cases} \qquad \text{(A1.9)}$$

For a free neutrino, the Dirac spinors $u(\vec{p},s)$ and $v(\vec{p},s)$ are the eignstates of the helicity operator. Therefore, The left-handed and right-handed neutrino are defined by

$$\nu_L \equiv \left(\frac{1-\gamma_5}{2}\right)\nu, \qquad \nu_R \equiv \left(\frac{1+\gamma_5}{2}\right)\nu \qquad \text{(A1.10)}$$

They are also called Weyl neutrino fields. In fact, there are four Weyl neutrino fields, ν_L, ν_R, $(\nu_L)^C$ and $(\nu_R)^C$. Because ν_R and $(\nu_R)^C$ have not been observed in the nature, they are absent from the Standard Model of the electroweak theory. Neutrinos and electron are called *leptons*. Each one of them is characterized by its own lepton number which is conserved during weak interaction. There are three generations of leptons and quarks. Table A1.1 shows the three generations of leptons and quarks.

Table A1.1 The Three Generations of Quarks and Leptons

Generations	**1st**	**2nd**	**3rd**	
	u	c	t	quarks with charge +2/3
	d	s	b	quarks with charge -1/3
	ν_e	ν_μ	ν_τ	neutrinos with charge 0
	e	μ	τ	leptons with charge -1

The quarks and leptons listed in Table A1.1 are called “conventional” quarks and leptons. There might also exist a forth generation with very heavy neutrino. But they have not yet been observed. In 1937, Majorana proposed ν_M, another representation of neutrino which is self-conjugate, $\nu_M = (\nu_M)^C$. Both Dirac and Majorana representations do not require neutrino to be massless. Neutrino mass will be discussed in the next section.

Neutrino Mass and Neutrino Oscillation

There are many models that describe the masses of neutrinos. For simplicity, the following discussion is restricted to the case of only two generations of neutrinos, *e.g.* ν_e and ν_μ. The neutrino mass term in the Lagrangian is

$$\mathcal{L}_{\text{mass}} = -\frac{1}{2}(\overline{\nu_L^C} \mathrm{M} \nu_L + \bar{\nu}_L \mathrm{M} \nu_L^C) \qquad \text{(A1.11)}$$

where

$$\nu_L = \begin{pmatrix} \nu_e \\ \nu_\mu \end{pmatrix}_L \quad and \quad \mathrm{M} = \begin{pmatrix} m_{ee} & m_{e\mu} \\ m_{\mu e} & m_{\mu\mu} \end{pmatrix} \qquad \text{(A1.12)}$$

Notes that the ν_L is not the mass eigenstate and the mass matrix M is real and symmetric. By diagonalizing the mass matrix M, one can find the two eigenvalues of mass m_1 and m_2. The correspondent mass eigenfunctions are χ_1 and χ_2. For the left-handed system, the electron and muon neutrino are

$$\nu_{e,L} = cos\theta\, \chi_{1,L} + sin\theta\, \chi_{2,L} \qquad \text{(A1.13)}$$

$$\nu_{\mu L} = -\sin\theta\, \chi_{1,L} + \cos\theta\, \chi_{2,} \qquad \text{(A1.14)}$$

Note that the electron and muon neutrinos are not the eigenstate of mass but the linear superposition of mass eigenstates χ_1 and χ_2. According to quantum mechanics, if a system starts at $t = 0$ in a state that is not an energy eigenstate, then at later times it can oscillate into another orthogonal state. This brings about oscillation between electron and muon neutrinos. The time dependent of the electron neutrino state is

$$\nu_e(t) = \cos\theta\, \chi_1\, e^{-iE_1 t} + \sin\theta\, \chi_2\, e^{-iE_2 t} \qquad \text{(A1:15)}$$

where E_1 and E_2 are the neutrino energies associate to two different masses. Using the relativistic limit and assuming $p >> m_i$, $E_i = p + m_i^2 /2p$. The probability of an electron neutrino becoming an muon neutrino after traveling a distant L is

$$P(\nu_e \rightarrow \nu_{\mu}) = |\langle \nu_{\mu}^{0} | \nu_e(t) \rangle|^{2} = \sin^2 2\theta \sin^2((\Delta m)^2 L/4p) \qquad \text{(A1.16)}$$

where Δm is the mass different between m_1 and m_2..

Most of the neutrino mass research relies on the study of the nuclear beta decay ($n \rightarrow p + e + \bar{\nu}_e$). Since there are three particles resulting from this decay, the energy sharing determines that the maximum energy of the beta electron, E to be $E_0 - m_{\nu}$, where E_0 is the reaction energy and m_{ν} is the neutrino mass. Therefore, the focus point of the study is to analysis the details of the high energy end of the beta ray. Laboratories around the world have performed countless experiments using weak decay process with neutrinos as final products. The current experimental limits of neutrino masses are: $m_{\nu_e} < 9$ eV, m_{ν_μ}

< 250 keV and $m_{\nu_\tau} < 35$ MeV. The least stringent limit for the mixing of ν_e with ν_τ is for $100 < m_{\nu_\tau} < 1000$ keV, where the current limit is 0.7%.

The study of beta decay requires the understanding of a very complex three body problem. Therefore, another approach is sometimes used: the electron capture (EC) decay to probe of neutrino mass. As discussed in Chapter 2, neutrinos with different masses will induce different recoil energies in the daughter nuclei in the EC decay. If this energy difference could be measure experimentally, the neutrino masses could then be deduced from the recoil energy spectra.

Perspective on Neutrino Mass Limit Study

The information on the mixing rate of massless neutrino and massive neutrino was extracted from the time-of-flight spectrum of the recoiled ^{37}Cl ions. The coincidence peak in the time-of-flight spectrum in Fig. 4.3(a) was first fitted with a Gaussian and a constant background. The centroid obtained from the fitting was at channel 122.96 and the sigma (the sigma in the Gaussian expression; FWHM = 2.348 sigma) was 9.8 channels. The fitted area was 14390 ± 139 counts. A flat region to the right of the peak which represents slower recoil ions hence massive neutrino recoil is then fitted with a Gaussian and a flat background with the centroid and width fixed. The width was assumed to scale with the centroid, *i.e.,* it is assumed that ΔV/V remains constant as the velocity decreases. There is no physical basis for this assumption. It could very well be that ΔV/V (or ΔE/E) remains constant for lower velocity, in which case the errors below would be larger (*i.e.,* the limits would be worse). The distance between the sample and the center detector was 7.62 cm. The time scale was 1 channel = 0.0885 ms. From this information one gets the absolute velocity of the recoil ^{37}Cl ions for each channel number. The results of the fit is shown in Table A1.2.

Table A1.2. Fitting Result on the Neutrino Mass Mixing.

Channel (cha.)	Sigma (cha.)	Recoil E (eV)	ν-Mass (keV)	Area (count)	%Area	%Mix
150	12.0	6.5	464	1069±64	7.2±0.4	10.6±0.6
160	12.7	5.7	519	910±56	6.1±0.4	10.3±0.7
170	13.5	5.0	560	625±54	4.2±0.4	8.1±0.8
180	14.3	4.5	592	270±53	1.8±0.4	3.8±0.9
190	15.1	4.0	618	33±54	0.2±0.4	0.5±1.0
200	15.9	3.6	639	-113±54	-0.7±0.4	-1.9±1.1
210	16.7	3.3	657	-204±55	-1.2±0.4	-4.1±1.2

Where the percent area is the ratio of the fitted "second peak" to the main peak. As one can see from the table, this experiment does not have the sensitivity below m_ν = 600 keV because the tail of the main peak there gives a positive answer outside the statistical error for the area of the "second peak". Therefore, only the last three rows of data can be used.

The physically relevant quantity one tries to measure is the mixing ratio: if the neutrino emitted in the EC capture is a mixture of two mass eigenstates

$$|m_{EC}\rangle = C_0\,|m_0\rangle + C_I\,|m_I\rangle \tag{A1.17}$$

then the mixing ratio is $R_M = C_I^2 / C_0^2$. Since $C_I^2 + C_0^2 = 1$ and $C_I^2 << C_0^2$, $R_M = C_I^2$. The probability P_I of decay to a given mass state is proportional to $C_I^2\, q_I^2$

$$P_I \propto C_I^2\, q_I^2 \tag{A1.18}$$

where q_I is the momentum of the neutrino. The factor q_I is just the phase space available for the neutrino. (Fermi's Golden Rule contains the density of final states). Therefore

$$P_I/P_0 = (C_I^2\, q_I^2)\,/\,(C_0^2\, q_0^2) \tag{A1.19}$$

hence the mixing ratio

$$R_M = C_I^2 / C_0^2 = P_I/P_0\, q_0^2 / q_I^2 \tag{A1.20}$$

In Table A1.2, the next to the last column is the ratio of the massive neutrino "peak" to the main peak and the last column is that ratio multiplied by q_0^2 / q_I^2. Note that the ratio of the areas is not exactly the same as the ratio of probabilities because one has to account for the fact that the desorbing probability for 3-4 eV Cl^{37} ions might be different from those for 9.6 eV Cl^{37} ions. The dependence of the desorbing fraction on energy in this experiment is still unknown. If one assumes that they are the same, then the last column gives the mixing ratio. The last column is really C_I^2 / C_0^2 x (desorbing probability for recoils at energy E) / (desorbing probability for recoils at energy 9.6 eV). Usually one quotes a 90 % confidence level (about 2 sigma). Therefore, with the above assumptions, the mixing ratio is about < 2% at the 2 sigma level for neutrino with $m_\nu \sim 600$ keV. This result is a little higher than the results obtained by different ways for this mass region. To achieve better result, *i.e.,* to obtain lower mixture rates and for lower mass region, a narrower recoil time-of-flight coincidence peak with better statistics will be needed. This would require to reduce the broadening effects in the neutrino recoil induced ^{37}Cl ion desorption process.

To get better results on neutrino mass limit study, future experiments will measure coincidence between ^{37}Cl ions and X-ray photons which would select charge +1 ions only with negligible recoil due to photon and LMM Auger electron emission (3.5%). More important, those charge +1 ^{37}Cl ions created by X-ray relaxation instead of Auger relaxation from the initial K-hole would be less likely to transfer charges with their neighbors due to the restrictions of energy conservation. This would significantly reduce the charge exchanges and the following Coulomb repulsion interactions, and therefore reduce the dominant broadening effect. Several buffer layers of stable ^{40}Ar will also be used before the active ^{37}Ar is dosed on the cold sample to deduce the charge exchange with the substrate and the residual gases pre-adsorbed as the substrate is being cooling down. Simulations have shown that with the reduced broadening effects, the recoil time-of-flight coincidence peak would be more appropriate for extracting information on the mixture rates of the 200 keV massive neutrino than the results obtained by other means.

APPENDIX B

DESIGNING DIAGRAMS OF THE DETECTORS

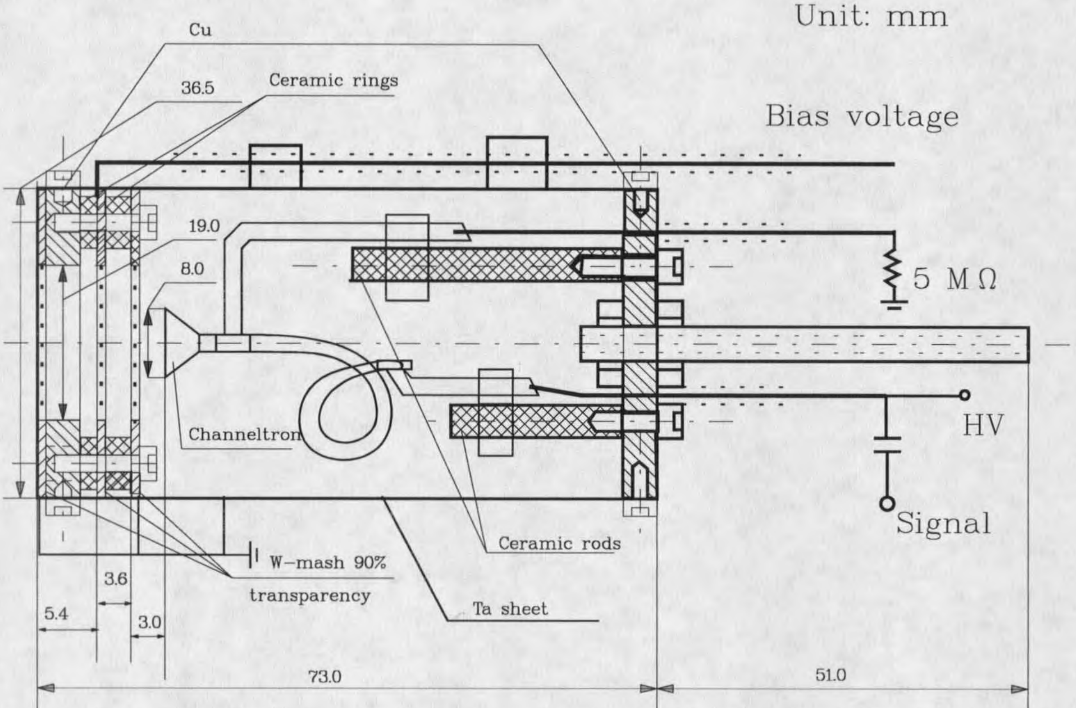

Channeltron Based Detector #2

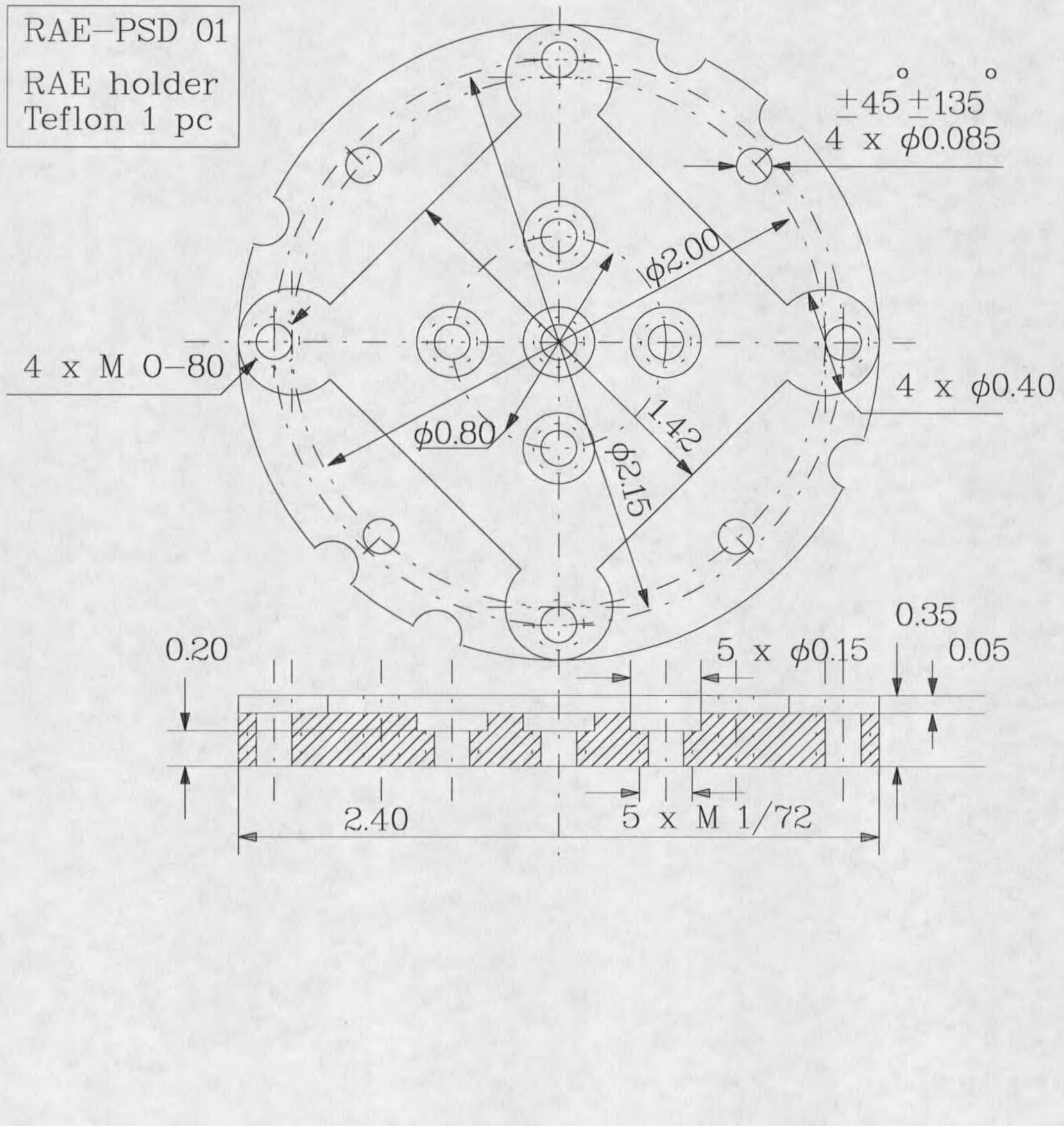
RAE–PSD 01
RAE holder
Teflon 1 pc
±45° ±135°
4 x ϕ0.085
ϕ2.00
4 x M 0–80
4 x ϕ0.40
ϕ0.80
1.42
ϕ2.15
0.20
5 x ϕ0.15
0.35
0.05
2.40
5 x M 1/72

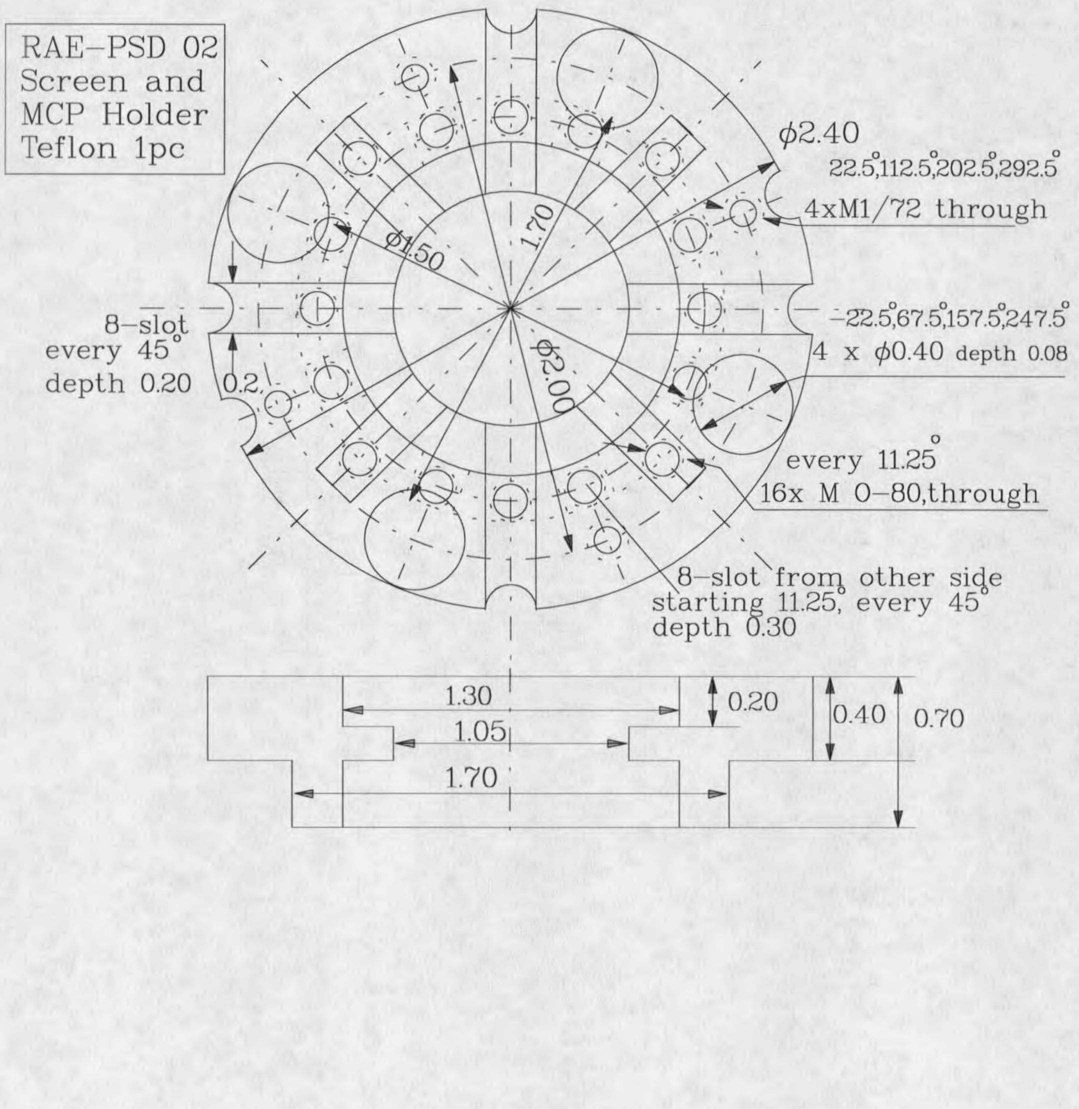
RAE–PSD 02
Screen and
MCP Holder
Teflon 1pc
ϕ2.40
22.5°,112.5°,202.5°,292.5°
4xM1/72 through
ϕ1.50
1.70
ϕ2.00
8–slot
every 45°
depth 0.20
0.2
–22.5°,67.5°,157.5°,247.5°
4 x ϕ0.40 depth 0.08
every 11.25°
16x M 0–80,through
8–slot from other side
starting 11.25°, every 45°
depth 0.30
1.30
1.05
1.70
0.20
0.40
0.70

RAE–PSD 03
Detector holder
Al 1 pc

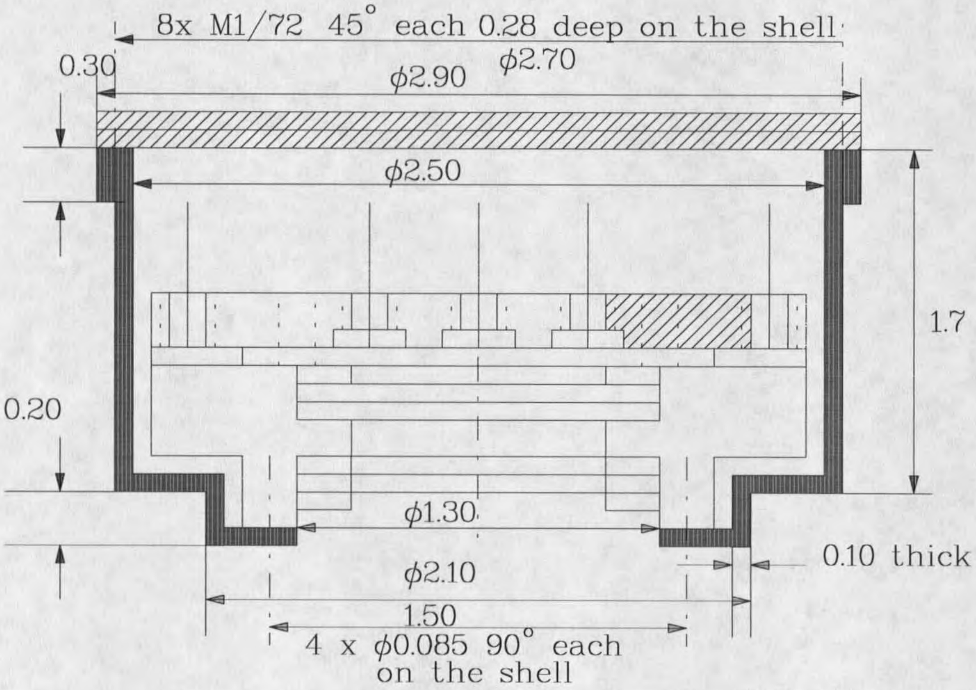

RAE–PSD 04
Bottom plate
Al 2pc

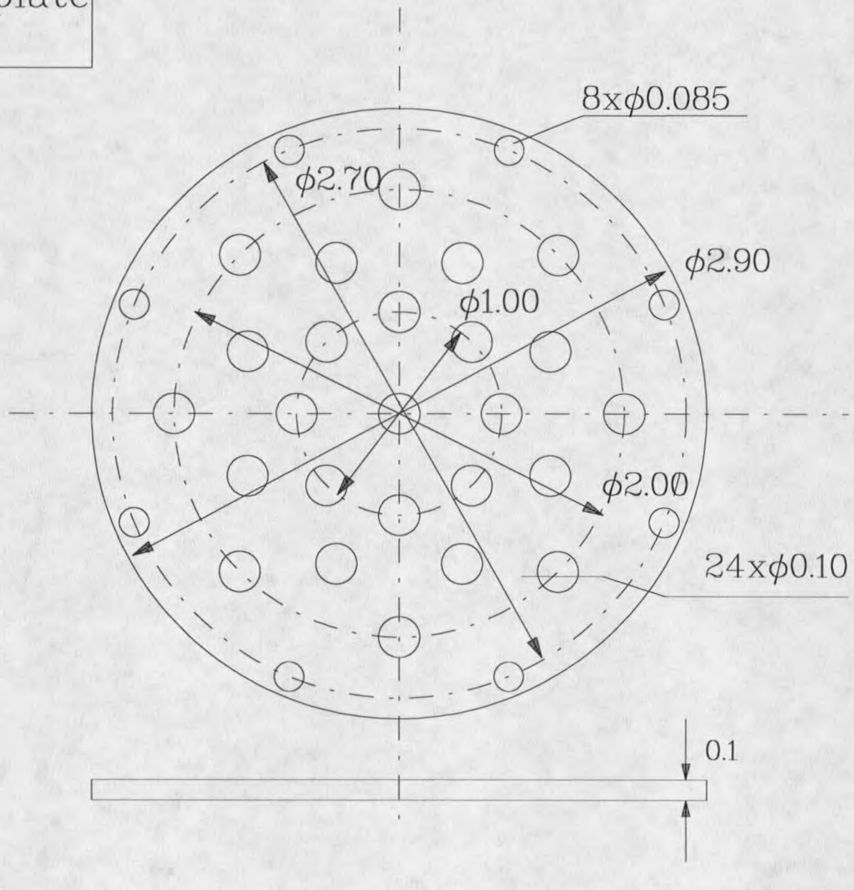

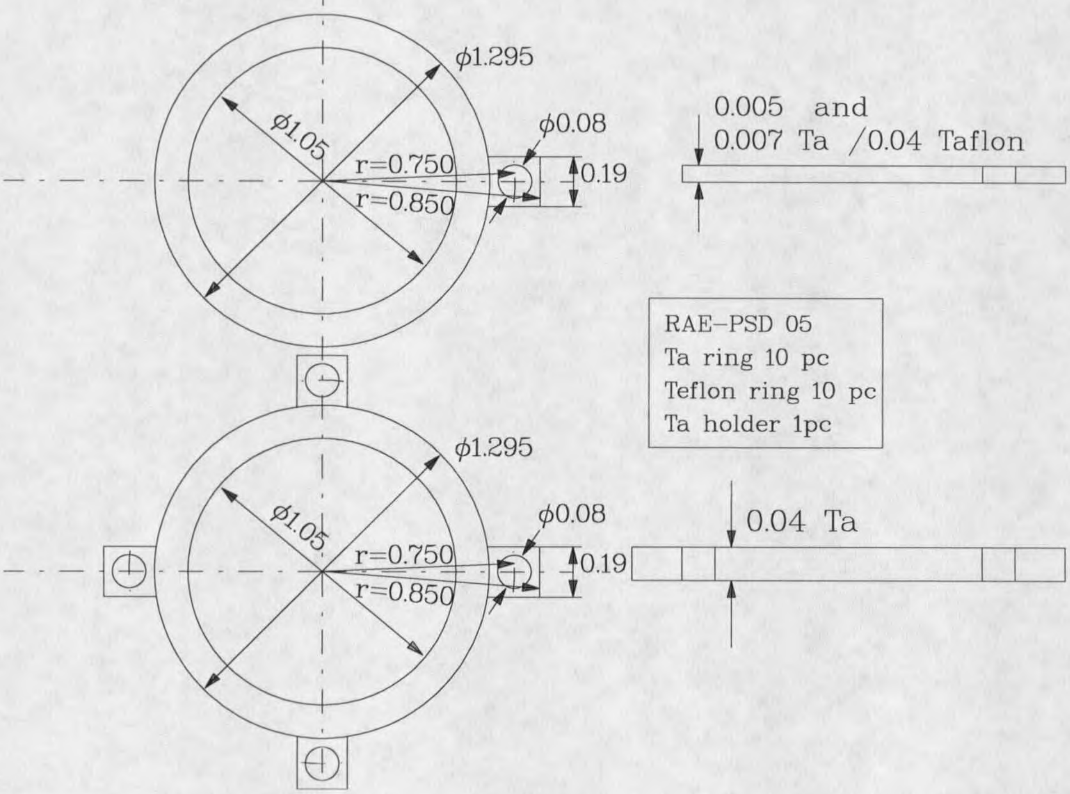

RAE–PSD 05
Ta ring 10 pc
Teflon ring 10 pc
Ta holder 1pc

RAE–PSD 06
Capacitor holder
Teflon 5 pc
MCP holder
Teflon 5 pc Ta 1 pc

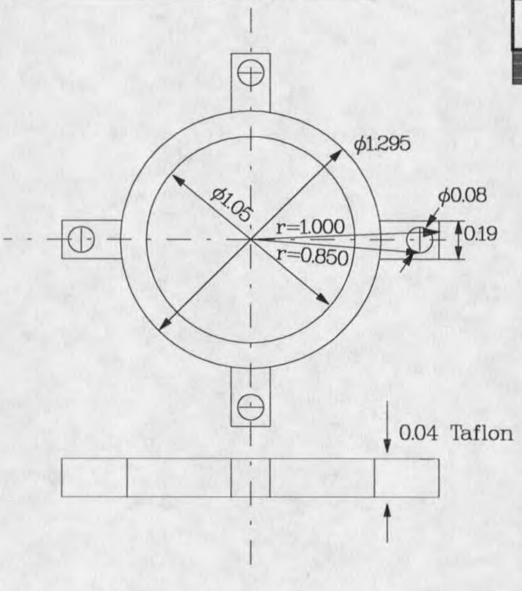

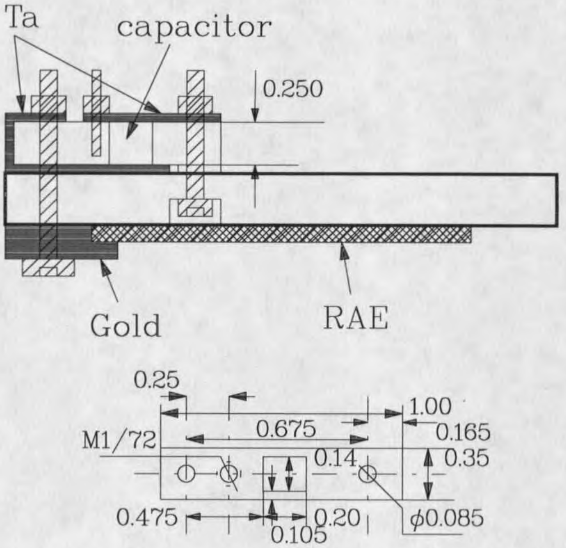

APPENDIX C

PLASMON DECAY INTO MULTI-ELECTRON-HOLE PAIRS IN SI(111)

Plasmon Decay into Multi-Electron-Hole Pairs in Si(111)

Lin Zhu,(1) Recep Avci,(1) M. M. Hindi,(2) and Gerald J. Lapeyre(1)

(1) *Department of Physics, Montana State University, Bozeman, MT 59717*

(2) *Department of Physics, Tennessee Technological University, Cookeville, TN 38505*

(December 20, 1992)

Abstract

The decay of plasmon excitations in Si(111) into multi-electron-hole pairs has been investigated. We observed coincidences between a ~1000 eV-electron beam, inelastically scattered from a Si(111) surface, and ~ 8.3 ± 0.3 eV-electrons resulting from the plasmon decay. The system geometry allowed only those coincidences in which a minimum of three plasmons with momenta $q \leq q_c \simeq 1$ Å^{-1} were excited, one of which subsequently decayed into two electron-hole pairs.

When a high-energy electron interacts with a solid, it gives rise to elementary excitations in that solid. The collective excitations, such as plasmons, and their subsequent decay have been a topic of interest since the early 1960's [1–5]. The decay of plasmon excitations can occur through a variety of channels; the one of interest here is the creation of electron-hole pairs with the emission of the electron into the vacuum. An impediment to the study of this phenomenon is that the kinetic energies of the emitted electrons are expected to fall between 0 and ~15 eV, which puts them in the region of intense secondary electrons. As a result the electrons emitted following plasmon decay are overwhelmed by the secondaries and their detection using conventional techniques is problematical.

In this paper we describe a coincidence method [6–9] of detecting just those electrons emitted as a result of plasmon decay. The coincidence is between (1) a primary electron that has created one or more plasmons and emerged from the sample surface with an energy reduced by a certain number of plasmon energies and (2) an electron which is created by the decay of one of these plasmons and is then emitted from the surface. The method discriminates against ordinary secondary electrons, which exhibit no correlation with the inelastically scattered primaries. The high selectivity of the method then permits detection of the electrons created in plasmon decay and a study of this process. Below we present for the first time the application of the coincidence technique to the study of the decay of plasmon excitations having a nonzero momentum in a Si crystal [10].

In general an electron beam transfers part of its energy and momentum to plasmon excitations in the solid. A typical dispersion relation between the energy $\hbar\omega(q)$ and momentum q transferred to the bulk plasmons is given to a first-degree approximation by [11]

$$\hbar\omega(q) \simeq \hbar\omega_p + \alpha(\hbar^2/m)q^2 + O(q^4). \qquad (1)$$

The parabola determined by Equ. (1) intercepts the single-pair excitation continuum of a simple metal at $q = q_c$, where q_c is called the critical momentum [2]. The significance of q_c in the plasmon decay process is that if $q < q_c$ the decay process must involve a minimum of two electron-hole pair excitations in order to conserve energy and momentum during the

When a high-energy electron interacts with a solid, it gives rise to elementary excitations in that solid. The collective excitations, such as plasmons, and their subsequent decay have been a topic of interest since the early 1960's [1–5]. The decay of plasmon excitations can occur through a variety of channels; the one of interest here is the creation of electron-hole pairs with the emission of the electron into the vacuum. An impediment to the study of this phenomenon is that the kinetic energies of the emitted electrons are expected to fall between 0 and ~15 eV, which puts them in the region of intense secondary electrons. As a result the electrons emitted following plasmon decay are overwhelmed by the secondaries and their detection using conventional techniques is problematical.

In this paper we describe a coincidence method [6–9] of detecting just those electrons emitted as a result of plasmon decay. The coincidence is between (1) a primary electron that has created one or more plasmons and emerged from the sample surface with an energy reduced by a certain number of plasmon energies and (2) an electron which is created by the decay of one of these plasmons and is then emitted from the surface. The method discriminates against ordinary secondary electrons, which exhibit no correlation with the inelastically scattered primaries. The high selectivity of the method then permits detection of the electrons created in plasmon decay and a study of this process. Below we present for the first time the application of the coincidence technique to the study of the decay of plasmon excitations having a nonzero momentum in a Si crystal [10].

In general an electron beam transfers part of its energy and momentum to plasmon excitations in the solid. A typical dispersion relation between the energy $\hbar\omega(q)$ and momentum q transferred to the bulk plasmons is given to a first-degree approximation by [11]

$$\hbar\omega(q) \simeq \hbar\omega_p + \alpha(\hbar^2/m)q^2 + O(q^4). \tag{1}$$

The parabola determined by Equ. (1) intercepts the single-pair excitation continuum of a simple metal at $q = q_c$, where q_c is called the critical momentum [2]. The significance of q_c in the plasmon decay process is that if $q < q_c$ the decay process must involve a minimum of two electron-hole pair excitations in order to conserve energy and momentum during the decay, while for $q > q_c$ energy and momentum can be conserved in a single electron-hole pair excitation. Theoretical calculations [12] suggest that two-electron-hole-pair excitation dominates the decay process for $q < q_c$.

In our setup we were restricted in the placement of detectors. As a result, we were able to observe only those processes in which multiple plasmons with momentum $q \leq q_c$ were created. Within the restrictions imposed by the detection geometry it was found that the best signal-to-noise ratio is obtained when the kinetic energy of the emitted electrons is around 8 eV, which appears to be a density-of-states effect.

A schematic diagram of the experimental setup is shown in Figure 1. The sample and the detectors were placed in an ultrahigh vacuum system at a pressure of 10^{-10} torr. The sample, a p-type Si(111) crystal with ~20 Ω-cm resistivity, was cleaned using conventional techniques to obtain a (7x7) reconstruction. Such a sample shows strong multiple plasmon energy loss peaks at ~17 eV spacings (see Fig. 2). A double-pass cylindrical mirror analyzer (CMA) detected slow electrons (< 15 eV) with a 0.6 eV energy window. A channeltron C2 with a high-pass energy filter and a small acceptance angle (±1.4°) detected electrons above a predetermined kinetic energy. Primary electrons were generated by a co-axial electron gun in the CMA. The primary electrons were incident at 42° with respect to the sample normal. The shaped and amplified channeltron pulse from C2 started a time-to-amplitude converter (TAC), while the shaped and amplified signal from channeltron C1 in the CMA stopped the TAC. The TAC output was fed into a multichannel analyzer (MCA). An MCA spectrum then represents the coincident counts vs. time within a preset time window. A typical MCA spectrum is shown in the inset in Fig. 1. One spectrum typically takes about six hours to collect. As evident in Fig. 1, the statistical error is dominated by the accidentals. Because the accidental count rate is proportional to the square of the primary electron beam intensity, whereas the true coincidence rate is proportional to the primary electron beam intensity, increasing the primary beam intensity does not substantially improve the statistical error for a fixed counting time. (See, for example, Ref. [8].) Further improvement in the statistical error can only result from increasing the counting time and/or improving the detection efficiency.

Figure 2 shows a coincidence spectrum (CS) superimposed on an electron energy loss spectrum (ELS). The coincidence is between $E_k \simeq 8.3 \pm 0.3$ eV-electrons (detected by C1) and primary electrons whose energy loss is smaller than ΔE (detected by C2). Also shown in Fig. 2 is a spline fit to the CS spectrum. Each point and its error bar in the CS spectrum are determined by the background-subtracted coincidence peak area of the MCA spectrum, as shown in Fig. 1. For the ELS the ΔE in the figure represents the energy loss by the primary electrons; for the CS the ΔE represents the difference between the primary energy (E_o=1009 eV) and the retarding voltage applied to the screen of C2. For the last point in Fig. 2, having $\Delta E = 200$ eV and ~1600 counts per six hours (cp6h), the background counts were about 10,000 cp6h, C1 counted $\sim 10^8$ cp6h, and C2 counted 4×10^7 cp6h. About 5% of the C2 counts ($\sim 2 \times 10^6$ cp6h) were due to plasmon losses. Of these only a handful of $\sim$ 1600 contributed to the coincidence in our setup.

The arrows in Fig. 2 indicate the locations of $\Delta E = n\hbar\omega_p$, corresponding to the energy loss due to multiple plasmon creation. Also shown are the locations of the Si 2p and Si 2s core levels. The CS shows no detectable coincidence counts below the 50-eV energy loss which corresponds to $n \simeq 3$. Above the 50-eV loss the coincidence counts increase in a step-like fashion at energy loss locations corresponding roughly to the creation of multiple plasmons with $n \simeq 4$ and 5, and to excitation of the Si 2p and Si 2s core levels.

The coincidence threshold for $n \geq 3$ can be explained as follows: Detector C2 is located 12° above the scattering plane; therefore, specularly reflected electrons cannot reach it. Excitations of one or more plasmons with $q \simeq 1$ Å^{-1} are needed to deflect the beam by $\sim 12°$. A single plasmon loss requires a momentum transfer larger than q_c in order to bend the beam into C2. The cross section for exciting plasmons with $q > q_c$ is very small [11] and hence results in a negligible coincidence count rate. On the other hand, if the momentum transfer to the plasmon is $q \leq q_c$, the plasmon can decay via two electron-hole pair creation with one of the electrons staying in the solid and the second ejected from the solid in the direction of C1. However, for momentum transfers of $q \leq q_c$ three inelastic scatterings are required to bend the beam 12° out of the plane. The details of these arguments are given below.

The relationship among the momentum **k** of the incident beam, the momentum **q** of the excited plasmon, and the energy $\hbar\omega(q)$ lost to the plasmon is fundamental to understanding our observations. Reference [11] reports the measured q_c and the dispersion coefficient α (see Eq. 1) for Si as $q_c \simeq 1.1$ Å^{-1} and $\alpha \simeq 0.41$ for q in the $\langle 100 \rangle$ direction and $\alpha \simeq 0.32$ in the $\langle 111 \rangle$ direction. We assume $\alpha \simeq 0.4$ of the nearly free electron gas value in the $\langle 1\bar{1}0 \rangle$ direction. Taking into account $\hbar\omega_p = 17$ eV, this means an electron will transfer an energy of $\hbar\omega(q) \simeq 20$ eV at momentum $q \simeq q_c$ in the $\langle 1\bar{1}0 \rangle$ direction. It can easily be shown that for $q \simeq q_c$ most of the momentum transfer by a $\sim$ 1000-eV incident electron is perpendicular to the travel direction of the electron. With this momentum transfer the incident electron beam will deviate from its original direction by $\sim 3.6°$.

Figures 3a and 3b depict the scattering processes and the coincidence geometry. The CMA accepts electrons falling into a polar angle of $42 \pm 6°$ from the CMA axis (the direction of the incident electrons). Detector C2 is located about 12° off the scattering plane defined by the incident **k** vector and the sample normal. A coincidence can take place in one of two ways: (1) An electron scatters elastically (but non-specularly) within the 3° cone about detector C2, followed by a single plasmon loss with momentum transfer **q** to reach the detector. Since no coincidence signal is observed for plasmon losses corresponding to $n = 1$ or $n = 2$ we assume that this is a rather weak contribution, owing to the fact that non-specular elastic scattering has a rather weak intensity. (2) An electron excites multiple plasmons, each with $q \simeq q_c$, on the way into and/or out of the solid, following or preceding a specular reflection. We think the latter channel is responsible for our observations. As shown in Fig. 3a, the multiple plasmon loss provides a multiple momentum transfer, bending the beam by about 12° into detector C2. For an electron beam of 1000-eV energy a minimum of three consecutive plasmon losses, each bending the beam by $\simeq 3.6°$, is required for a coincidence. The observed coincidence rates are consistent with rough estimates of the probability of these multi-scattering processes. For $n \geq 3$ some of the losses may have $q \simeq 0$

momentum transfers causing the step-like increase in coincidence counts every time a new loss channel is introduced (see Fig. 2). After the core level transitions have taken place, the relaxation process generates a cascade of secondary electrons, resulting in a further step-like increase in the coincidence counts.

For single plasmon excitation ($n = 1$) a momentum transfer $q \simeq 3$ Å^{-1} is required for bending the beam by 12°. The coincidence rate for this case is very small because (1) the cross section of plasmon excitation for $q \simeq 3$ Å^{-1} is almost nil [11], (2) the decay of plasmons with $q > q_c$ is mostly via single electron-hole creation; energy and momentum conservation limit the possible initial states from which the electron can be ejected. Similar arguments can be made for two plasmon excitation ($n = 2$).

Figure 3b shows the vector diagram for the conservation of momentum in the case of plasmon decay to two electron-hole pairs: $\mathbf{k}_1 + \mathbf{k}_2 = \mathbf{q}$ where vectors $\mathbf{k}_1$ and $\mathbf{k}_2$ are changes in the momenta of the two electrons excited as a result of plasmon decay. Here we assumed that the electrons originated at the Γ point. The electron with $\mathbf{k}_1$ is detected by C1 while the electron with $\mathbf{k}_2$ stays in the solid because of the direction of its momentum. Vector $\mathbf{q}$ is assumed to be nearly parallel to the surface along the $\langle 1\bar{1}0 \rangle$ direction. The conservation of energy requires that $\hbar\omega(q) = E_1 + E_2 \simeq 20$ eV, where E_1 and E_2 are the changes in energy of the electrons with momenta $\mathbf{k}_1$ and $\mathbf{k}_2$, respectively. The kinetic energy E_k (=8.3 eV) of the emerging electron is selected such that E_2 matches the difference between the bulk initial and final density-of-state maxima, which are separated by $\sim$ 6.5 eV [14]. This means $E_1 \simeq 13.5$ eV, and an electron initially at the top of the valence band maximum (Γ point) will come out of the solid with $E_k \simeq 8.5$ eV. However, E_1 and E_2 can vary due to variations in initial states, such that $E_1 + E_2 \simeq 20$ eV and $E_k = E_1 - \Phi \simeq 8.3$ eV, where $\Phi \simeq 5$ eV is the work function. The electron ejected from the crystal will be detected by C1 provided that it falls into the acceptance angle of C1. For example, an 8.3 eV electron making a 45° angle with $\mathbf{q}$ will need a perpendicular component of about 1 Å^{-1}. The component of $\mathbf{k}_1$ perpendicular to the surface cannot easily be related to the component inside the solid because the translational invariance is broken in that direction. Knowledge of the band structure in the various k-directions, the surface reconstruction, the initial states of the ejected electrons in relation to the plasmon decay, the orientation of the crystal, and the angular and energy acceptances of both detectors is necessary to pinpoint exactly the initial and final states of the ejected electrons accompanying a plasmon decay.

In summary, we report the first direct measurements of multiple electron-hole pair creation resulting from the decay of plasmons having momentum near q_c. The system geometry only allowed observation of coincidences between incident electrons which have suffered a minimum of three multiple plasmon losses and electrons ejected as a result of the decay of these plasmons. The technique has a promising future for studying the unexplored elementary excitations of solids provided that proper angular and energy resolving detectors and a precision sample manipulator are used.

We thank J. Anderson for critical editing of the manuscript with many helpful comments and corrections. We thank J. Hermanson and A. Equiluz for helpful discussions. The work is supported by NSF Grant No. DMR 9102854. M.M.H. acknowledges support by the U.S. Department of Energy, Nuclear Physics Division, via Grant No. DE-FG05-87ER40314.

REFERENCES

[1] D. F. DuBois, Annals of Physics **8**, 24 (1959), and D. F. DuBois and M. G. Kivelson, Phys. Rev. **186**, 409 (1969).

[2] *Elementary Excitations in Solids*, by David Pines (W. A. Benjamin, Inc., 1964).

[3] M. Hasegawa and M. Watabe, J. of the Phys. Soc. of Japan **27**, 1393 (1969).

[4] P. K. Aravind, A. Holas, and K. S. Singwi, Phys. Rev. B **25**, 561 (1982), and A. Holas and K. S. Singwi, Phys. Rev. B **40**, 158 (1989).

[5] M. E. Bachlechner, W. Macke, H. M. Miesenböck, and A. Schinner, Physica B, **168** 104 (1991).

[6] H. W. Haak, G. A. Sawatzky, L. Ungier, J. K. Gimzewski, and T.D. Thomas, Rev. Sci. Instrum. **55**, 696 (1984).

[7] S. Thurgate, B. Todd, B. Lohmann, and A. Stelbovics, Rev. Sci. Instrum. **61**, 3733 (1990).

[8] E. Jensen, R. A. Bartynski, S. L. Hulbert, and E. D. Johnson, Rev. Sci. Instrum. **63**, 3013 (1992).

[9] F. J. Pijper and P. Kruit, Phys. Rev. B 44, 9192 (1991).

[10] An excellent work by Pijper and Kruit in Ref. [9] reports coincidence measurements between the secondary electrons and the energy-loss events in C foils using 80 keV electrons in transmission. Some of the low-energy electron production is attributed to the plasmon decay process in C-foil.

[11] J. Stiebling and H. Raether, Phys. Rev. Lett. **40**, 1293 (1978).

[12] See, for example, Ref. [5] and references therein.

[13] The broadening in the time resolution is mostly due to different flight paths in the

cylindrical mirror analyzer. For details see reference [6].

[14] *Handbook of the Band Structure of Elemental Solids*, by D. A. Papaconstantopoulos (Plenum Press, New York, 1986).

FIGURES

FIG. 1. Schematic of the coincidence spectrometer. A typical channeltron pulse is shaped and amplified by TFA and then CFD before it arrives at the TAC input. A typical TAC spectrum is shown in the inset. The area under the background-subtracted peak determines the coincidence counts.

FIG. 2. The coincidence spectrum (open circles with error bars) superimposed on the electron energy loss spectrum (dotted line). Arrows indicate energy positions corresponding to multiple plasmon loss energies for $n = 1$ through $n = 5$ and the Si 2p and Si 2s core level positions. The (ΔE) for the coincidence spectrum is $\Delta E = E_o - eV$, where V is the voltage applied to the retarding grid in front of C2. The line through the points is a spline fit to the coincidence data.

FIG. 3. The model explaining the data shown in Fig. 2: (a) Inelastic process scattering the incident electron beam with $\mathbf{k_i}$ into detector C2. The model assumes the incident beam transfers a momentum $\mathbf{q}$ perpendicular to $\mathbf{k_i}$. Each time a momentum $q \simeq q_c$ pointing to the left is transferred to a plasmon the beam bends $\sim 3.6°$ to the right. Three successive momentum transfers ($n = 1, 2$ and 3) to a bulk plasmon will bend the beam into the detector. The plasmon losses can take place on the way into the solid and/or on the way out of the solid following a specular reflection represented by $\mathbf{k_s}$ in the figure. (b) Conservation of momentum during the plasmon decay process. Vector $\mathbf{q}$ represents the decaying plasmon while vectors $\mathbf{k_1}$ and $\mathbf{k_2}$ represent the excited electrons, one of which (k_1) is detected by C1 in coincidence with the inelastically scattered electron (k_f) detected by C2 in part (a).

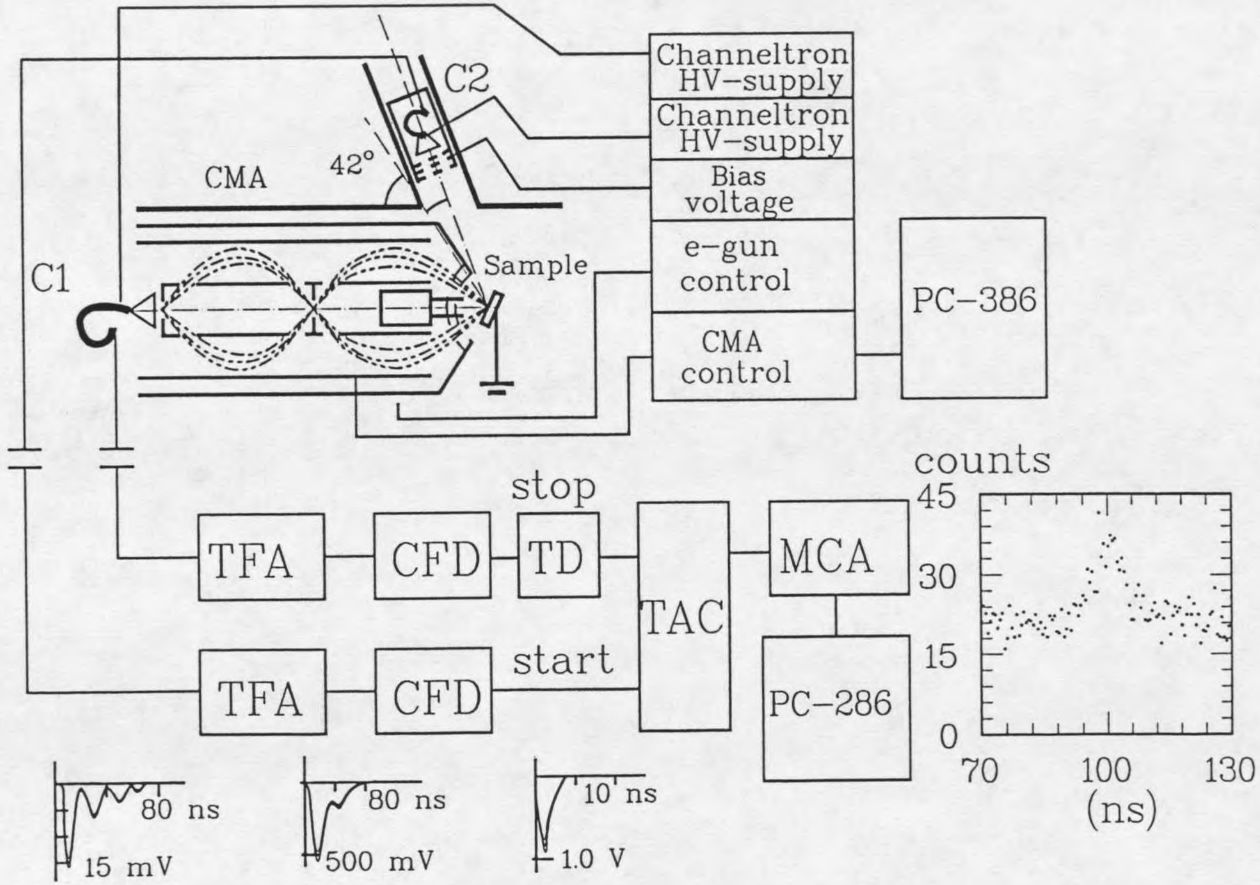

TFA: Timing Filter Amplifier
CFD: Constant Fraction Discriminator
TAC: Time-to-Amplitude Convertor
MCA: Multichannel Analyzer
TD: Time Delay
CMA: Cylindrical Mirror Analyzer

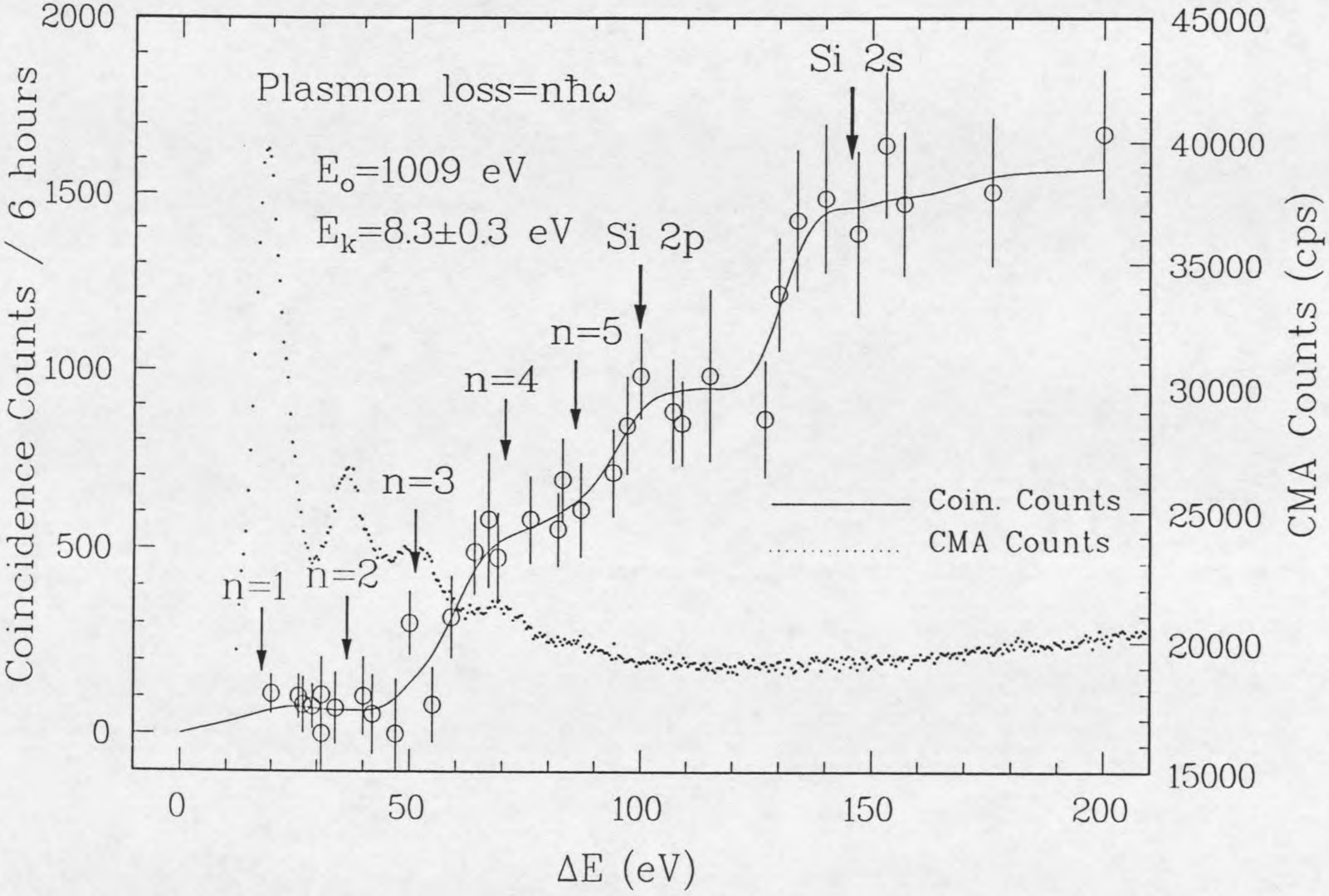
Plasmon loss=nħω
E$_o$=1009 eV
E$_k$=8.3±0.3 eV
Si 2s
Si 2p
n=1
n=2
n=3
n=4
n=5
Coin. Counts
CMA Counts
Coincidence Counts / 6 hours
CMA Counts (cps)
ΔE (eV)
0
50
100
150
200
500
1000
1500
2000
15000
20000
25000
30000
35000
40000
45000

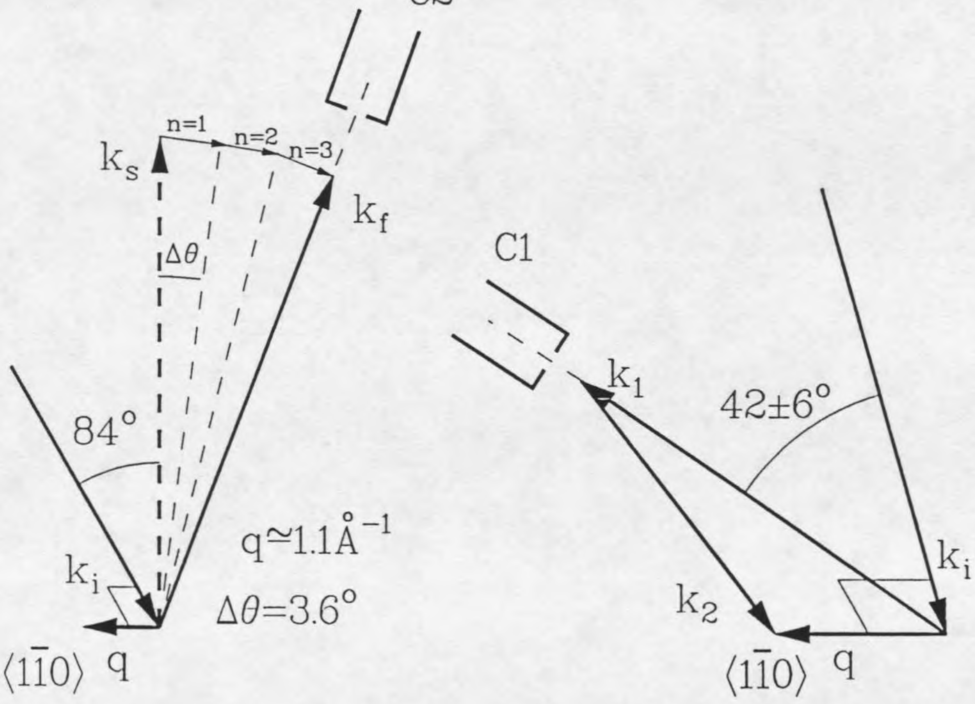

a. inelastic scattering.

b. plasmon decay.